UNIVERSITY OF CALIFORNIA
RIVERSIDE

Design Strategies for Enhancing Photoreactive Systems

A Dissertation submitted in partial satisfaction
of the requirements for the degree of

Doctor of Philosophy

in

Chemistry

by

Thomas Joseph Gately

September 2022

Dissertation Committee:
Dr. Christopher Bardeen, Chairperson
Dr. Jingsong Zhang
Dr. James Davies

The Dissertation of Thomas Joseph Gately is approved:

_____

_____

_____

Committee Chairperson

University of California, Riverside

Acknowledgements

First, I would like to thank Professor Chris Bardeen for everything he has done to support me during my PhD adventure. Chris is an incredible scientist, and great mentor and teacher. He is always coming up with new ideas and is open to any ideas I come up with. He has been very understanding of my situation with the Air Force and has helped push me to get everything done that I needed to complete my PhD in three years. I am very proud to say that I worked with Chris Bardeen for my PhD.

I would like to thank all of the members of the Bardeen lab during my time at UCR. Dr. Kerry Hanson, Dr. Fei Tong, Dr. Xinning Dong, Dr. Wangxiang Li, Dr. Hossein Mostafavi, Adam Berges, Brandon Lui, Taylor Lewis, Touhid Bin Anwar, Pranaya Pravin Ghate, Marielle Sewell, Kevin Lam and Jacob Rodriguez. The assistance in the lab, positive attitude, and helpful conversations to get through a problem were monumental in my success. I would also like to thank my master's advisors, Jim Ranville and Tom Wildeman for all of their guidance in graduate school and during my undergraduate career. You really helped lay the groundwork for my success.

I am also grateful for all of our collaborators. Dr. Rabih Al-Kaysi and his lab for all of their interesting unique compounds that they synthesize. Dr. Greg Beran and our collaborators from the Beran Group, for their calculations to explain our research. Dr. Robert Dillon for his assistance with the ultrafast system. Dr. David Casanova for his excited state calculations. Dr. Hans Van Tol and the entire Mag Lab staff for supporting our visit and analysis on their high end EPRs. I am very appreciative of all the work you have done to make these projects possible.

I would like to thank all of my family. My parents for all they have done for me, and for putting up with me for so many years. Finally, I would like to thank my wife Kristina for all of her love and support, leaving her job in Las Vegas and moving to Riverside having our daughter Ophelia. Thank you for sleeping well, Ophelia, it makes work that much easier. It has been amazing having both of you by my side and I look forward to our next adventure in San Antonio.

Portions of the dissertation are adapted with permission from the following references:

Chapter 3: T. J. Gately, W. Li, S. H. Mostafavi, and C. J. Bardeen, “Reversible adhesion switching using spiropyran photoisomerization in a high glass transition temperature polymer," Macromolecules, 2021 54, 20, 9319–9326.

Chapter 4: T.J. Gately, W. Sontising, C.J. Easley, I. Islam, R.O. Al-Kaysi, G.J.O. Beran, C.J. Bardeen, “Effect of halogen substitution on energies and dynamics of reversible photomechanical crystals based on 9-anthracenecarboxylic acid,” CrystEngComm, 2021 23 (34), 5931-5943

ABSTRACT OF THE DISSERTATION

Design Strategies for Enhancing Photoreactive Systems

by

Thomas Joseph Gately

Doctor of Philosophy, Graduate Program in Chemistry
University of California, Riverside, September 2022
Dr. Christopher Bardeen, Chairperson

Stimulus-response chemical systems have been pushed to the forefront of research since the 2016 Nobel prize was awarded for molecular machines. Photoreactive systems represent one of the most promising of all stimulus-response systems. These systems can rapidly overcome large energy barriers to create useful effects like motion and adhesion. Furthermore, light is easily tunable, and can be rapidly delivered to the location necessary to generate the reaction leaving the surroundings unaffected. While many photoreactive systems have been found, there exist many ways to improve their effectiveness or elicit more useful properties from them. This dissertation focuses on three photoreactive systems generating adhesion, photomechanical motion, and spin stabilization in a crystal.

Adhesion can be enabled by light through a variety of methods. Photocrosslinking, photoinduced phase changes, and mechanical bonding between surfaces have all been previously explored methods for photoadhesives. Reversible adhesion has been more elusive though. By focusing on noncovalent adhesion this experiment was able to generate a photoreversible adhesive using a polar substrate, a nonpolar glue, and spiropyran, a photochrome that changed color and polarity when exposed to light. The shear strength

was increased by a factor of 5 between the reacted and unreacted state and the entire system was reversible to within 10% of its initial values.

Photomechanical systems can be used to do work in place of electronic motors. 9-anthracene carboxylic acid (9AC) is a well-known thermal backreaction photomechanical system. By looking at the fluorescence recovery after photobleaching combined with calculations of the energetics of isolated molecules and those in the crystal lattice we were able to develop a deeper understanding of the crystal system. Calculations showed an energetic threshold of 80-90 kJ per mole was the limiting energy for the dimerization reaction, due primarily to the steric interactions of molecules. The absence of hydrogen fluorine intermolecular bond formation along with the energy differences was able to explain much of the observed differences in mechanical reset times. The crystal kinetics were much more complicated though as a strong concentration dependence of the dimer was observed.

Two state systems have many potential applications in quantum information systems. Crystal defects are one such two state system that has seen success as a qubit candidate. 4-azidobenzoic acid generates a stable nitrene biradical when reacted in a crystal. By fluorinating the 4-azidobenzoic acid changes to the crystal structure as well as the reduced ability for the radical to form side products stabilized the nitrene for weeks at room temperature and produced the characteristic signal of a nitrene biradical at 6700 G. Both nitrenes fluoresces in the visible spectrum allowing for readouts of quantum information. The foundation of a nitrene based quantum information system has been laid but further investigation is needed to make it a reality.

Table of Contents

List of Figures

List of Tables

Chapter 1 Introduction

The ability for a material to change its properties in response to an external stimulus is highly sought after. In 2016 the Nobel Prize in chemistry was jointly awarded to Bernard Feringa, Jean-Pierre Sauvage, and James Fraser Stoddart for their design of molecular machines.[1-3] Molecular systems may react to many stimuli such as shock, heat, pH, light, or many other phenomena.[4] Light is of particular interest as it can be delivered rapidly and directly to where it is needed through relatively simple means like fiber optics and avoids exposure to the rest of the system. Additionally, light has many variables which can be controlled and tailored to the system, such as the wavelength, intensity, and polarization.

Light can be used to transform the properties of materials providing the stimulus in a stimulus response system. Historically light has been used to generate reactions in chemistry such as the initiation of photochlorination by ultraviolet (UV) light[5] photodegradation[6], photochemical rearrangements[7], and the Norrish reaction[8] to name a few. While these reactions are important, they are not the stimulus response photochemical systems that seen extensive research in recent years. Stimulus response photochemical systems are able to perform useful work like motion[18-23], or adhesion[13-15]. Stimulus response chemical systems like these could potentially replace some everyday chemical and electrical systems and deliver savings on cost, and weight while increasing robustness.

1.1 Photochemistry

Photochemistry examines the chemical effects of light[9]. Photochemistry reaction pathways allow for higher energy intermediates that cannot be generated thermally. This

enables the reaction to overcome a large activation barrier in a short timeframe, allowing reactions to occur that cannot progress by thermal processes[10]. Lasers are able to excite molecules to a desired electronic or vibrational state which allows a high degree of selectivity in a photoreaction[11]. There are many types of famous photochemical reactions, including photosynthesis, vitamin D synthesis[12] and many lesser-known reactions that will be discussed in the next section. Many of these reactions can generate useful phenomena such as adhesion[13-15], electron spin[16-17], or movement[18-23]. Many of these systems could be made more useful by fine tuning parameters either in, or around the system.

1.1.1 Types of photoreactions

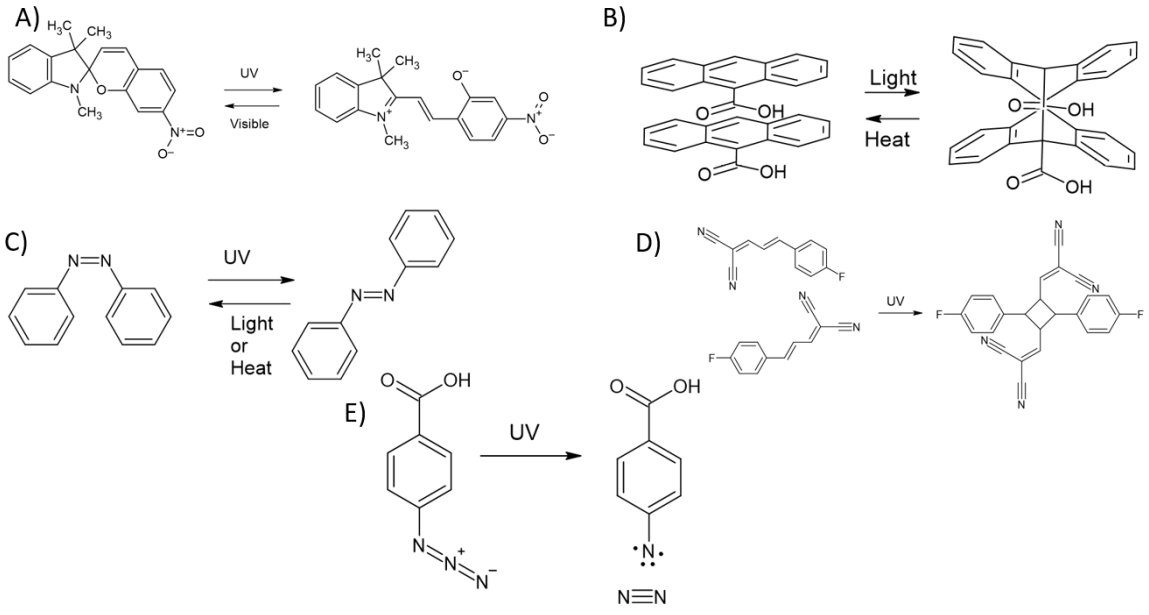

Figure 1.1: Illustrations of various types of photoreactions. **A)** Spiropyran converts to merocyanine by a ring opening reaction. **B)** 9-Anthracene carboxylic acid undergoes a 4+4 photodimerization. C) Azobenzene undergoes a cis to trans isomerization. **D)** 4-Fluoro Cinnamaldehyde Malononitrile undergoes a 2+2 photodimerization. **E)** 4-Azidobenzoic acid undergoes a photolysis to generate a nitrene and nitrogen gas. The nitrene typically reacts quickly with molecules around it. Reactions D and E are irreversible.

Broadly there are three types of reactions based off the reaction mechanism discussed in this dissertation: cis to trans or E/Z isomerization, bond cleaving reactions, and bond forming reactions. Azobenzene is a famous cis to trans isomerization molecule and is shown in Figure 1.1C.[24] Bond forming reactions include 9-anthracene carboxylic acid (Figure 1.1B), which undergoes a 4+4 photodimerization, and cinnamic acids that undergo a 2+2 photodimerization (Figure 1.1D)[25]. Bond cleaving reactions include the formation of nitrogen gas when cleaved from an azide (Figure 1.1 E)[26], and the ring opening and twisting of spiropyran forming merocyanine (Figure 1.1A)[27]. Some of these reactions, such as spiropyran and merocyanine and azobenzene, are reversible, while cinnamic acids dimerization and azide photolysis are not.

1.1.2 P-Type and T-type Photochromes

Reversible reactions can be divided into two types of reversibility. Molecules that undergo a thermal back reaction like anthracene are considered T-type. Molecules that return to their original state by photons are called P-type[28-29]. Both categories of reaction process forward with light but the back reaction's activation energy in T-type reactions is much smaller than those seen in P-type materials[30]. The 4+4 photodimerization of 9-anthracene carboxylic acid is a well-known T-type reaction as is the cis to trans isomerization of azobenzene. These reactions typically have a back reaction barrier of about 80 kJ/mol[31]. P-type materials, such as diarylethenes have back reaction activation energies of 150 kJ/mol[32]. Some molecules, like spiropyran and merocyanine can be either T-type or P-type depending on their environment with the more polar zwitterionic merocyanine form favoring polar environments while the less polar spiropyran favoring

less polar environments. The large change in charge distribution between the two forms is responsible for stabilizing one over another in various mediums.[33]

1.1.3 Positive and Negative Photochromes

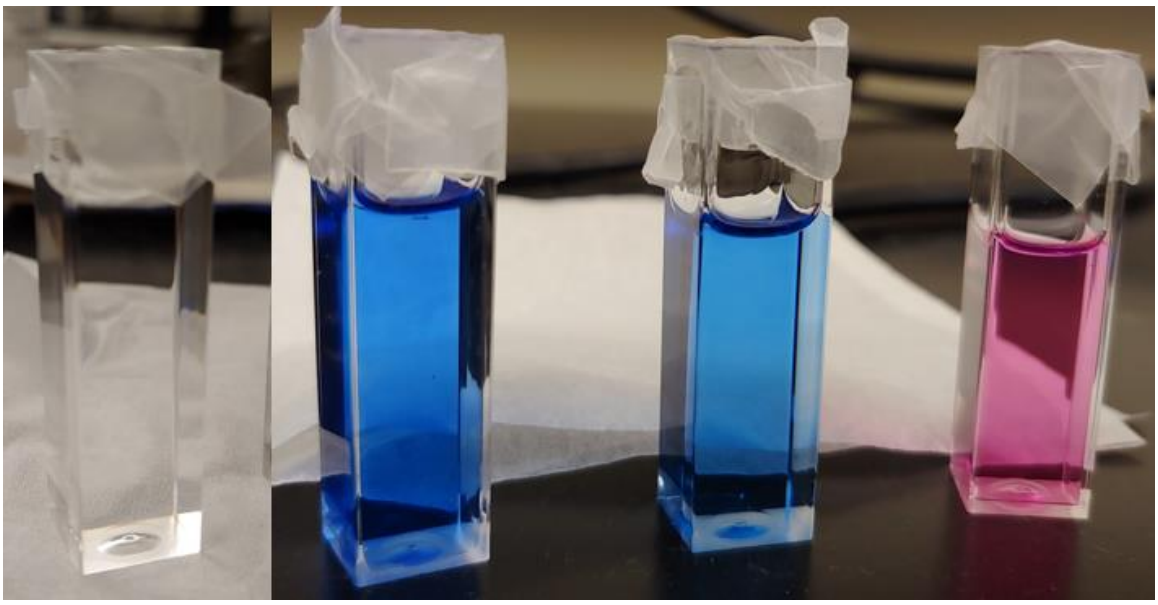

Figure 1.2: Spiropyran is transparent when dissolved in toluene (left). After conversion to merocyanine it is blue in solution (center) and reverts to Spiropyran. In ethanol merocyanine is red and will not fully convert back to spiropyran.

Photochromes that change color when exposed to light exhibit one of two properties: positive or negative photochromism. A positive photochrome starts as one color and is typically transparent in the visible spectrum. As the photochrome is reacted it changes color, typically into the visible spectrum in the form of a redshift. A negative photochrome has a more stable colorless state, meaning the molecule starts out colored and reacts to a colorless state which is a blueshift. The dimerization of 9-anthracene or the conversion of donor-acceptor Stenhouse adducts (DASA)[34-35] are examples of negative photochromic reaction, while spiropyran converting to merocyanine (figure 1.2) and the cleaving of nitrogen from an azidobenzoic acid are positive photochromic reactions.

Negative photochromes are typically more beneficial due to their greater light penetration properties.

1.2 Photoreactive molecules

1.2.1 Spiropyran

Spiropyran is a well-known photochromic molecule. As mentioned earlier spiropyran converts to merocyanine when exposed to UV light. This breaks the central oxygen carbon bond[36]. The reaction of spiropyran can be seen in figure 1.3. While not visible in the two-dimensional molecular image the molecule changes from a chair confirmation when spiropyran to planar confirmation in merocyanine. Merocyanine is zwitterionic, meaning it has two charged functional groups attached to it. Spiropyran has a large polarity difference between its unreacted spiropyran and reacted merocyanine forms which makes it perfect for applications that require a large change in polarity. Merocyanine can be reacted back to spiropyran with visible light. The exact wavelength of light needed to revert merocyanine to spiropyran depends on the functional groups attached to the molecule[37]. This makes it possible to tune the absorbance to what is needed by the system. The properties of spiropyran are highly dependent on its environment. In highly polar environments the merocyanine form is more stable, while in less polar environments the more polar one is stable. Spiropyran is thermochromic[38-39], solvatochromatic[40] (also see figure 1.2), acidochromatic[41], and mechanochromatic[42] in addition to its photochromic properties. These wide-ranging properties make it a versatile molecule in many photochromic systems.

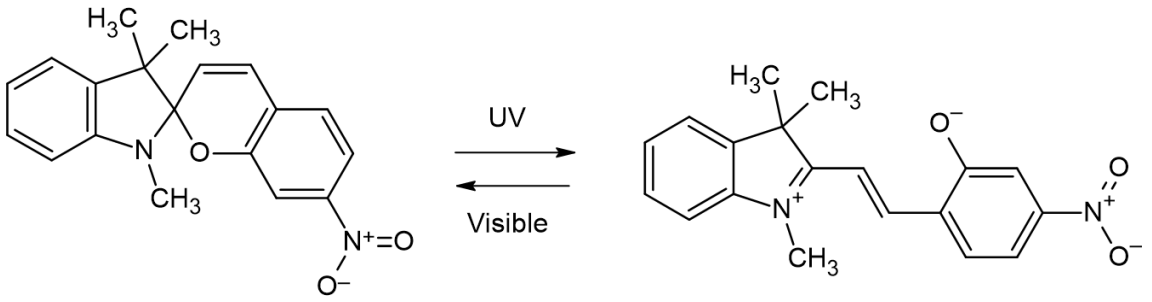

Figure 1.3: Spiropyran (left) is transparent and reacts with UV (365 nm) light to form Merocyanine (right). Merocyanine is typically blue due to the long-conjugated bond system in the molecule. It is also zwitterionic and far more polar than spiropyran. Merocyanine will back react with visible light (500-650 nm) to Spiropyran.

1.2.2 9-Anthracene Carboxylic acid

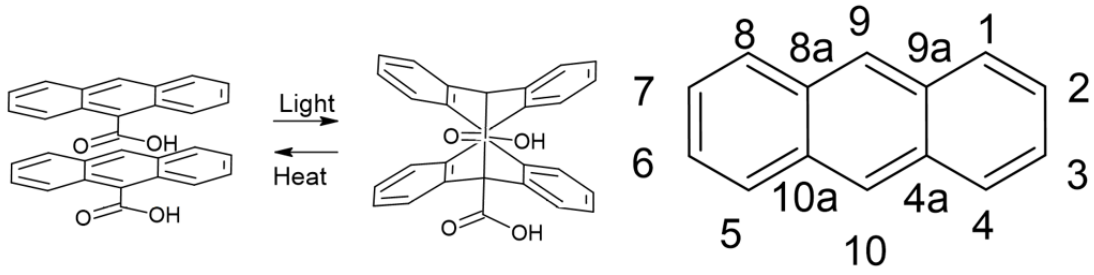

Figure 1.4: The left shows the 4+4 photodimerization of 9AC while the right shows the IUPAC numbering scheme for anthracene.

Anthracene is a molecule consisting of three fused benzene rings as seen in Figure 1.5. The molecule has a somewhat unique numbering scheme which may not be immediately apparent to those that have not worked with it previously[43]. Constituents are always given the lowest overall number, so 9AC is lower than 10-anthracene carboxylic making it correct. The 9AC system has been extensively studied[44-47]. When exposed to UV light the 9 and 10 carbons under form bonds between stacked molecules. This removes the resonance of the center ring and forms the butterfly like dimer as see in figure 1.4. The dimer thermally back reacts to the monomer in the crystal. The molecule will bend when exposed to UV light which can be used to make a molecular motor. This makes 9AC a T-

type photomechanical molecule that undergoes a bending motion when exposed to UV light. This T-type behavior occurs because the crystal packing gives rise to steric interactions between the carboxylic acid groups opposing molecules. This makes the photodimer unstable and causes it to revert to its monomer state thermally[48].

Anthracene is a fluorescent molecule. In solution it fluoresces blue, while in the crystal is fluoresces green when exposed to ultraviolet radiation[49]. 9AC will dimerize in a crystal to form dianthracene by a 4+4 photodimerization as seen in figure 1.5. When this happens, the crystal begins to fluoresce blue instead of green, giving an indication of how much of the crystal has dimerized. The dimer itself is not fluorescence but the monomer that does not react will continue fluorescing. The difference in color comes from the π stacking[50]. That stacking is removed when the dimer is formed. Figure 1.6 shows a crystal bending under irradiation of 405 nm light as well as the change in fluorescence that is observed when the crystal is reacted. Using the crystal's fluorescence, it is possible to accurately determine the rate at which the crystal is reverting to its original state

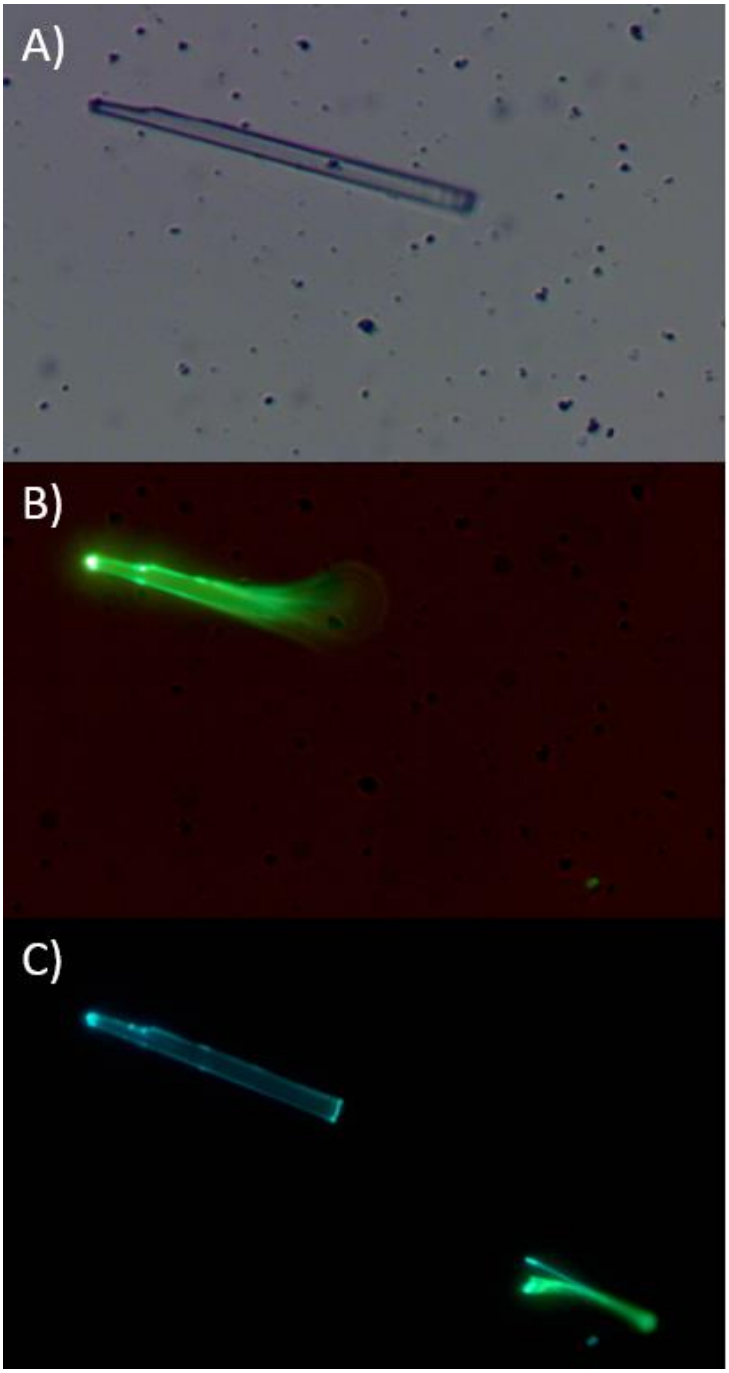

Figure 1.5: A) A 9AC crystal before irradiation under normal lighting conditions. B) Immediately after the 405 nm light is turned on bending is visible, and the fluorescence is green. C) The same crystal after irradiation for 15 seconds. The fluorescence is blue instead green due to the dimerization o 9AC. The stress from the bending of the crystal broke it in half. If given enough time after the light is turned off the crystal would straighten out and fluoresce green again.

1.2.3 4-azidobenzoic acid

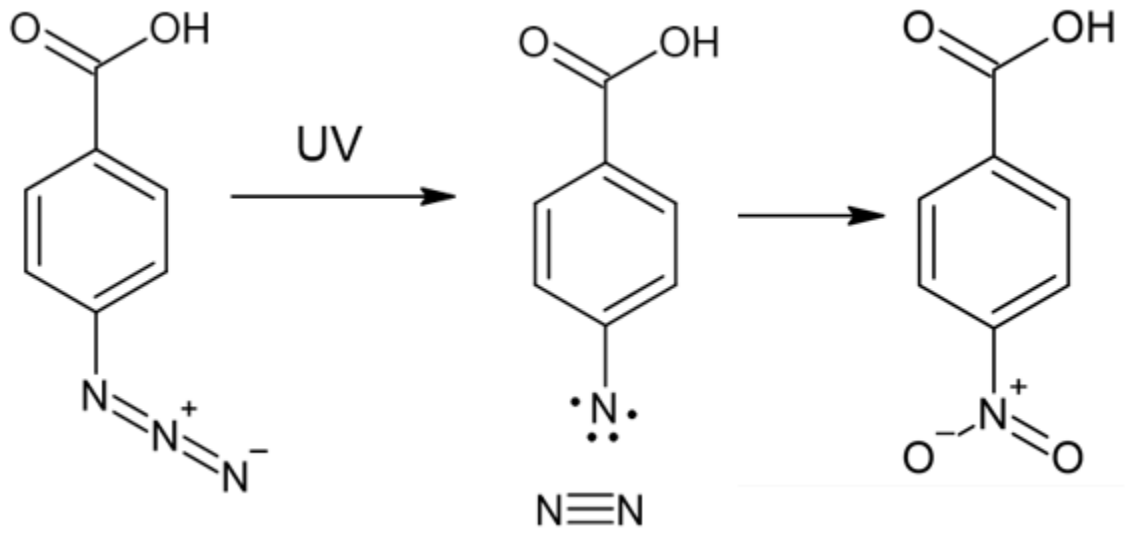

Figure 1.6: 4ABC will react with UV light to form a nitrene plus nitrogen gas. In an uncontrolled environment the nitrene will rapidly react with most molecules such as oxygen or solvent to form the end product (example of nitrobenzoic acid shown).

The final reaction set that will be discussed in this thesis is the release of gas from molecules using light and the radicals left behind. Azides (N_3) are well known nitrogen releasing compounds. The most famous azide is sodium azide, which was used as a propellent in air bags in cars[51]. Organic azides will release nitrogen gas when exposed to ultraviolet light with smaller organic azides reacting more violently. The release of nitrogen gas is accompanied by a nitrene biradical which typically reacts with any nearby molecule as seen in figure 1.6[52]. The release of nitrogen gas from the solid is a very energetic process with the resulting gas occupying substantially more volume than the original molecule. In a crystal this would lead to a photosalient effect, or a jumping and shattering of the crystal from the high amounts of stress the gas creates within the structure as seen in figure 1.7 [53]. Organic azides, such as 4-azidobenzoic acid, are typically used in

organic reactions, being particularly useful for synthesizing peptides and as a nucleophile in SN2 reactions.[54]

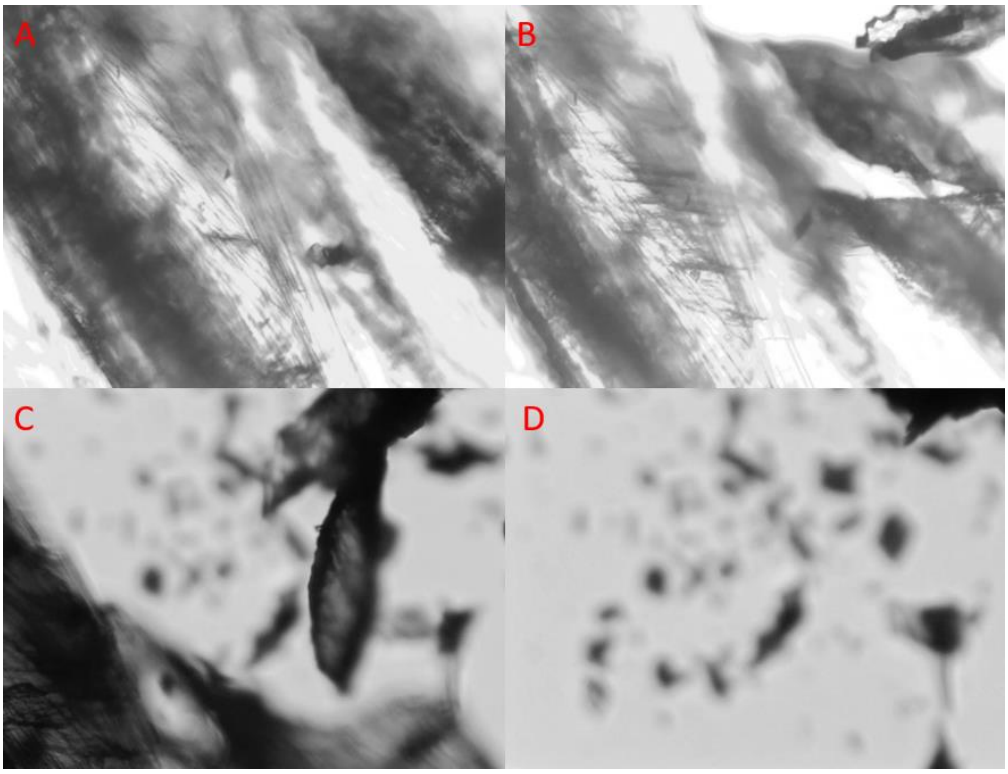

Figure 1.7: A) The original 4ABC crystal before irradiation. B) The crystal shortly after radiation has begun. Cracks can be seen forming in the crystal as stress builds up. C) The crystal shatters and jumps as the built-up energy is released. D) Only fragments of the original crystal remain. The crystal also changed from white to orange-brown after irradiation. 4ABC is only photosalient under 405 nm irradiation.

1.3 Photoreversible Adhesion with Spiropyran

Adhesion is an industry that generates more than 60 billion dollars' worth of revenue annually and is expected to rise to over 100 billion dollars by 2030[55]. The majority of adhesives are used in industrial capacities with construction, manufacturing, and transportation but there has been substantial growth and research put into adhesives for the medical field[56]. Low odor and hot melt adhesives are particularly attractive because of

their reduced environmental impacts[57]. Photoreversible adhesives can be the ultimate green adhesives as they do not require solvent or heat to adhere or deadhere from surfaces. Their ability to be turned on and off with light completely removes the need solvents or high temperatures.

Adhesion is the phenomenon whereby dissimilar particles or surfaces cling to each other. Cohesion is the phenomena where similar particles or surfaces cling to each other. Both are necessary to form a good adhesive[58]. While many categories of adhesives exist, we will be focusing on two, chemical and mechanical adhesion. Mechanical adhesion is physical connection, such as a screw and bolt, or an intrusion of a component between two surfaces. Mechanical adhesion tends to be very strong, as something must physically break or be removed in order to destroy that adhesion[59]. Chemical adhesion can occur in a variety of methods. Cross linking, electrostatics, and Van der Waals forces are all methods of generating adhesion. Crosslinking typically forms a strong adhesive bond but is irreversible by most normal methods[60-61]. Dipole interaction can be reversible if the dipoles can be turned off but is typically weak[13]. Van Der Waals forces are typically very weak, but the gecko uses its unique feet to great effect. There has been much study of gecko feet for adhesion with some success though the adhesive effectiveness of gecko feet is greatly dependent on the angle of contact of the foot, limiting its usefulness somewhat[62].

Most adhesion is not reversible. While this is useful for many applications where removing the adhered objects is not an issue there are many applications that would benefit from reversible adhesion. Having control over adhesion with light would be useful in many fields, in particular the medical field, for releasing drugs to the spot where they are needed,

or to protect a surface from chemicals. Light controlled adhesion occurs in many ways; photocrosslinking, photoinduced phase changes[63-64], and mechanical bonding[65-66] between surfaces have all been previously explored. These all have the drawback of requiring large chemical changes, a specialized surface, and are usually nonreversible. By using light to switch on and off electrostatic properties of a molecule in an adhesive adhesion can be created or removed between any polar surface and the adhesive layer. A model of noncovalent electrostatic adhesive can be seen in figure 1.8.

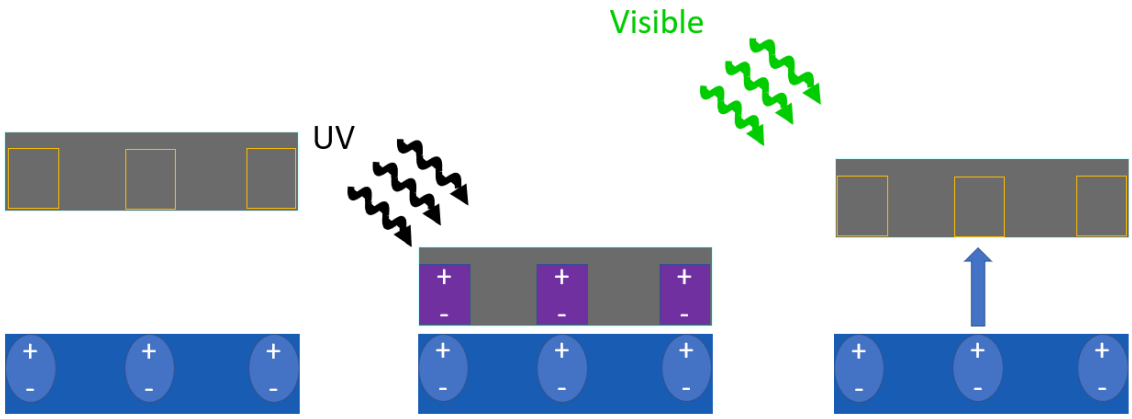

Figure 1.8: A model of reversible adhesion using noncovalent forces. The substrate, in this case glass, is made polar by the piranha treatment. The nonpolar glue contains a photochrome weakly adheres to the surface when not reacted. Once reacted the molecule becomes highly polar and more strongly adheres to the surface. This adhesion remains until the molecule is back reacted to its original form at which point the adhesive film is only weakly attached to the surface and detaches.

In this model spiropyran is an ideal reversible photochromic molecule. Spiropyran has a large polarity difference between its unreacted spiropyran and reacted merocyanine forms which makes it perfect for a noncovalent electrostatic adhesion[67]. Many types of spiropyran exist which can be tailored to the system. Absorption wavelengths can be adjusted by adding or modifying substituents on the molecule. allowing the system to be tailored to specific needs. Isomerization can deform the adhesive layer and induce

mechanical adhesion in addition to noncovalent adhesion[13]. The adhesive layer must not deform or must recover from the deformation to make the adhesion fully reversible.

1.4 Photomechanical crystals 9-Anthracene Carboxylic Acid

Motion is another response that can be elicited from a chemical system with a stimulus. Using a light to move a photoactuated motor to transfer energy from one area to another has obvious benefits over traditional electrical methods. Copper wires are heavy, comparatively fragile and can corrode[68]. Fiber optic cables are light weight, and low maintenance leaving many potential applications where weight is critical such as the aerospace industry or where corrosion is commonplace like maritime industry. Many such photomechanical systems exist, one of the most well-known is that of 9-anthracene carboxylic acid (9AC)[69-70]. This system has the potential to be used as a molecular machine as it can bend and revert to its original position with no additional input beyond the light required to initiate the reaction, however the room temperature reversion of the dimerization is too slow. By adding a single fluorine in the four position the back reaction was able to be increased by almost an order of magnitude over the non-substituted system[71]. Likewise, it can be slowed down by substituting a different atom in the 10 position. If the group is large enough, like a phenyl group, the photomechanical motion is lost completely[72]. This result inspired as investigation to further optimize the 9AC system so that it can be used in practical applications. Ideally, we are seeking to understand and model the system so that we can have a faster photomechanical system that can act as a molecular motor under light. To this end a two-pronged approach was devised to tackle

the issue. First theoretical calculations were done to determine trends of halogen substitution on 9AC. These were then verified experimentally. This process will allow for the design of molecules with the properties required for a photon driven motor, saving time by not synthesizing less productive compounds and providing an agile stimulus-response photomechanical system.

1.5 Photolysis of Crystalline 4-Azido-2,3,5,6-tetrafluorobenzoic acid

Initially the goal of this project was to design a system to harness the energy of the photosalient effect and achieve a work output using a 405 nm light source. A photosalient molecule is a nonreversible reaction but the energy released is substantially greater than that of the 9AC system[73]. When performing preliminary experiments however a much more interesting phenomenon was observed using 365 nm light to photo react the 4-Azido-benzoic acid (4ABC) in a crystal. The photosalient effect was no longer observed when reacted with 365 nm light and the nitrene biradical was stabilized for days when reacted in the crystal. Typically, a highly inert matrix, such as solid argon, is needed to stabilize the nitrene[74]. The stabilization of an intermediate product may not seem immediately interesting as this can already be done using solid argon, however this greatly limits its usefulness as the system must be stored in a cryogenic state. The emerging field of quantum information could make use of a stabilized nitrene. The nitrene is a quantum mechanical two-state system which is a requirement for many facets of quantum information systems[75].

1.5.1 Electron Spin and Quantum Computing

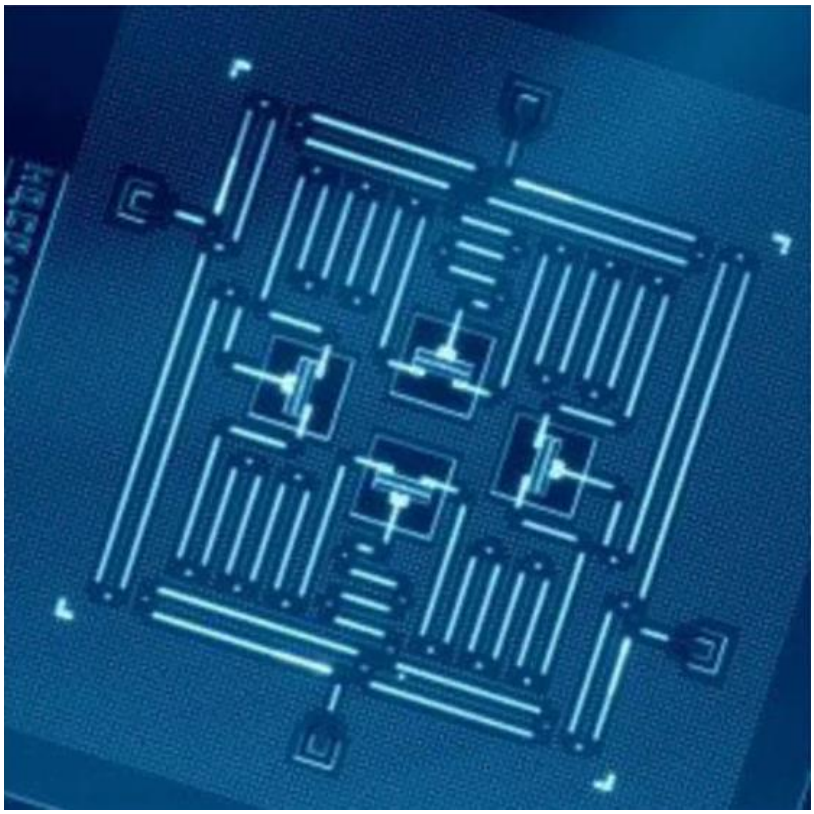

Figure 1.9: A chip consisting of four qubits produced by IBM. This chip has four qubits, four buses and four readout resonators. If cavities are not carved appropriately the chip will not function. Reproduced from Springer Nature under the creative commons license.[86]

Quantum Computing (QC) was initially proposed by Paul Benioff in 1980 when he created a quantum mechanical model of a Turing machine[76] and it is one of the major research drives of the second quantum revolution. The cornerstone of the quantum computer is the quantum bit, or qubit, a quantum analog to a transistor[77]. A qubit can be any two-state quantum mechanical system, but a viable qubit must have several properties; a long coherence time in its superposition state (>100 μs), be initialized in a specific initial state (1 or 0), is well-defined and scalable, can be individually measured, and is able to devise universal quantum gates[78]. QC and classical computing can accomplish all of the

same tasks; there is nothing that one can do that the other cannot but how they function makes the quantum computer exponentially faster in some tasks, such as prime number factoring. This is critical for computer security as most common encryption algorithms are secure because of the difficulty of factoring large numbers. QC will also greatly boost the speed of large calculations, such as those seen in large chemical and physical simulations[79]. Typically, the biggest issue in any QC system is coherence times. Usually, devices must be cooled to millikelvin temperatures to maintain coherence times long enough to use for quantum computing [80]. A wide variety of qubit candidates exist, photons, ion traps, lattice defects, superconductors, quantum dots, and electron spin qubits to name a few[81]. The most popular qubit candidate is the superconducting qubit being developed simultaneously by several major companies such as IBM [82], Intel[83], and Google[84]. A superconducting qubit consists of a Josephson junction and a series of carved resonance channels at the macroscopic level as seen in figure 1.9. This is one of the few macroscopic size qubits and can be manufactured by traditional means. These qubits ideally are identical down to the atom, which is not feasible with macroscopic manufacturing methods. These imperfections lead to each superconducting qubit having a personality according to an engineer that works on the system[85]. Having too many personalities in quantum computer can inevitably lead to issues in the system. This poses obvious problems for scalability of superconducting qubits in the long term. Chemical or physical systems can avoid this by virtue of all of the qubits (typically atoms) being the same. Electron spins, such as those seen in a nitrene, are a viable qubit candidate however no research to date has looked at nitrenes viability in quantum information systems. The closest analog to a nitrene qubit is

a crystal defect qubit, or more specifically a diamond vacancy center. Diamond vacancy centers, or nitrogen vacancy centers have one of the longest coherence times of any qubit candidate, having microseconds of coherence time at room temperature.

1.5.2 Defect Centers in Quantum Computing

The diamond vacancy center, or nitrogen vacancy center (NV center), is the primary defect center used in quantum computing and the closest comparison to the proposed nitrene qubit. In this crystal a nitrogen defect is present in the tetrahedral diamond lattice. There is a vacancy in the lattice next to the nitrogen. The NV center of interest will be negatively charged with three bonds to carbon atoms and a lone pair giving the nitrogen a negative charge[87]. NV centers have many properties that make them useful for quantum computing[88]. They have long coherence times[89], easy manipulatable spin states[90-91], convenient optical excitation, and emission properties[92], and are easily scalable. The coherence time is among the best of any qubit candidate due to the rigid crystal structure and separation from other spins. NV centers can be optically read by using optically detected magnetic resonance (ODMR)[93]. Figure 1.10 shows the energy layout of the NV center which allows for an optical readout of the spin state of the NV center. NV centers can be produced but it is somewhat difficult as the nitrogen defect must be in the crystal, then high energy gamma rays are used to make vacancies. Finally, the diamond is annealed at 700 °C until the vacancies and nitrogen atoms are by each other in the diamond[94-96]. The diamond is then shaped into an optical cavity to better observe the fluorescence readout of the qubit. This process is quite intensive. Furthermore, NV centers have a relatively long radiative lifetime of 12 ns which greatly slows down the processing speed of the qubit[97-98]. Using azides, we hope to be able to use ultraviolet light to generate

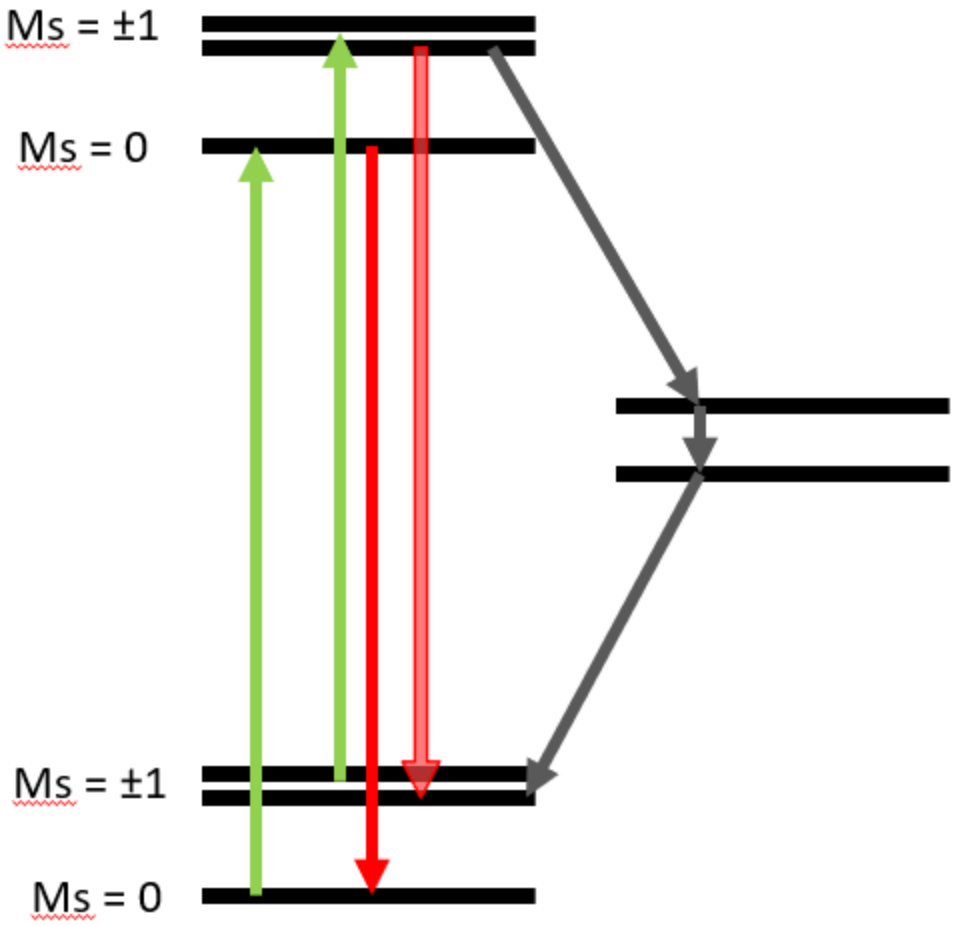

Figure 1.10: The approximate energy levels of the diamond vacancy center. The NV center absorbs green light (532 nm). If excited from the M_s=0 state it will remain in the same state when excited. This electron will then radiatively decay back to its ground state emitting red light (637 nm). If in the M_s=±1 state, there is a nonradiative pathway open to the decay of the electron available through intersystem crossing. This will darken the fluorescence by approximately 30% allowing for the spin state of the system to be optically read[99-100]. There are very few measurements of nitrene fluorescence[101-102] and we were unable to find any ODMR data on nitrenes. Many other crystal defects have a similar energy structure.[103]

stable nitrene radicals in a crystal and use this process to photo pattern radicals for qubits and other quantum technologies.

1.5.3 Designing a stable Nitrene System for use in Quantum Computing

The stability of the nitrene in the crystal likely is due to two factors. First the crystal holds the nitrene in place preventing it from moving and reacting with other atoms in the crystal. Second the nitrogen released from the photolysis of the azide is held in the crystal structure and oxygen was prevented from entering and reacting with the nitrene. In 4ABC nitrogen gas slowly escapes the crystal[104]. Designing a nitrene qubit will require three parts. First is the azide that can be photolyzed to form the nitrene. Second is a strong crystal directing group to prevent the formation of polymorphs and maintain the nitrenes in their positions after the azide has been cleaved. Finally, the remaining portion of the molecule must provide appropriate spacing as well as enough other atoms to prevent the azide from being unstable. 4-Azido-2,3,5,6-tetrafluorobenzoic acid (4F4ABC) fit all of these categories. It follows almost the same crystal structure but is slightly herringbone as seen in figure 1.11. The crystal structure has less empty space in it than 4ABC and the empty space does not form continuous channels to the edge of the crystal. Furthermore, fluorine molecules on phenylnitrenes have been shown to reduce side reactions such as ring expansion reactions[105]. Using this final photoreactive system we have designed a high energy crystal that can only be created with light. The rigid crystal structure holds the unstable nitrene in an isolated environment which allows for it to be used in quantum information systems.

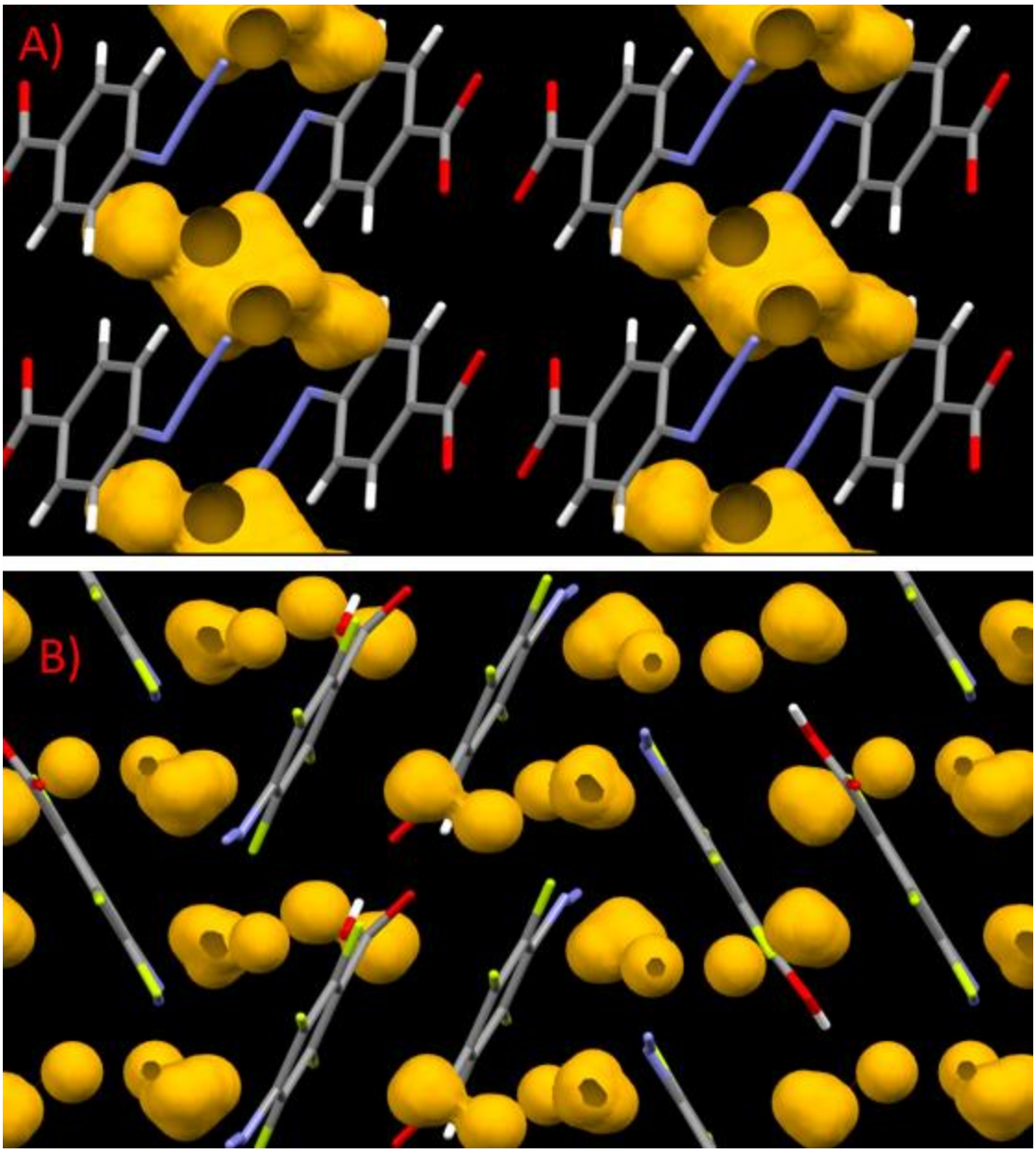

Figure 1.11: A) The packing of 4ABC has the carboxylic acid groups facing each other and the azides form long channels through the crystal. This can allow the nitrogen to escape and oxygen to enter to react with the nitrene destroying the radical. B) 4F4ABC has a herringbone structure similar to 4ABC but the channels through the crystal are less well defined. This should better trap nitrogen in the crystal and extend the radical's life.

1.6 Optimizing Photoreactive Systems (This Work)

Light driven stimulus response chemistry is a rapidly advancing field. Many types of photoreactive systems have been discovered. Typically, if they are not immediately remarkable, they are set by the wayside, or characterized and forgotten. By optimizing these existing systems, we can get more useful properties that can be exploited. The work in this thesis looks at already existing photoreactive systems, and studies ways to optimize or otherwise enhance them. In Chapter 3 a reversible photoadhesive is created from a photochromic molecule, spiropyran, and a rigid polymer, zeonex. This is an improvement over a previous system where polystyrene was used. Previously, adhesion could be increased, but not reversed[13]. The more rigid, higher glass transition temperature polymer allowed for reversal of the adhesive properties. In Chapter 4 the 9-anthracene carboxylic acid system was optimized by looking at different substitutions, primarily by halogens, on the structure. Energetic calculations were also performed to look for molecules that would revert more quickly and this was verified by using a technique called fluorescence recovery after photobleaching. The position of the substitution, type of substitution, as well as the number of substitutions had a large impact on how quickly a molecule would revert to its monomer state. Interesting highly concentration dependent photodynamics in the crystal were also observed which will require further investigation. In Chapter 5 we look at an already existing system, 4-azidobenzoic acid which had previously been shown to generate stable nitrenes in the crystal[106]. We further characterize the system for use in quantum information systems and once again looked at the addition of fluorines to the system. This made the nitrene substantially more stable and greatly decreased the creation of side

products. Further studying these molecules showed they can be used in quantum information systems, though the specific properties quantum properties will need further research. Each of the systems looked at in the work already existed, however the research put forth in this work improved the properties in some way making it more useful for real world applications of photoreactive materials. This work represents another step forward stimulus response systems and brings provides new applications for these light driven systems.

1.7 References

1 Sauvage J.-P., From chemical topology to molecular machines (Nobel lecture)," Angewandte Chemie International Edition, vol. 56, no. 37, pp. 11080-11093, 2017. Publisher: Wiley Online Library.

2 Stoddart J. F., Mechanically interlocked molecules (mims)|molecular shuttles, switches, and machines (nobel lecture)," Angewandte Chemie International Edition, vol. 56, no. 37, pp. 11094-11125, 2017.

3 Feringa B. L., The art of building small: from molecular switches to motors (Nobel lecture)," in Angew, 56: 11060-11078, 2017.

4 Wei M., Gao Y., Li X., Serpe M.J., "Stimuli-responsive polymers and their applications," Polym. Chem., 2017,8, 127-143

5 Jean-Baptiste Dumas: Über das Gesetz der Substitution und die Theorie der Typen, Lieb. Ann., Vol. 33, 1840, p. 259–300.

6 Karimi, S., Helal, E., Gutierrez, G., Moghimian, N., Madinehei, M., David, E., ... & Demarquette, N. A review on graphene's light stabilizing effects for reduced photodegradation of polymers. Crystals, 2020 11(1), 3.

7 Lefebvre, Corentin; Fortier, Lucas; Hoffmann, Norbert (2020). "Photochemical Rearrangements in Heterocyclic Chemistry". European Journal of Organic Chemistry. 2020 (10): 1393–1404.

8 Laue T. Plagens A., Named Organic Reactions, 2nd Edition, John Wiley & Sons: Chichester, England, New York, 2005.

9 McNaught A. D. and Wilkinson A., "IUPAC. Compendium of Chemical Terminology, 2nd ed. (the "Gold Book")." Compiled by. Blackwell Scientific Publications, Oxford (1997). Online version (2019).

10 Turro, N.J. and Ramamurthy, V. and Ramamurthy, V. and Scaiano, J.C., "Principles of Molecular Photochemistry: An Introduction," 2009, University Science Books.

11 Menzel, Jan P.; Noble, Benjamin B.; Lauer, Andrea; Coote, Michelle L.; Blinco, James P.; Barner-Kowollik, Christopher. "Wavelength Dependence of Light-Induced Cycloadditions". Journal of the American Chemical Society. 2017 139 (44): 15812–15820.

12 Glusac, K. What has light ever done for chemistry?. Nature Chem 8, 734–735 (2016).

13 Mostafavi S. H., Tong F., Dugger T. W., Kisailus D., and Bardeen C. J., Noncovalent photochromic polymer adhesion," Macromolecules, vol. 51, no. 6, pp. 2388-2394, 2018.

14 Mostafavi S. H., Li W., Clark K. D., Stricker F., Alaniz J. R, and Bardeen C. J., Photoinduced deadhesion of a polymer film using a photochromic donor-acceptor stenhouse adduct," Macromolecules, vol. 52, no. 16, pp. 6311-6317, 2019.

15 Gately T. J., Li W., Mostafavi S. H., and Bardeen C. J., Reversible adhesion switching using spiropyran photoisomerization in a high glass transition temperature polymer," Macromolecules, 2021 54, 20, 9319–9326.

16 Imran, M., Zhang, X., Wang, Z., Chen, X., Zhao, J., Barbon, A., & Voronkova, V. K. Electron spin dynamics in excited state photochemistry: recent development in the study of intersystem crossing and charge transfer in organic compounds. Physical Chemistry Chemical Physics, 2021 23(30), 15835-15868.

17 Sun, X., Bedoya-Pinto, A., Mao, Z., Gobbi, M., Yan, W., Guo, Y., Hueso, L. E. Active morphology control for concomitant long distance spin transport and photoresponse in a single organic device. Advanced Materials, 2016 28(13), 2609-2615.

18 Kitagawa D., Tsujioka H., Tong F., Dong X., Bardeen C. J., and Kobatake S., Control of photomechanical crystal twisting by illumination direction," Journal of the American Chemical Society, vol. 140, no. 12, pp. 4208-4212, 2018.

19 Tong F., Liu M., Al-Kaysi R. O., and Bardeen C. J., Surfactant-enhanced photoisomerization and photomechanical response in molecular crystal nanowires," Langmuir, vol. 34, no. 4, pp. 1627-1634, 2018.

20 Uchida E., Azumi R., and Norikane Y., Light-induced crawling of crystals on a glass surface, Nat Commun, vol. 6, p. 7310, 2015.

21 Wang H., Chen P., Wu Z., Zhao J., Sun J., and Lu R., Bending, curling, rolling, and salient behavior of molecular crystals driven by [2+ 2] cycloaddition of a styrylbenzoxazole derivative," Angewandte Chemie International Edition, vol. 56, no. 32, pp. 9463-9467, 2017.

22 Nath N. K., Runcevski T., Lai C.-Y., Chiesa M., Dinnebier R. E., and Naumov P., Surface and bulk effects in photochemical reactions and photomechanical effects in 120 dynamic molecular crystals," Journal of the American Chemical Society, vol. 137, no. 43, pp. 13866-13875, 2015.

23 Tong F., Al-Haidar M., Zhu L., Al-kaysi R. O., and Bardeen. C.J., Photoinduced peeling of molecular crystals," Chem Commun, vol. 55, p. 3709, 2019.

24 Henzl, J., Mehlhorn, M., Gawronski, H., Rieder, K. H., & Morgenstern, K. Reversible cis–trans isomerization of a single azobenzene molecule. Angewandte Chemie International Edition, 2006 45(4), 603-606

25 Ramamurthy V. and Venkatesan K., "Photochemical Reactions of Organic Crystals," Chem. Rev., 1987, 87, 433–481.

26 L'abbe, G. Decomposition and addition reactions of organic azides. Chemical Reviews, 1969 69(3), 345-363.

27 Rini, M., Holm, A. K., Nibbering, E. T., & Fidder, H. Ultrafast UV-mid-IR investigation of the ring opening reaction of a photochromic spiropyran. Journal of the American Chemical Society, 2003 125(10), 3028-3034.

28 Kobatake S., Photochromism," in Progress in the Science of Functional Dyes, pp. 263-281, Springer, 2021.

29 Nakai H. and Isobe K., Photochromism of organometallic compounds with structural rearrangement," Coordination Chemistry Reviews, vol. 254, no. 21-22, pp. 2652-2662, 2010.

30 Nakagawa T., Ubukata T., and Yokoyama Y., Chirality and stereoselectivity in photochromic reactions," Journal of Photochemistry and Photobiology C: Photochemistry Reviews, vol. 34, pp. 152-191, 2018.

31 Vetrakova L., Ladanyi V., Anshori J. Al, Dvorak P., Wirz J., and Heger D., The absorption spectrum of cis-azobenzene," Photochemical & Photobiological Sciences, vol. 16, no. 12, pp. 1749-1756, 2017.

32 Nakamura S. and Irie M.; Thermally irreversible photochromic systems. a theoretical study," The Journal of Organic Chemistry, vol. 53, no. 26, pp. 6136-6138, 1988.

33 Kortekaas L. & Browne W. R. (2019). The evolution of spiropyran: fundamentals and progress of an extraordinarily versatile photochrome. Chem. Soc. Rev. 48, 3406-3424.

34 S. Helmy, F. A. Leibfarth, S. Oh, J. E. Poelma, C. J. Hawker, and J. Read de Alaniz, Photoswitching using visible light: a new class of organic photochromic molecules," Journal of the American Chemical Society, vol. 136, no. 23, pp. 8169-8172, 2014.

35 Hemmer J. R., Poelma S. O., Treat N., Page Z. A., Dolinski N. D., Diaz Y. J., Tomlinson W., Clark K. D., Hooper J. P., Hawker C., et al., Tunable visible and near

infrared photoswitches," Journal of the American Chemical Society, vol. 138, no. 42, pp. 13960-13966, 2016.

36 Kortekaas L., and Browne W. R., “The Evolution of Spiropyran: fundamentals and progress of an extraordinarily versatile photochrome,” Chem. Soc. Rev., 2019, 48, 3406

37 Mustroph, H. "Merocyanine dyes," Physical Sciences Reviews, vol. 7, no. 3, 2022, pp. 143-158.

38 Decker H., Felser H., “Uber cyclische Oxoniumsalze aus Dicumarketon und uber Spiropyranderivate,” Ber. Dtsch. Chem. Ges., 1908, 41, 2997–3007.

39 Day J., “Thermochromism,” Chemical Reviews 63.1 (1963): 65-80.

40 Piard, J. "Influence of the solvent on the thermal back reaction of one spiropyran." Journal of Chemical Education 91.12 2014: 2105-2111.

41 Paramonov, S. V., Lokshin, V., & Fedorova, O. A. Spiropyran, chromene or spirooxazine ligands: Insights into mutual relations between complexing and photochromic properties. Journal of Photochemistry and Photobiology C: Photochemistry Reviews, 2011 12(3), 209-236.

42 Li, M., Zhang, Q., Zhou, Y. N., & Zhu, S. Let spiropyran help polymers feel force!. Progress in Polymer Science, 2018 79, 26-39.

43 Farve H.A., Powell W.H., “Nomenclature of Organic Chemistry (IUPAC Recommendations and Preferred IUPAC Names 2013),” Royal Society of Chemistry, 2013.

44 Al-Kaysi, R. O.; Muller, A. M.; Bardeen, C. J., Photochemically driven shape changes of crystalline organic nanorods. J. Am. Chem. Soc. 2006, 128, 15938-15939.

45 Koshima, H.; Uchimoto, H.; Taniguchi, T.; Nakamura, J.; Asahi, T.; Asahi, T., Mechanical motion of molecular crystals induced by [4 + 4] photodimerisation. Cryst. Eng. Comm. 2016, 18, 7305-7310.

46 Salzillo, T.; Brillante, A., Commenting on the Photoreactions of Anthracene Derivatives in the Solid Stte. Cryst. Eng. Comm. 2019, 21, 3127–3136.

47 Tong, F.; Bardeen, C. J.; Al-Kaysi, R. O., Photomechanical Crystals Made from Anthracene Derivatives. In Mechanically Responsive Materials for Soft Robotics, Koshima, H., Ed. Wiley-VCH: Weinheim, Germany, 2020.

48 Al-Kaysi R. O. and Bardeen C. J.y, Reversible photoinduced shape changes of crystalline organic nanorods, Adv. Mater., 2007, 19, 1276–1280.

49 Berlman, I. B. “Handbook of Fluorescence Spectra of Aromatic Molecules,” 1971 Academic Press, N.Y.

50 C. J. Easley, F. Tong, X. Dong, R. O. Al-Kaysi and C. J. Bardeen, Using light intensity to control reaction kinetics and reversibility in photomechanical crystals, Chem. Sci., 2020, 11, 9852–9862.

51 Tat, J., Heskett, K., Satomi, S., Pilz, R. B., Golomb, B. A., & Boss, G. R. Sodium azide poisoning: a narrative review. Clinical toxicology, 2021 59(8), 683-697.

52 Schuster, G. B., & Platz, M. S. Photochemistry of phenyl azide. Advances in photochemistry, 1992 17, 69-143.

53 Shields, D. J., Karothu, D. P., Sambath, K., Ranaweera, R. A. U., Schramm, S., Duncan, A., Naumov, P. Cracking under internal pressure: photodynamic behavior of vinyl azide crystals through N2 release. Journal of the American Chemical Society, 2020 142(43), 18565-18575.

54 Bräse, S., & Banert, K. (Eds.). Organic azides: syntheses and applications. 2010 John Wiley & Sons.

55 Adhesives and Sealants Market Size, Share & Trends Analysis Report By Technology, By Product, By Application, By Region (North America, Europe, APAC, CSA, MEA), And Segment Forecasts, Grand View Research, 2020.

56 “The global adhesives and sealants market is projected to grow from $65.38 billion in 2022 to $92.29 billion by 2029, at a CAGR of 5.0% in forecast period”, Fortune business insights, 2021.

57 “The global hot melt adhesives market is projected to grow from $7.10 billion in 2022 to $10.10 billion by 2029, at a CAGR of 5.2% in forecast period”, 2022-2029, Fortune business insights, 2022.

58 Zeng, H. (2013). Polymer Adhesion, Friction, and Lubrication; Wiley: Hoboken, NJ.

59 Geminger, T., Jarka S., Specialized Injection Molding Techniques William Andrew Publishing, 2016.

60 Yan, M.; Harnish, B. A Simple Method for the Attachment of Polymer Films on Solid Substrates. Adv. Mater. 2003, 15, 244−248.

61 Vitale, A.; Trusiano, G.; Bongiovanni, R. UV-Curing of Adhesives: a Critical Review. In Progress in Adhesion and Adhesives; Scrivener Publishing LLC, 2017.

62 Federle W, Labonte D. Dynamic biological adhesion: mechanisms for controlling attachment during locomotion. Phil. Trans. R. Soc. B. 2019 374: 20190199.

63 Saito, S.; Nobusue, S.; Tsuzaka, E.; Yuan, C.; Mori, C.; Hara, M.; Seki, T.; Camacho, C.; Irle, S.; Yamaguchi, S. Light-Melt Adhesive Based on Dynamic Carbon Frameworks in a Columnar Liquid-Crystal Phase. Nat. Commun. 2016, 7, No. 12094.

64 Xu, W.-C.; Sun, S.; Wu, S. Photoinduced Reversible Solid-to- Liquid Transitions for Photoswitchable Materials. Angew. Chem., Int. Ed. 2019, 58, 9712−9740.

65 Gurney, R. S.; Dupin, D.; Nunes, J. S.; Ouzineb, K.; Siband, E.; Asua, J. M.; Armes, S. P.; Keddie, J. L., Switching Off the Tackiness of a Nanocomposite Adhesive in 30 s via Infrared Sintering. ACS Appl. Mater. Interfaces 2012, 4, 5442-5452.

66 Gao, Y.; Wu, K.; Suo, Z., Photodetachable Adhesion. Adv. Mater. 2019, 31, 1806948/1-7.

67 Kovalenko, O., Lopatkin, Y., Kondratenko, P. et al. Merocyanine–spiropyran relaxation processes. Eur. Phys. J. D 72, 20 (2018).

68 "7 Reasons to choose fiber optic over copper cable" Tripp-Lite, https://blog.tripplite.com/7-reasons-you-should-choose-fiber-optics-over-copper (Accessed 28 July 2022).

69 Ito Y. Fujita H., Formation of an unstable photodimer from 9-anthracenecarboxylic acid in the solid state, J. Org. Chem., 1996, 61, 5677–5680.

70 More R. et al. "Hydrogen Bond Dynamics in Crystalline b-9-Anthracene Carboxylic Acid – a Combined Crystallographic and Spectroscopic Study," Phys. Chem. Chem. Phys., 2012, 14, 10187–10195.

71 Zhu L., Tong F., Salinas C., Al-Muhanna M. K., Tham F. S., Kisailus D., Al-Kaysi R. O. and Bardeen C. J., Improved Solid-State Photomechanical Materials by Fluorine Substitution of 9-Anthracene Carboxylic Acid, Chem. Mater., 2014, 26, 6007–6015.

72 Zhu, L., Al-Kaysi, R. O., Dillon, R. J., Tham, F. S., & Bardeen, C. J. "Crystal structures and photophysical properties of 9-anthracene carboxylic acid derivatives for photomechanical applications." Crystal growth & design, 2011 11(11), 4975-4983.

73 Tong, F.; Xu, W.; Guo, T.; Lui, B. F.; Hayward, R. C.; Palffy-Muhoray, P.; Al-Kaysi, R. O.; Bardeen, C. J., Photomechanical molecular crystals and nanowire assemblies based on the [2+2] photodimerization of a phenylbutadiene derivative. J. Mater. Chem. C 2020, 8, 5036-5044.

74 Chapyshev, S. V., Korchagin, D. V., & Misochko, E. Y. Recent advances in chemistry of high-spin nitrenes. Russian Chemical Reviews, 2021 90(1), 39.

75 Chapyshev, S. V., Walton, R., Sanborn, J. A., & Lahti, P. M. Quintet and septet state systems based on pyridylnitrenes: Effects of substitution on open-shell high-spin states. Journal of the American Chemical Society, 2000 122(8), 1580-1588.

76 Benioff P., (1980). The computer as a physical system: A microscopic quantum mechanical Hamiltonian model of computers as represented by Turing machines. J Stat Phys 22, 563–591.

77 Ladd, T. D.; Jelezko, F.; Laflamme, R.; Nakamura, Y.; Monroe, C.; O'Brien, J. L. Quantum Computers. Nature, 2010 464, 45−53.

78 DiVincenze, D. P. The Physical Implementation of Quantum Computation. Fortschritte der Physik 2006, 48, 771-783

79 Hassija, V., Chamola, V., Goyal, A., Kanhere, S. S., & Guizani, N. Forthcoming applications of quantum computing: peeking into the future. IET Quantum Communication, 2020 1(2), 35-41.

80 Unruh, W. G. Maintaining coherence in quantum computers. Physical Review A, 1995 51(2), 992.

81 Gyongyosi, L., & Imre, S. A survey on quantum computing technology. Computer Science Review, 2019 31, 51-71.

82 Linke, N. M., Maslov, D., Roetteler, M., Debnath, S., Figgatt, C., Landsman, K. A., Monroe, C. Experimental comparison of two quantum computing architectures. Proceedings of the National Academy of Sciences, 2017 114(13), 3305-3310.

83 Gomes, L. Quantum computing: Both here and not here. IEEE Spectrum, 2018 55(4), 42-47.

84 Cho, A. Google claims quantum computing milestone. 2019, https://www.science.org/doi/full/10.1126/science.365.6460.1364?casa_token=07GQlLHw0B8AAAAA:gimVCwZRu4s7BK1xelvQ204V17jo-sfYdPP9_6Kxq3QUkP10ahqV4z8i1A1g5-C45-Th9CWFavteEHQ

85 Brown R., “Qubit: The heart of Quantum Computing,” https://www.quantumcomputinginc.com/blog/qubit-the-heart-of-quantum/ (accessed 20 July 2022)

86 Gambetta, J.M., Chow, J.M. & Steffen, M. Building logical qubits in a superconducting quantum computing system. npj Quantum Inf 2017 3, 2.

87 Schreyvogel, C.; Polyakov, V.; Wunderlich, R.; Meijer, J.; Nebel, C. E. "Active charge state control of single N-V centres in diamond by in-plane Al-Schottky junctions". Scientific Reports. 2015, 5: 12160.

88 Acosta, V., Hemmer, P. Nitrogen-vacancy centers: Physics and applications. MRS Bulletin, 2013, 38(2), 127-130.

89 Bar-Gill, N.; Pham, L.M.; Jarmola, A.; Budker, D.; Walsworth, R.L. "Solid-state electronic spin coherence time approaching one second." Nature Communications. 2012 4: 1743.

90 Loubser, J. H. N.; van Wyk, J. A. "Electron spin resonance in the study of diamond". Reports on Progress in Physics. 1978 41 (8): 1201

91 Loubser, J. H. N.; van Wyk, J. A. "Electron Spin Resonance in Annealed Type 1b Diamond". Diamond Research. 1977 11: 4–7.

92 Iakoubovskii, K.; Adriaenssens, G. J.; Nesladek, M. "Photochromism of vacancy-related centres in diamond.” Journal of Physics: Condensed Matter. 2000 12 (2): 189.

93 Gruber, A.; et al. "Scanning Confocal Optical Microscopy and Magnetic Resonance on Single Defect Centers" Science. 1997 276 (5321): 2012–2014.

94 Davies, G.; Hamer, M. F. "Optical Studies of the 1.945 eV Vibronic Band in Diamond". Proceedings of the Royal Society of London A. 1976, 348 (1653): 285.

95 Iakoubovskii, K.; Adriaenssens, G. J. "Trapping of vacancies by defects in diamond". Journal of Physics: Condensed Matter. 2001 13 (26): 6015.

96 Lang, A. R.; et al. "On the Dilatation of Synthetic Type Ib Diamond by Substitutional Nitrogen Impurity". Philosophical Transactions of the Royal Society A. 1991 337 (1648): 497–520.

97 Atatüre, M. Englund, D. Vamivakas, N. Lee, S. Wrachtrup, J."Material platforms for spin-based photonic quantum technologies". Nature Reviews Materials. 2018 3 (5): 38–51.

98 Radko, I. P. Boll, M. Israelsen, N. M. Raatz, N. Meijer, J. Jelezko, F.; Andersen, U. L. Huck, A. "Determining the internal quantum efficiency of shallow-implanted nitrogen-vacancy defects in bulk diamond." Optics Express. 2016 24 (24): 27715–27725.

99 Maze J.R., Gali A., Togan E., Chu Y., Trifonov A., Kaxiras E., Lukin M.D., "Properties of nitrogen-vacancy centers in diamond: the group theoretic approach" 2011 New J. Phys. 13 025025.

100 Ivady V., Simon T., Maze J. R., Abrikosov I.A., Gali A., "First principles study on the pressure and temperature dependence of the zero-field splitting in the ground state of NV-center in diamond," Phys. Rev. B, 2014, 90, 235205

101 Hancock G. McKendrick K.G., "Laser-induced fluorescence and vibrational relaxation of the phenyl nitrene radical," J. Chem. Soc., Faraday Trans. 2, 1987, 83, 2011-2024.

102 Kozankiewicz B., Deperasinska I., Zhai H. B Hadad C. M., "Spectroscopic and Computational Studies of Perfluorophenyl and Perfluoro-2-naphthyl Nitrenes in Shpolskii Matrixes," J. Phys. Chem. A 1999, 103, 26, 5003–5010.

103 Aharonovich, Zhou, C., Stacey, A., Orwa, J., Castelletto, S., Simpson, D., Greentree, A., Treussart, F., Roch, J.., & Prawer, S., "Enhanced single-photon emission in the near infrared from a diamond color center." Physical Review B 2009, 79(23), 1–5.

104 Sasaki, A., Mahe, L., Izuoka, A., & Sugawara, T. Chemical consequences of arylnitrenes in the crystalline environment. Bulletin of the Chemical Society of Japan, 1998 71(6), 1259-1275.

105 Karney, W. L., Borden W. T., "Why does o-Fluorine substitution raise the barrier to ring expansion of phenylnitrene?" J. Am. Chem. Soc. 1997, 119, 3347-3350.

106 Mahe, L., Izuoka, A., & Sugawara, T. How a crystalline environment can provide outstanding stability and chemistry for arylnitrenes. Journal of the American Chemical Society, 1992 114(20), 7904-7906.

Chapter 2 Experimental Methods

This chapter will explain how certain setups were built, how instruments work, or why certain parameters were chosen for the experiments. The procedures for each experiment can be found in their respective chapters.

2.1 Photoreversible Adhesives

2.1.1 Instron 5900 Series Universal Testing Systems

Figure 2.1: The Instron 5942 with the installed 100 N load cell and a sample mounted in place.

The Instron 5942 (Single Column Tabletop Testing System) is a mechanical tester with a 100 N load cell as seen in figure 2.1. This instrument is owned by the Uhrich Group, and they have been very helpful with all of our requests to use it. This instrument slowly pulls apart and registers the force required to do so. This was used for the shear strength measurements. Very precise alignment was needed to ensure that the glass slides were still adhered after loading the sample into the instrument. Due to the difficulty of mounting two perfectly vertical attachments to glass slides this instrument was only used for the shear

strength measurements; weights were added top of the sample suspended above a surface instead of using Instron. 1 mm per minute was chosen as the pull apart rate in order to ensure that the maximum strength was recorded.

2.1.2 Piranha Cleaning

Piranha is a solution that is used to clean organic residues off of substrates. It is a 3:1 mixture of 30% hydrogen peroxide and sulfuric acid which is heated to boiling. The solution is corrosive and a powerful oxidizer and will easily dissolve organic matter as well as hydroxylate most surfaces. The solution is also explosive if organics are added directly to the solution. The piranha solution is prepared by placing the surface that needs to be cleaned into a glass container. The sulfuric acid is then added, and the hydrogen peroxide is added slowly to the acid. The solution may start boiling when the hydrogen peroxide is added. After the initial reaction has subsided, heat is applied to keep the solution at a low boil[1-2]. The boiling was done for 15 minutes then the slides were removed, rinsed in deionized water, and used immediately. Environmental health and safety has specialized safety equipment for piranha including waste bottles, caps, and signs like those seen in figure 2.2.

Figure 2.2: Warning signs for piranha solution provided by UCR's Environmental Health and Safety

2.2 9-Anthracenecarboxylic Acid-Fluorescence Recovery After Photobleaching

Fluorescence Recovery After Photobleaching (FRAP) is a technique that is common in the field of biochemistry and biology to measure the diffusion of fluorescently labeled proteins[3]. By adapting this technique, we are able to track the recovery of various 9AC compounds. As previously discussed, anthracene fluoresces green in a crystal when in its monomer form and is surrounded by other monomers. As the monomers are isolated when dimers form the molecules lose their pi-pi interaction and individual anthracene molecules begin fluorescing blue instead as if they were in solution. By using a pump probe setup, we can use an intermittent weak laser beam to measure how much green light is emitted and track the recovery of the 9AC molecules[4]. The pump spot is much more powerful than the probe and only operates for a limited time to bleach the sample. The weak probe beam would ideally be able to track the recovery without impacting the recovery of the molecule. By tracking the fluorescence recovery, we are able to better characterize the back reaction and energetics of the crystal system.

The setup for the Fluorescence Recovery After Photobleaching (FRAP) experiments was a typical pump probe style set up as seen in figure 2.3. First the pinhole allowed only the mode that was desired to continue. Then the light was attenuated, typically with an ND 2.0 before being collimated. It was then passed through a chopper at 100 Hz and split into the pump and probe beams. The pump beam was focused so it was much smaller than the probe beam in the sample. The probe beam is attenuated with additional ND filters before being rejoined with the probe beam and entering the

microscope. The light entered the Olympus IX-70 inverted microscope the laser in the side. The photo multiplier tube (PMT) was positioned at the side port and had a 500 long wave pass filter to prevent any light from the monomer from reaching the PMT. When necessary, the probe beam was manually blocked with a piece of paper to ensure that it had no impact on the recovery rates.

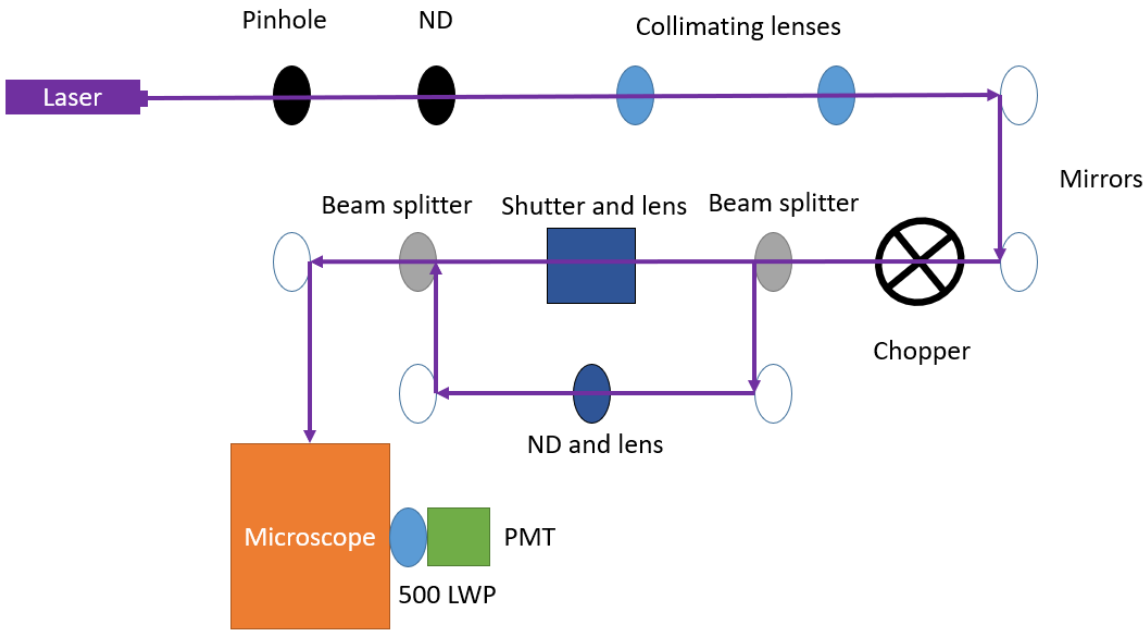

Figure 2.3: The basic set up of the pump-probe beam for FRAP. This set up used a 405 nm laser, a 2.0 neutral density filter after the pinhole, 10 cm collimating lenses, a 100 Hz chopper, a 1.7 neutral density filter after the beam splitter (this was adjusted based on the sample).

2.2.1 X-Ray Diffraction

X-ray Diffraction (XRD), or X-ray crystallography is the primary method used for determining the atomic and molecular structure of a crystal. It works by taking a monochromatic X-ray source and focusing it on a crystal mounted on a goniometer. The goniometer rotates producing a diffraction pattern at several different angles. Using the

known chemical data of the crystal, and Fourier transformations multiple two-dimensional images are put together to generate a three-dimensional structure. Critical to XRD is Braggs law. This states that two beams of identical wavelength at a given angle will interfere constructively when they travel an integer value of the wavelength relative to the interplane spacing of the crystal as seen in figure 2.4. The Bragg equation can be written as[5]:

$$n\lambda = 2d \sin(\theta)$$

Where n is the diffraction order and a whole number, λ is the wavelength of the beam, d is the interplane spacing of the crystal and θ is the angle of incidence of the x-rays. Braggs law holds true for any quantum beam, including electron beams and visible light on lattices of the appropriate size. In XRD larger atoms diffract much better than smaller atoms making it harder to obtain the XRD structure for only small atoms. Hydrogen atoms are typically calculated into the crystal structure and not actually measured due to their small size. XRD has been vital to the advancement of many branches of science and gives insight into the interactions of molecules.

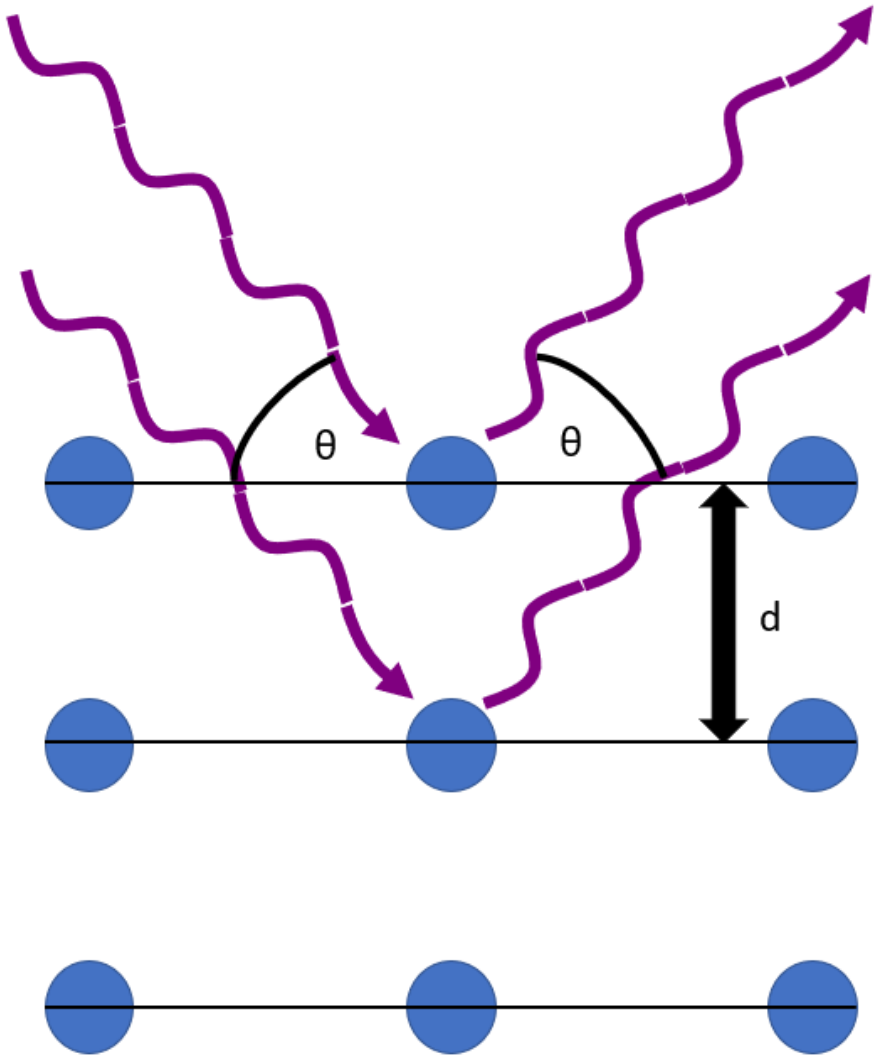

Figure 2.4: Two beams with the same wavelength elastically scatter off of the atoms of the crystal. They will interfere constructively at whole number values for n.

2.3 Nitrene generation and characterization

2.3.1 EPR

Electron Paramagnetic Resonance (EPR), sometimes called Electron Spin Resonance (ESR), is a microwave spectroscopy technique for measuring materials that have unpaired electrons. Fundamentally EPR functions in a similar way to nuclear magnetic resonance (NMR) but NMR looks at nuclear spins instead of unpaired electrons. EPR relaxation time are also typically much faster than NMR relaxation times. Paired electrons do not give a signal in an EPR which limits the applications of the technique. All electrons have a spin quantum number with a value of $m_s = \pm ½$. Normally in these energy levels are degenerate, or they have the same energy. In an EPR a magnetic field is applied which changes the system which splits the degenerate energy levels into a lower and higher energy level due to the Zeeman Effect. Figure 2.5 shows the Zeeman effect and expected transitions in an EPR. The stronger the magnetic field is, the more energetic the radiation must be to drive the electrons between states. In a triplet (S=1), such as a nitrene, zero field splitting (ZFS) occurs, which means even in the absence of an applies magnetic field the energy levels are not the same. This occurs due to the effects of inter-electron repulsions.[6-7]

There are two primary types of EPR, continuous wave (CW) EPR and pulsed EPR. A CW EPR is simpler and is primarily used in this research. A pulsed EPR will be necessary for any quantum computing applications of nitrenes in order to probe the lifetimes of the two-state system. CW EPR functions by placing a sample into a resonator cavity, setting the microwave generator to the resonant frequency, then varying the

magnetic field to scan for a signal (note that this is opposite of how an NMR collects data, where usually the field is held constant, and the microwave radiation is varied).

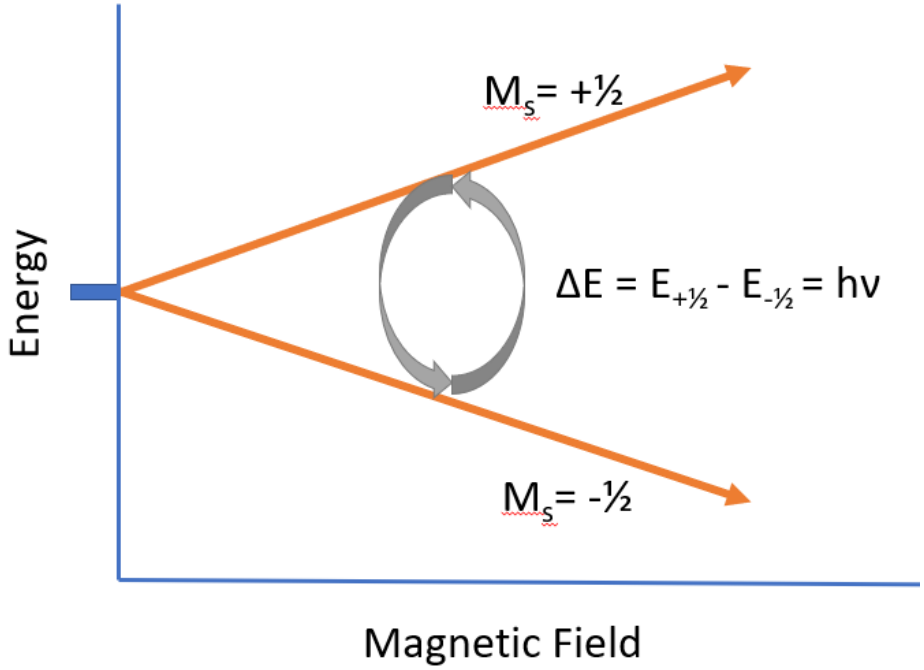

Figure 2.5: An illustration of the Zeeman Effect. The stronger the magnetic field the larger the splitting becomes. In order to use the X band (9-10 GHz) a typical magnetic fiels of 330 mT is applied for a g value of 2. Trirplet nitrenes are more shifted and require almost twice that strength (670 mT).

The general layout of a CW EPR can be seen in figure 2.6. Data is typically displayed as the first derivative of the raw data. There are many factors that can affect the EPR signal. If a single crystal is being analyzed the crystal will be highly anisotropic, or it will give a stronger signal in one direction than another. The crystal must either be aligned the same way to provide the same signal or a powder or liquid should be run instead. Liquids must have a small ($\varepsilon < 4$) dielectric constant, or the signal will be attenuated[6-11]. Hyperfine coupling arises from the interaction of an electron spin and a nuclear spin. This is similar to J coupling in NMR. An example of a sample with hyperfine

coupling and one without it can be seen in figure 2.7. This can be beneficial as more information is given about the distribution of the unpaired electron can be obtained. Depending on the frequency of the EPR it may not be possible to resolve the signal with the X-band EPR alone[6]. EasySpin is a MATLAB toolbox that is specially designed for EPR analysis that can fit hyperfine couplings among other things[12]. EPR is highly temperature sensitive. The sensitivity was described by Pierre Curie in what would be known as Curie's law. In general, for a fixed value of the applied magnetic field, the magnetic susceptibility is inversely proportional to temperature[11]. CW EPR can give a general idea of the T_1 and T_2 times. Sharper lines usually mean shorter T_1, and T_2 times though local spin density can affect this. A signal to power dependance can also reveal information about T_1 and T_2.[13]

In pulsed EPR the sample is also placed in a resonator cavity, but a large range of frequencies are used at once. This pulse rotates the electrons alignment in the magnetic field. As they return to their ground state, they emit microwaves which are detected. The Fourier transformation of the EPR signal transforms the data back to the frequency domain. Varying pulse sequences can collect different data on a pulsed EPR. To determine the resonance frequencies an Echo Detected Field Sweep (EDFS) is performed. This performed by using a $\pi/2–\tau–\pi$ pulse sequence. In and EDFS measurement the microwave frequency is held constant, and the pulse sequence is not changed, while the echo intensity is recorded as a function of the magnetic field, generating results similar to a CW EPR. This is method is more sensitive than CW EPR as several sources of noise are removed, however a pulsed EPR has dead time between the pulse and the measurement[13]. Typically,

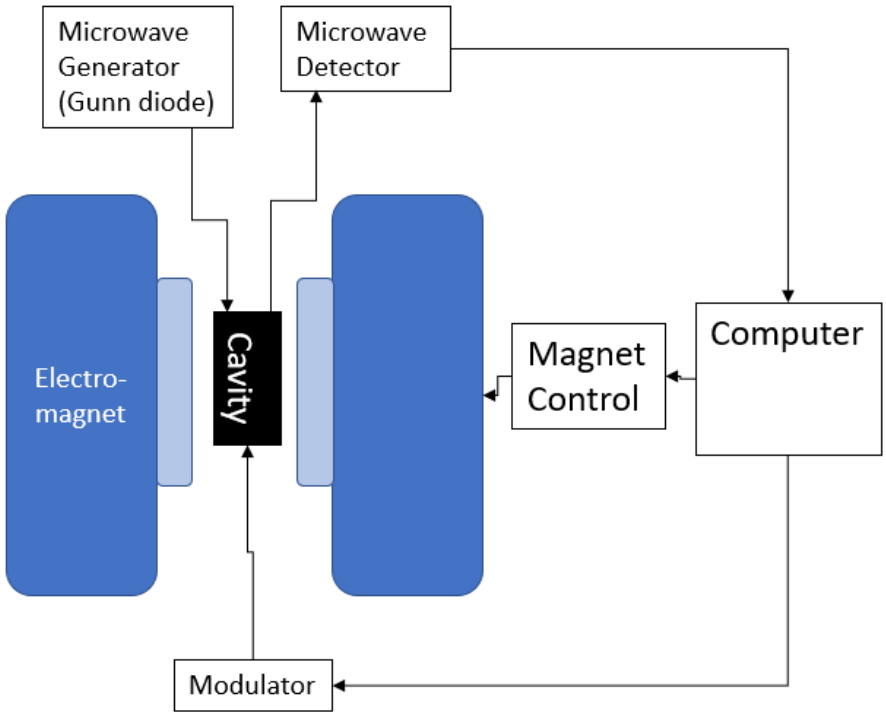

Figure 2.6: A general diagram of how an X-band CW EPR works. Microwave radiation is generated through either a Gunn diode or a klystron (vacuum tubes and a resonator). The radiation is then passed through the sample cavity and moves to a phase sensitive detector which is sends data to a computer. The computer controls the magnet and modulator to take the data and produce the spectrum.

the T_1 or the spin-spin relaxation time is determined by a population inversion pulse sequence π–T–$\pi/2$–τ–π–τ–echo. This is done at a single magnetic field strength. T_2, or the spin-spin relaxation is measured by a Hahn echo pulse sequence of $\pi/2$–τ–π–τ–echo. T_1 will typically be longer than T_2, the reverse only happens by exception[13,30]. There are many advanced techniques using pulsed EPR such as Electron Nuclear Double Resonance (ENDOR) which better shows the relationship between electron spins and nuclear spins[17]. Electron Spin Echo Envelope Modulation (ESEEM) is used to obtain nuclear spin transition frequencies[14-17]. One final measurement that must be done on a pulsed EPR is the detection of Rabi Oscillations. Rabi Oscillations, or the Rabi Frequency, is the

frequency that drives a two-state quantum mechanical system from the 0 to 1 state and back under a constant field. A typical pulse sequence of tp−T−π/2−τ−π−τ−echo where T must be >5Tm is usually used and tp is a nutation pulse. To ensure that Rabi oscillations are detected a power dependence should be taken and the response should be linear. If it is not then the detected signal may be something else, such as Larmor processions[18]. UC Riverside does not have a pulsed EPR system. USC, the National High Magnetic Field Laboratory, UCSD, and UCSB each have an instrument which time could be obtained on.

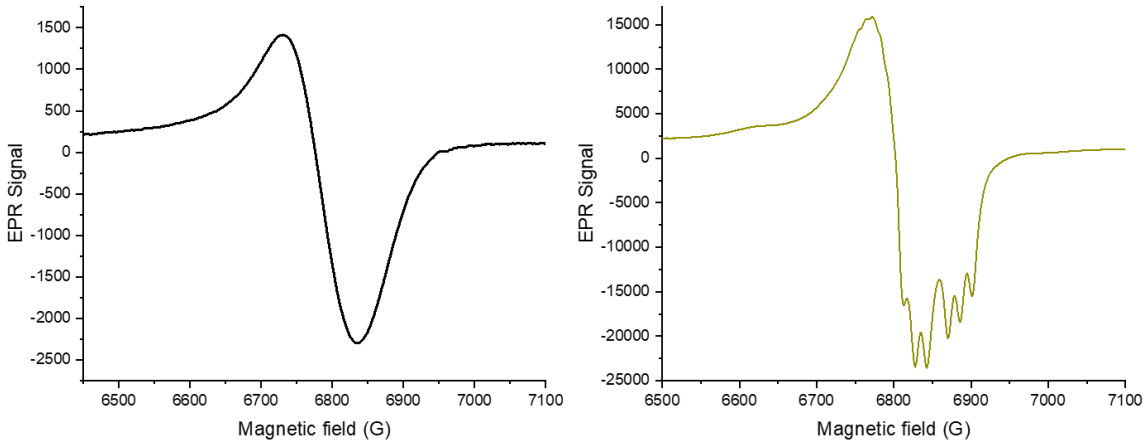

Figure 2.7: An example of a sample without hyperfine coupling (left) and with hyperfine coupling (right). The X band EPR could not resolve all of the individual peaks, so they are jumbled together. EasySpin can still fit all three nitrogen atoms in the signal.

Optically detected magnetic resonance (ODMR) is another magnetic resonance technique but instead of using a microwave detector the readout is performed optically. The underlying principle of ODMR is the same as in EPR and it still makes use of the Zeeman effect. In ODMR one state, typically the $m_s=\pm1$ state, is a dark state meaning it does not optically fluoresce. The other state, typically the $m_s=0$ will optically fluoresce. This occurs because the $m_s=\pm1$ states will undergo intersystem crossing to a singlet state

and relax in the infrared region while the m_s=0 state does not and instead emits light with a Stokes shift. The electron's state can therefore be detected by monitoring the fluorescence of the visible emission while using microwaves to drive the electrons from the m_s=0 to the m_s=±1 state. This also provides a readout of the information in quantum information systems which is critical for practical applications[19-23]. UCR does not have any ODMR capabilities.

Figure 2.8: The Brucker EMX EPR instrument at UC Riverside used in the experiments. The magnet and resonator cavity are visible in the middle, the temperature control is above the magnet. The power supply for the magnet and transputer are on the front right of the image. The X-band microwave generator is absent from the picture as it was being repaired at the time. The dewar for the cryogen is behind the instrument.

UC Riverside has a Brucker EMX x-band EPR spectrometer seen in figure 2.8. The design and manufacture are quite old as the software was designed for Windows 95. The cavity and large electromagnet are still functional and have superb sensitivity. The age and use of the instrument have led to the resonance of the cavity to have shifted left of where it should be in the calibration window. This does not affect the data when properly

calibrated. There is an Eurotherm temperature control unit with the instrument that enables temperatures down to 90 K but in practice it is not possible to go below 100 K with liquid nitrogen. There is a separate liquid helium sample chamber but that was not used for these experiments. A full tank of liquid nitrogen will allow for approximately 2-3 hours at 100 K and 5-6 hours at 125 K. When using the liquid nitrogen ensure the heater is on the lowest setting that gives the desired temperature to prolong the nitrogen in the tank.

Parameter	Setting used
Modulation frequency	100 kHz
Modulation amplitude	8 G
Receiver gain	20 dB
Time constant and conversion time	1:1 ratio at 20.48 ms (large scans) or 163.84 ms (focused scans)
Data points	512-4096
Microwave attenuation	20 dB

Table 2:1: Common parameters used in the EPR for analysis. Additional details on the why settings were chosen can be found in the text.

Parameter settings vary depending on samples. This is a brief summary of the parameters used for analysis. Modulation frequency is by default 100 kHz, and this was what used for the nitrene analysis. For samples with sharp lines the modulation frequency should be lowered to avoid distortions. A higher modulation amplitude will increase the signal of the EPR to a point however it will sacrifice some sensitivity in the process. 8 G was used for all modulation amplitudes. Receiver gain increases the signal and noise in the sample. 20 dB was used for all samples. This should be started in the middle so the signal can be kept within a reasonable value if more or less receiver gain is required. The

conversion time is the amount of time the analog-to-digital converter spends integrating signal at one data point before moving on to the next. The longer the conversion time, the better the signal to noise ratio is. The time constant, or response time, also helps to increase signal to noise ratio by 1/TC. The time constant should be about ¼ of the conversion time. Increasing the time constant to match the conversion will increase signal strength. Nitrene analysis used the same conversion time and time constant for each run, 20.48 ms for the large scans and 163.84 ms for the focused scans. The number of points is a rather self-explanatory setting. More points lead to more detail in the signal to a point, and longer sample run times. It is necessary to have 10 points for every peak, though it can be beneficial to have more. There will come a point where additional data points do not provide any more information and only increases run time. 4096 data points was used for the large sweeps (~8000 G) and 512 points for the small sweeps (~500 G). To calculate the sample run time per scan multiply the conversion time by the number of points. The sample run time should be kept to under 3 minutes to minimize drift. The instrument is generally more stable after having warmed up for half an hour and more stable when using the cryostat. The number of scans also requires no additional explanation. The EMX at UCR however does not average the data obtained from each run, it simply adds the data together. Only one scan at a time was run to better account for drift. The microwave power is not directly controlled, instead microwave attenuation is used to control the power. This can range from 0-60 dB; 20 dB was used for all analysis which corresponds to 2 mW of power. More power will lead to more signal, with the signal increasing by the square root of the power, however excessive power can cause sample heating, or saturation. Saturation

is more of an issue in samples with long relaxation times, or sharp peaks. The center field is the center point of where the EPR will scan. The sweep with is the entire width of the EPR spectrum. When analyzing with a sweep width of 500 G the instrument will scan 250 G above and below the center field for 500 G total, not 500 G on either side. Ensure the entire signal is within the window. There is no noticeable drop in sensitivity on the edges of the analysis window, so no buffer zone is needed. The harmonic option displays either raw data (0), the first derivative of the data (1) or the second derivative of the data (2). EPR data is typically analyzed by looking at the first derivative and all data used in this paper is shown using the first derivative. The Oxford temperature controller is controlled externally, directly on the temperature controller, not through the computer. The power of the liquid nitrogen heat exchanger device controls the cooling while the temperature controller controls the heater. When a good seal is formed between the cryostat and the heat exchanger the minimum power will give 150 K without the heater turned on. At 50% power, the maximum power that is recommended for the heat exchanger, the temperature will be just below 100 K. Exceeding 50% power on the heat exchanger will cause the sample to vibrate in the resonance chamber and decrease data quality even when properly secured.

Sample analysis should be done in specially made EPR tubes. Wilmad quartz (CFQ) EPR tubes were used in both 100 mm and 250 mm lengths with a 4 mm outer diameter. The instrument has sample holders for a variety of tube sizes. Tubes need to be washed and dried with organic reagents that will not leave behind salts as they can be picked up by the EPR. The outside of the tube should also be wiped with ethanol and a

kimwipe before inserting the sample into the resonator (note that if samples are being run using the cryostat this should be done before freezing). The sample should be centered in the resonator, there is nothing to stop the sample at the correct point so measurements must be taken beforehand. If samples are inserted to the same depth the frequency adjustments will be minor when a new sample is inserted.

EPR samples do not require special preparations. Powders can be placed directly into the EPR tube. Samples should be no more than half a centimeter in height. Too much of a sample in the tube can lead to distortions of the EPR signal while too little will result in a loss of signal. Samples should be rotated 90° and run a second time to ensure that the powder is fine enough to avoid anisotropic effects. If a single crystal is being analyzed the orientation should be kept constant. Liquids must have a dielectric constant of 4 or less to analyzed in the EPR.

2.3.3 Laser Fluorescence

Laser fluorescence is a spectrometry technique that uses a laser to excite a molecule which then fluoresces. This is functionally similar to normal fluorescence but instead of using a lamp to excite the sample a laser is used. The coherent monochromatic light source allows more power of the desired wavelength to excite the sample.[24] Care must be taken to not heat the sample using too much power from the laser. Figure 2.9 shows the general setup of the laser fluorescence that was used.

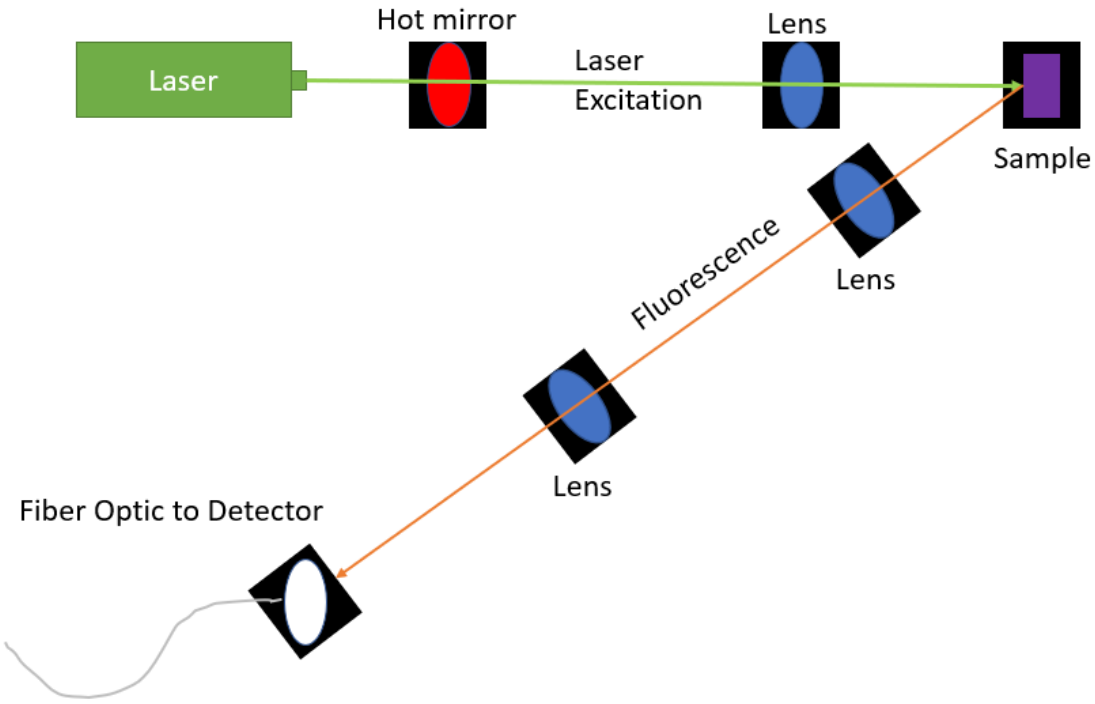

Figure 2.9: The laser fluorescence setup begins with the laser going through the hot mirror to remove wavelengths >750 nm. A neutral density filter is applied here to attenuate the laser power to the desired intensity. A lens then focuses the light on the sample. The sample fluoresces and a second lens collimates the light. The final lens focuses the sample on the detector and includes a notch filter or long wave pass to remove laser scatter from the signal. The signal is then collected by the optical fiber and sent to the detector.

The laser used was a 405 nm, 465 nm or 532 nm laser depending on the sample. The laser power was attenuated to 2 mW to start measurements and increased until an appropriate signal to noise ratio was obtained. Usually, 20 mW of laser power would saturate the detector when using the crystal. When using glass samples in the cryostat the sample would visibly change when more than 50 mW of power was used. The detector used was an Ocean Optics USB 4000 spectrometer. Integration times and repetitions per sample varied but 200 ms and 20 repetitions gave a good signal to noise ratio and gave a good dynamic range. The dark spectrum needed to be updated between each sample.

2.3.4 Diffuse Reflectance

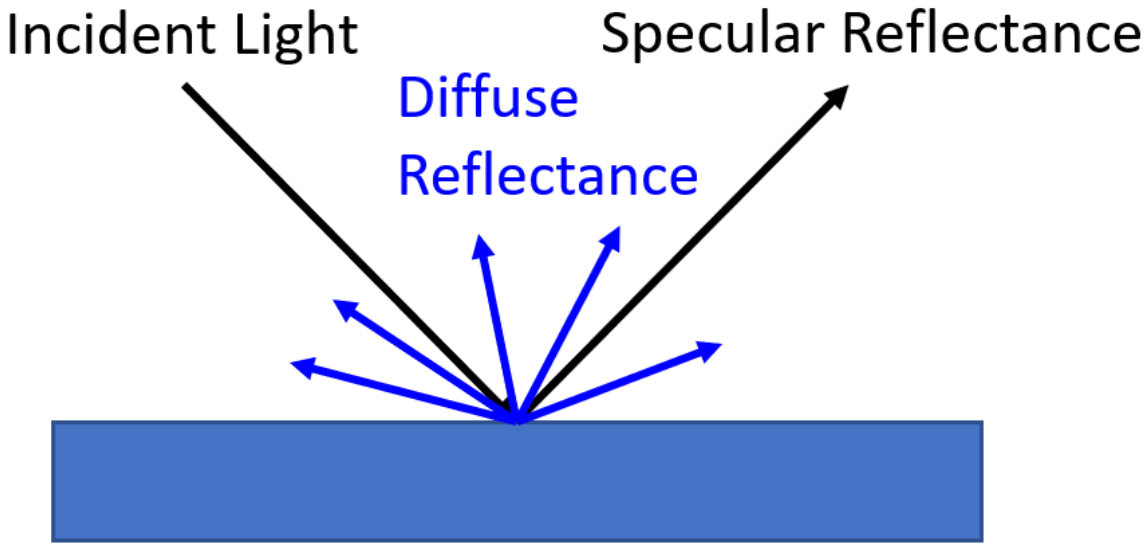

Figure 2.10: Specular reflectance is what is seen using a smooth surface like a mirror. Diffuse reflectance is much less intense and can be seen from a much wider range.

Diffuse reflectance spectroscopy is a type of optical spectroscopy that looks at the scatter of light off of a surface. There are two main types of reflectance from a surface, specular reflectance, like that what is seen off of a smooth surface like a mirror, and diffuse reflectance which is what is reflected off of a mat surface. A colored powder is ideal for analysis using diffuse reflectance. Figure 2.10 shows the difference between specular and diffuse reflectance. In diffuse reflectance the sample is placed on a highly reflective substrate, usually barium sulfate for measurements in the ultraviolet to near infrared range and potassium bromide for farther in the infrared spectrum. The sample is placed in an integrating sphere to better capture the light from the sample. The reflectance of the sample is compared to a blank to determine the reflectance of the sample. The reflectance can be converted to absorbance for comparison to normal absorbance data. One of the major draw backs of diffuse reflectance is its low sensitivity compared to absorbance measurements.

Nitrenes are unstable outside their crystal, making diffuse reflectance necessary to find the absorbance of the molecules.[25-26]

2.3.5 Glass Formation

A glass is an amorphous solid that is usually transparent. Glass is commonly used in optics because of its desirable qualities. Glasses are transparent due to the lack of grain boundaries that are found in crystalline materials.[27] The nitrenes are highly reactive and must be in an inert matrix in order to prevent the nitrene from reacting. This is typically done using a solid argon matrix[28-29] or a glass. To form a chemical glass a solvent that does not crystalize should be used. Ethanol will occasionally work but solvents with extra methyl groups attached, like 2-methyltetrahydrofuran (2-MeTHF) or methylcyclohexane, as seen in figure 2.11, work much better and will dissolve a wide range of compounds. They can also be mixed to form a glass. Butylated hydroxytoluene is sometimes added 2-MeTHF to prevent the formation of explosive peroxides. This does not affect the formation of the glass but does increase absorption in the ultraviolet region and gives an emission in the blue.

In the nitrene experiments a glass of 2-MeTHF was created by dissolving the azide compound in 2-MeTHF. This was added to the analysis cuvette and capped tightly. This was covered in indium where the cuvette was not illuminated and mounted into the cryostat and liquid nitrogen was poured down the cryostat. The cryostat was pumped down to stepwise to prevent the 2-MeTHF from evaporating as the cap on the cuvette was not airtight. Once below the freezing point of 2-MeTHF (137 K) the pump was left on, and nitrogen was kept in the cryostat for at least 4 hours before analysis. Even at these low

temperatures the 2-MeTHF slowly reacts with the nitrene once created so useful measurements can only be taken for 5-10 minutes.

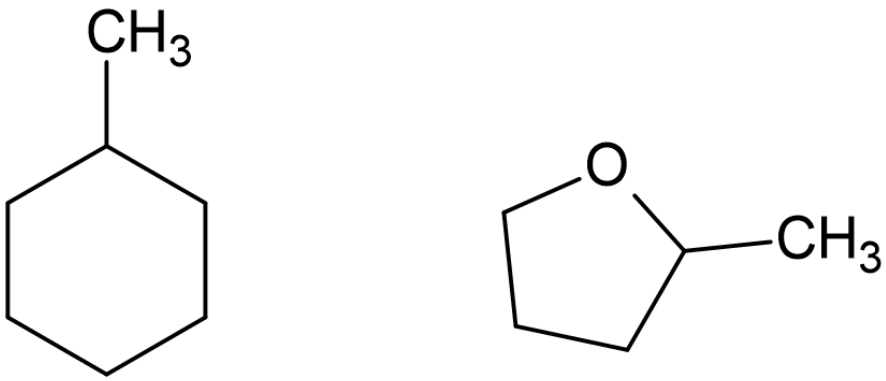

Figure 2.11: Methylcyclohexane (left) and 2-methyltetrahydrofuran (right), are both good glass forming molecules.

2.4 References

1 UC Riverside Environmental Health and Safety; Generation, Use and Disposal of Piranha Solutions Standard Operating Procedure, UC Riverside, 2019.

2 Schmidt H. G., "Safe Piranhas: A Review of Methods and Protocols," ACS Chem. Health Safety. 2022, 29, 1, 54–61.

3 Axelrod D, Koppel DE, Schlessinger J, Elson E, Webb WW. Mobility measurement by analysis of fluorescence photobleaching recovery kinetics. Biophys J. 1976 Sep;16(9):1055-69

4 Easley, C. J.; Tong, F.; Dong, X.; Al-Kaysi, R. O.; Bardeen, C. J., Using light intensity to control reaction kinetics and reversibility in photomechanical crystals. Chem. Sci. 2020, 11, 9852–9862.

5 Bragg, Henry W.; Bragg, Lawrence W., X RAYS AND CRYSTAL STRUCTURE, January 1915, G. Bell and sons L.T.D. London (ed.).

6 Stroll S. Goldfarb D., EPR Spectroscopy: Fundamentals and Methods, April 2018, John Wiley & Sons.

7 Kevan L. and Bowman M. K. Modern Pulsed and Continuous Wave Electron Spin Resonance New York, Year: 1990, Publisher, John Wiley & Sons.

8 Carrington A, McLachlan AD. Introduction to Magnetic Resonance: with Applications to Chemistry and Chemical Physics. 1979, Chapman and Hall.

9 Rinck P. A., Magnetic Resonance in Medicine, 12th edition, 2018 BoD.

10 Wertz, J., Bolton, J. R., Electron Spin Resonance: Elementary Theory and Practical Applications, 1986, Springer.

11 Coey, J. M. D. Magnetism and Magnetic Materials. March 2010, Cambridge University Press.

12 Stroll S., Schweiger A., EasySpin, a comprehensive software package for spectral simulation and analysis in EPR, The Journal of Magnetic Resonance, 2006, Volume 178, Issue 1 pg 42-55.

13 Schweiger A., Jeschke G., Principles of Pulse Electron Paramagnetic Resonance, 2001 Oxford University Press - Oxford.

14 Dikanov S. A., and Tsvetkov Y. D., Electron Spin Echo Envelope Modulation (ESEEM) Spectroscopy), 1992, CRC Press, Inc. – USA.

15 Mims W. B., Amplitudes of superhyperfine frequencies in electron-spin-echo-envelope. Phys Rev B 1973, 6: 3543-3545.

16 Kevan L., Schwartx R. N., Time Domain Electron Spin Resonance, 1979, John Wiley & Sons - New York.

17 García-Rubio I., Pulsed ENDOR and ESEEM: Principles and Examples of Applications to Heme Proteins. In: Encyclopedia of Biophysics. 2013, Springer, Berlin, Heidelberg.

18 Balamurugan M., Karunakaran C., Spin Resonance Spectroscopy, 2018, Elsevier.

19 Delaney, P; Greer, JC (Feb 2010). "Spin-Polarization Mechanisms of the Nitrogen-Vacancy Center in Diamond" Nano Letters. 10 (2): 610–614.

20 Gordon, Luke; Weber, Justin R.; Varley, Joel B.; Janotti, Anderson; Awschalom, David D.; Van de Walle, Chris G. (2013-10-01). "Quantum computing with defects". MRS Bulletin. 38 (10): 802–807.

21 Rogers, L. J.; Doherty, M. W.; Barson, M. S. J.; Onoda, S.; Ohshima, T.; Manson, N. B. (2015-01-01). "Singlet levels of the NV − centre in diamond". New Journal of Physics. 17 (1): 013048.

22 Rogers, L. J.; Armstrong, S.; Sellars, M. J.; Manson, N. B. "Infrared emission of the NV centre in diamond: Zeeman and uniaxial stress studies". New Journal of Physics. 2008. 10 (10): 103024.

23 Doherty, Marcus W.; Manson, Neil B.; Delaney, Paul; Jelezko, Fedor; Wrachtrup, Jörg; Hollenberg, Lloyd C.L. "The nitrogen-vacancy colour centre in diamond". Physics Reports. 2013. 528 (1): 1–45.

24 Kinsey, J. L., Laser-Induced Fluorescence, Ann. Rev. Phys. Chem. 1977 28: 349-72.

25 Mirabella F. M., Modern Techniques in Applied Molecular Spectroscopy, Techniques in Analytical Chemistry Series. 1998, John Wiley & Sons, Inc.

26 Zin, J. H., Clarke P.J., Total Color Management in Textiles, 2006, Woodhead Publishing.

27 Carter, C. Barry; Norton, M. Grant., Ceramic Materials: Science and Engineering. 2007, Springer Science & Business Media.

28 Chapyshev, S. V. Korchagin D. V., Costa P., Sander, W., Photochemical generation of high-spin nitrenes from 4,6-diazido-N-(4,6-diazido-1,3,5-triazin-2-yl)-1,3,5-triazin-2-amine in solid argon Journal of Photochemistry and Photobiology A: Chemistry. Volume 377, 15 May 2019, Pages 207-213

29 Smirnov V.A., Brichkin S.B., Spectral and Photochemical Properties of Aromatic Nitrenes; Chemical Physics Letters Volume 87, Issue 6, 16 April 1982, Pages 548-551.

30 Traficante, D.D., Relaxation. Can T_2, be longer than T_1?. Concepts Magn. Reson., 1991 3: 171-177.

Chapter 3 Reversible Adhesion Switching Using Spiropyran Photoisomerization in a High Glass Transition Temperature Polymer

3.1 Introduction

Materials that change their properties in response to external stimuli (light, heat, pH, etc.) can be used to make structures that adapt to their surroundings. For example, the assembly or disassembly of objects or thin films "on command" could be useful for some applications. In the case of drug delivery, it is desirable to have a container that can disintegrate when required. For active transport, one would like to attach an object to a carrier, move it, and then detach it in a different location. For surface protection, it is important to be able to apply a protective coating that can be easily removed. In all these examples, the ability to turn off the adhesion between two objects using an external stimulus would be an enabling technology. The use of light as a stimulus is in many ways ideal because it does not require physical contact or exposure to additional chemical species. Light also provides many parameters (intensity wavelength, polarization) that can be varied to selectively control adhesion changes.

Light-controlled adhesives can be based on a variety of physico-chemical changes.[1] Photocrosslinking that creates covalent bonds between surfaces is an approach that leads to irreversible bonding.[2, 3] Mechanical bonding between surfaces can be modulated by a photoisomerization reaction that induces a large change in mechanical strength or tackiness.[4, 5] In extreme cases, photoinduced melting can occur, leading to very large changes in the material's ability to adhere.[6-13] Rather than relying on large changes in chemical bonding or mechanical properties, adhesion can also be reversibly modulated

using purely noncovalent interactions, for example by using photoisomerization to switch the electrostatic properties of a molecule bound to a surface.[14-20] Instead of using surface-bound molecules that switch polarity after photoisomerization, it is also possible to simply embed the photochromic molecules into a polymer host.[21, 22] This approach has the advantage of simplicity, since it does require surface chemistry and the polymer host has well-defined properties. It also has the advantage of clean separation without leaving residual bound molecules behind.

In order to modulate solid-solid adhesion, our idea is to switch the effective polarity of a polymer layer, and thus its Coulombic interaction with the surface, by utilizing the photoisomerization of a photochromic dopant. In previous work, we found that spiropyran (SP) isomerization in polystyrene could enhance its adhesion to a clean glass surface by 5×, but that this change was mostly irreversible due to internal mechanical changes in the polymer.[22] In order to demonstrate decreased adhesion, we used a different donor-acceptor Stenhouse adduct (DASA) photochrome that started in a relatively polar form. Visible light exposure could reduce adhesion by a factor of 2, but at the high dye concentrations used, the switching required up to 12 hours of light exposure.[23] Based on these results, we identified some important material requirements for developing a more practical polymer-glass system with reasonably rapid adhesion switching. First, given that the substrate, Piranha-cleaned glass, is highly polar and hydrophilic, the reversible photochromic reaction should generate a large polarity change. Second, the host polymer should be highly nonpolar so that its background contribution to the adhesive forces is minimized. Third, the host polymer should be resistant to nanoscale mechanical changes, so that only

the polarity change affects the glass-polymer interface. If we assume that the nanoscale morphology changes result from local heating by the photochrome, then this means that the host polymer should have a high glass transition temperature (T_g).

In this chapter, we demonstrate that a polymer-photochrome composite based on spiropyran in a Zeonex (ZX) host is capable of fulfilling all the above requirements. The spiropyran (SP)→merocyanine (MC) photoisomerization provides a highly reversible reaction with a large polarity change[24, 25], while replacing PS (T_g = 90-100°C) with the cyclic olefin polymer Zeonex (ZX) (T_g > 120°C)[26] results in a highly nonpolar solid that should be more resistant to nanoscale mechanical deformations. Ultraviolet (UV) light-induced isomerization of SP to the polar MC form increases adhesion to a clean glass surface by a factor of 5, and this MC form is stable for hours in the ZX matrix. Visible irradiation switches it back to the nonpolar SP form and close to its original weak adhesion. This high degree of reversibility was not observed for polystyrene films, and it allows us to harness the MC→SP reaction to make a light-controlled payload release device as well as accelerate the polymer film delamination rate in water by a factor of 100. The kinetics of the water delamination, as well as the origin of some residual adhesion after switching back to the SP form are investigated. Although the noncovalent intermolecular interactions used here have limited adhesive strength, they provide a clear example of how photochemistry can be used to control adhesion and stimulate a structural response in a macroscopic object.

3.2 Experimental

3.2.1 Materials and Sample Preparation: 1′,3′-dihydro-1′,3′,3′-trimethyl-6-nitrospiro[2H-1-benzopyran-2,2′-(2H)-indole]) (SP), was obtained from TCI. Zeonex Z480 (ZX) was obtained from Zeon Specialty Materials. Hydrogen peroxide (30%) concentrated sulfuric acid (95.0−98.0%), and toluene were obtained from Fisher Scientific. All chemicals were used as received. Glass microscope slides (Fisherbrand 25 x 75 x 1 mm) were cleaned using freshly prepared acidic piranha solution of a 1:3 ratio of 30% hydrogen peroxide and concentrated sulfuric acid. The solution was boiled, and the glass slides were submerged for 20 minutes. After removal from the piranha solution, the glass slides were thoroughly rinsed with Mili-Q (10 MΩ) water, dried with compressed air and used immediately. ZX-SP mixtures for film casting were made by first preparing a 17.5 mg/ml Zeonex solution in toluene. Spiropyran was then added to the solution to attain the desired mass fractions of 0%, 6%, 11%, 20%, 30% or 40%. Inspection of SP/ZX films by optical and atomic force microscopy methods showed homogeneous, smooth films with no sign of SP aggregates or scattering due to particles (Supporting Information, Figures S3.14).

3.2.2 Characterization: Water detachment tests were performed by dropping 2.5 μL of a ZX-SP toluene solution onto a piranha-cleaned slide. Six circular films, three ZX only and three ZX-SP, were placed on the slide. UV exposed samples were placed under a 365 nm bench lamp (UVP 15 W) with an intensity at the sample of 0.6 mW/cm^2 for 1 min. The microscope slides were then submerged in a water bath with stirring (1 inch stir bar at 900

rpm), and the number of detached dots was tracked over time. Samples were irradiated with a 532 nm laser through a diffuser 6 inches above the sample.

Pull-off adhesion tests were performed by cutting a glass microscope slide into 6 mm wide strips before piranha cleaning. 3.5 μL of ZX-SP solution was added the top of a cleaned slide in two locations and the other pieces of cleaned glass were pressed on top. The entire structure was allowed to dry overnight. UV exposed samples were placed under a 365 nm bench lamp (UVP 15 W) with an intensity at the sample of 0.6 mW/cm^2 for 1 min. Weights were added to the center of the sample in 5 g increments every 10 seconds until the sample broke.

Shear adhesion tests were performed using two piranha-cleaned glass slides. 10 μL of ZX-SP solution was added to the top of one slide and another cleaned slide was pressed on top. The sample was allowed to dry overnight. UV exposed samples were placed under a 365 nm bench lamp (UVP 15 W) with an intensity at the sample of 0.6 mW/cm^2 for 1 min. For visible light exposure, samples were irradiated with a 532 nm laser through a diffuser placed six inches away from the sample. Typically, the samples were irradiated by the 532 nm light for 30 minutes with an intensity of 30 mW/cm^2. The shear strength was measured using an Instron 5942 (Single Column Tabletop Testing System) with a 100 N load cell. Samples were pulled at a speed of 3 mm/min and each concentration was tested five times.

Contact angle measurements were taken using a Kruss DO4010 Easy Drop. Samples were prepared on cleaned glass slides using 5 μL of ZX-SP solution and allowed to dry overnight. UV exposed samples were placed under a 365 nm bench lamp (UVP 15

W) with an intensity at the sample of 0.6 mW/cm^2 for 1 min. Samples were irradiated with 532 nm laser through a diffuser 6 inches above the sample. 5 μL of deionized water was placed on the surface and the software was used to measure the contact angle.

Fluorescence data were obtained by a Horiba PTI QM-400 Fluorescence spectrophotometer. Samples were prepared using 10 μL of ZX-SP solution and allowed to dry on glass slides overnight. The sample were loaded into the solid sample holder and set to an angle of 30°. Samples were excited with 570 nm light. Absorbance measurements were taken using a Cary 60 UV/Vis spectrophotometer. Glass slides were cut to cuvette width and 10 μL of ZX-SP solution were placed on the slide at the height of the beam (20 mm) and allowed to dry overnight on a level surface.

Payload release test samples were prepared in the same manner as the shear tests. Two cleaned slides were adhered by a layer of SP/ZX. After drying and UV exposure, a 130 g weight was attached to one of the slides and the assembly was then mounted vertically. Irradiation with a 532 nm laser began 30 minutes after the sample was mounted. A diffuser was placed six inches from the sample. The time it took the sample to drop after irradiation began was recorded.

Polymer surface characterization was performed using a Veeco systems Dektak 8 and a Dimension 5000 AFM. Differential scanning calorimetry (DSC) measurements were taken on a Netzsch 214 Polyma differential scanning calorimeter. Samples were started at 70°C and heated to 170°C at a rate of 20°C/min. Samples were cooled at 20°C and the process was repeated three times (Supporting Information, Figure S3.15).

3.3 Results and Discussion

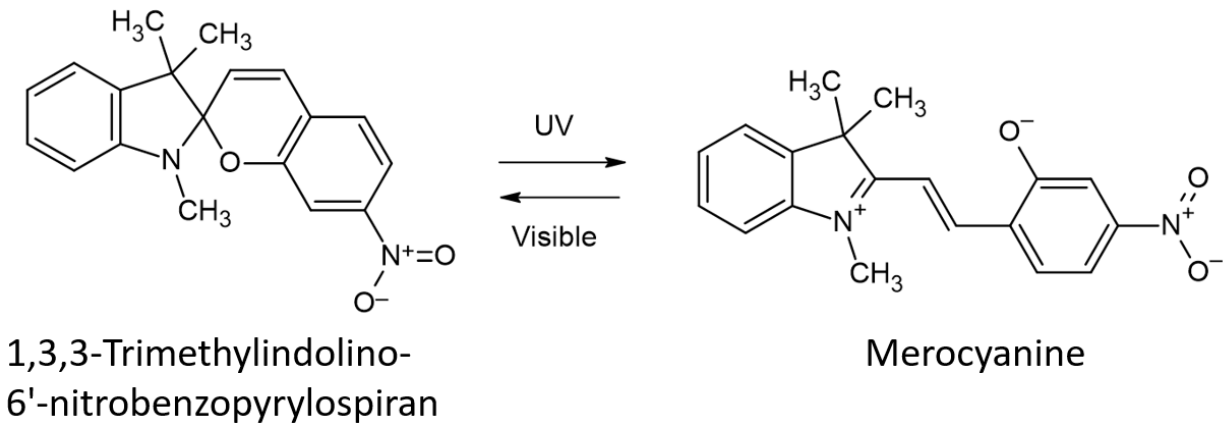

Figure 3.1: Spiropyran (SP) converts to polar Merocyanine (MC) form when exposed to UV light, and reverts after exposure to visible light.

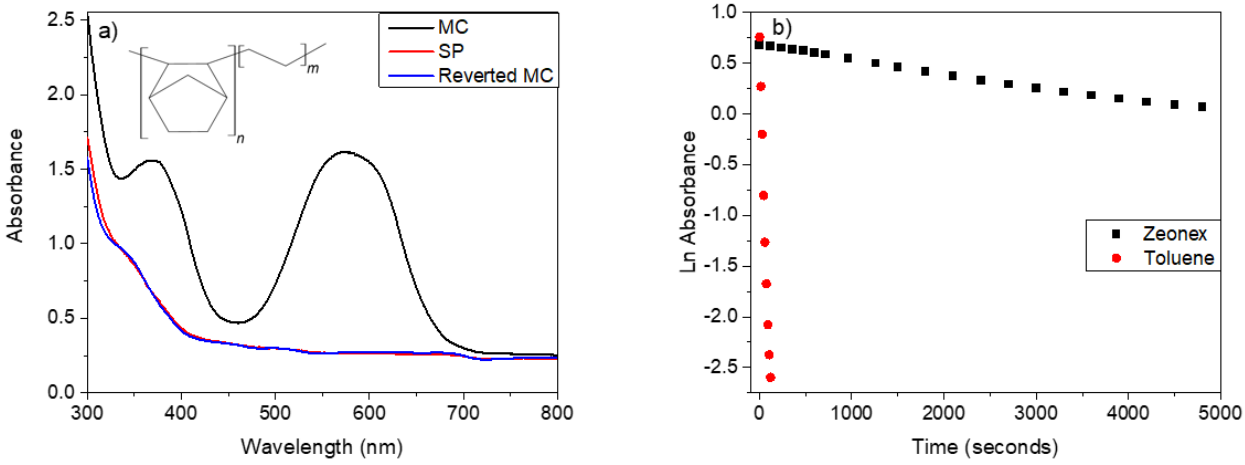

Figure 3.2: **a)** Absorption spectra of a 30% w/w SP/ZX film before light exposure showing only the SP absorption (red), showing the MC absorption after UV exposure (black), and MC reverted back to SP after visible light exposure. **b)** Absorbance decays at 600 nm of the MC isomer in toluene (red circles) and in ZX (black squares). A long-time scale plot of the decays is available in the Supporting Information

The structure of the ZX polymer is shown in Figure 3.2a. We characterized our ZX sample using differential scanning calorimetry, finding a relatively high T_g=140.4°C. The absorption spectrum showed no features below 220 nm, consistent with the absence of

aromatic impurities. But using toluene as a common solvent, SP could be dissolved into ZX at variable loadings. The photoisomerization of SP to its MC form in ZX is accomplished by exposure to UV light, while MC can then be switched back to SP by irradiation with visible light (Figure 3.1). The switching of isomers can be easily followed by the growth and disappearance of the MC absorption, peaked at 580 nm in ZX (Figure 3.2a). The stability of the MC form is sensitive to the polarity of its host environment[27, 28], and in a nonpolar liquid like toluene it has the relatively short lifetime of 34 s, as shown in Figure 3.2b. But when the host is a rigid polymer like ZX, the lifetime of the MC form was extended by more than two orders of magnitude to 4500 s. The very slow rate of MC→SP thermal isomerization in nonpolar ZX but is consistent with previous work showing the rate of MC isomerization back to SP is on the order of minutes in other solid polymers.[29, 30] Additional studies would be needed to shed light on the precise mechanism of the slow MC→SP reaction in ZX, but it is likely that the rigid polymer matrix provides steric hindrance for this back reaction. The survival of the MC photoisomer for >1 hr allowed the MC/ZX film adhesion to be characterized using standard methods.

Adhesion is measured by the force/area that must be applied both parallel (shear) and perpendicular (pull-off) to the interface to rupture the polymer-glass bond. Incorporation of SP into ZX increased its adhesion to the glass even in the absence of light, and this adhesion increased slightly with increasing SP loading. Two glass slides could be adhered together with a polymer layer measured to be in the range 50-70 nm by atomic force microscopy (Supporting Information, Figure S3.14). The creation of the highly polar MC isomer in the ZX polymer should increase its attraction to the glass surface and thus

the adhesive force. Indeed, we observe that photoisomerization leads to a 4-5× increase in adhesive strength for the highest (30% w/w) SP concentrations, comparable to that observed previously for SP/polystyrene blends.[22] The results for shear and pull-off adhesion tests as a function of SP concentration before and after UV irradiation are shown in Figures 3.3a and 3.3b.

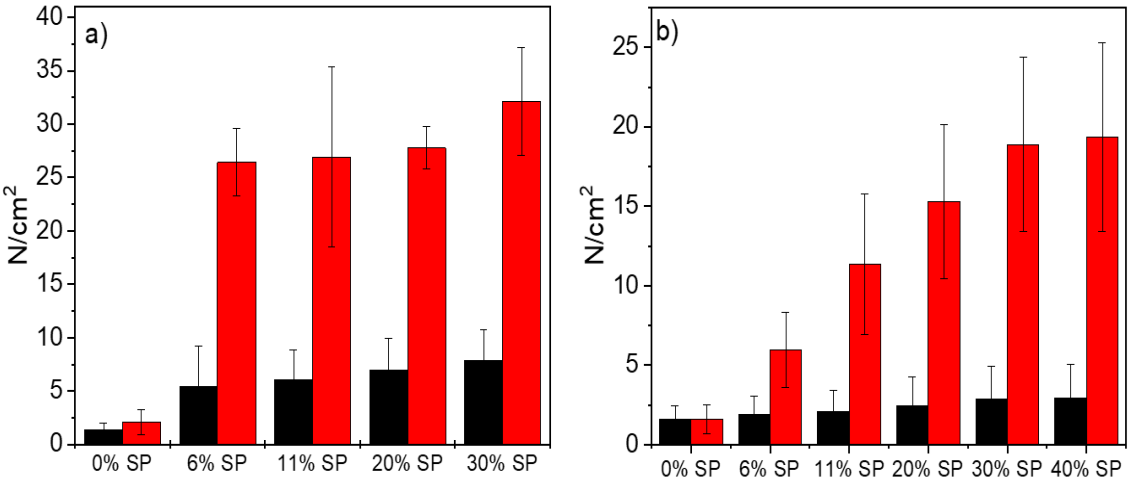

Figure 3.3: a) The increase in pull-off adhesive strength with increasing SP concentration before (black) and after (red) UV light exposure. **b)** The increase shear adhesive strength with increasing SP concentration before (black) and after (red) UV light exposure. For the pull-off adhesion, no significant change in adhesion was observed after 6% SP/ZX, and for shear adhesion no change was observed after 30% SP/ZX.

	Contact Angle (deg)	Shear Strength (N/cm^2)
ZX Only	91.5 ± 4.7	1.6 ± 0.8
30% w/w SP/ZX	84.8 ± 4.0	2.9 ± 2.1
30% w/w SP/ZX after UV Exposure	67.9 ± 3.7	18.9 ± 5.5
30% w/w SP/ZX after UV and visible exposure	81.7 ± 1.7	4.8 ± 2.2

Table 3:1 The change in contact angle on 30% w/w SP/ZX samples before and after exposure to UV light as well as the angles after back reaction with a 532 nm laser. The bottom of the table shows the shear strength change when exposed to UV light and after being back reacted with a 532 nm laser.

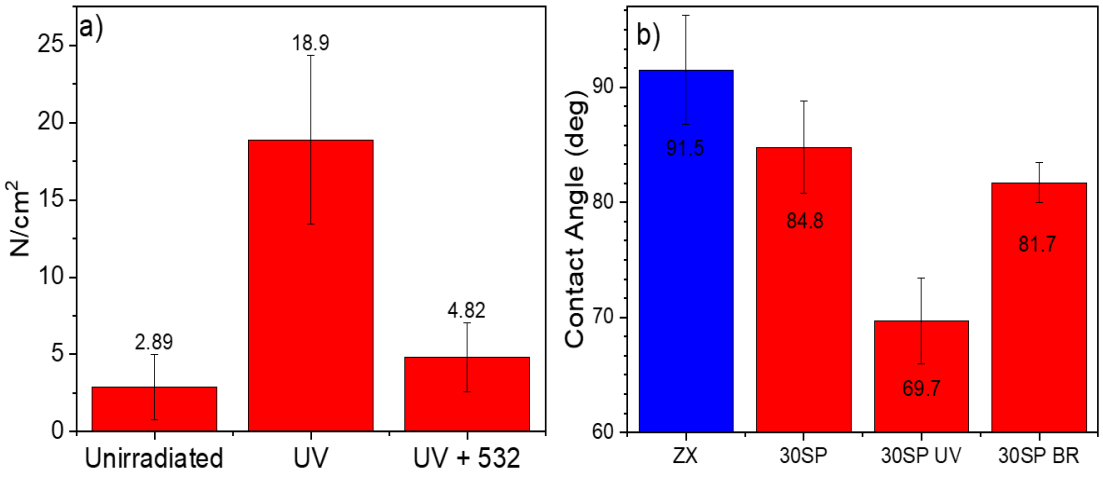

Figure 3.4 a) The increase in shear adhesion strength when a 30% w/w SP/ZX mixture was exposed to UV light, followed by a decrease in adhesive strength when exposed to UV for 1 minute followed by a 532 nm laser for 30 minutes. **b)** Contact angle measurements show a decrease in contact angle when ZX/SP samples are reacted with UV light. The contact angle mostly recovers when exposed to 532 nm light.

The important difference for the ZX blend is that the adhesion increase could be almost completely reversed using visible (532 nm) light. This reversal is shown in Figure 3.4a, where the shear adhesion for a 30% SP/ZX film jumps from 3±2 N/cm^2 to 20±5 N/cm^2 after UV exposure, and then drops back down to 5±2 N/cm^2 after visible light exposure. MC/polystyrene films did not exhibit this large reversal of adhesion after switching back to the SP form, which we attributed to the softer PS deforming on the nanoscopic scale to create irreversible mechanical adhesion points to the glass surface.[22] The reversible adhesion was accompanied by changes in contact angle for water on the SP/ZX film surface. Contact angle measurements in Figure 3.4b show that SP slightly lowers the contact angle of ZX from 91.5° to 84.8°, photoisomerization under UV light lowers it to 69.7°. After visible light exposure, the contact angle rebounds to 82°, indicating that the nonpolar interface is almost fully recovered. These contact angle changes are larger than previously measured values for SP in polymer hosts[22, 31] and similar to those observed for SP-functionalized surfaces[32], suggesting that the SP molecules embedded in the film are exposed to the surface. The adhesion and contact angle values are summarized in Table 1. Cycling the ZX/SP film on glass through 3 UV-Vis exposures did not change its adhesive properties, but it should be noted that once the film was detached from the glass surface, it could not be reattached.

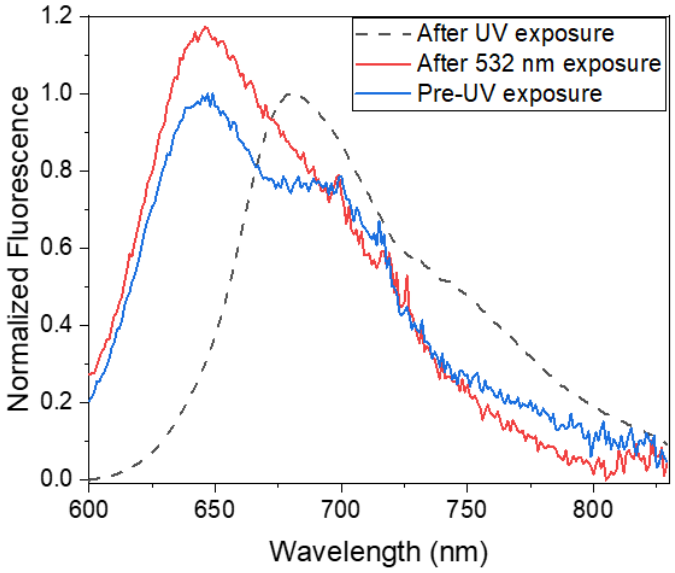

Figure 3.5 The normalized MC fluorescence peaks (excited at 532 nm) for a ZX/SP film before light exposure (blue), after UV exposure (black dashed), and after the same film is exposed to a 532 nm laser for 60 min with an intensity of 300 mW/cm^2 (red line). The MC peak of the UV exposed sample is about 50× larger in the raw data. The blue-shifted MC fluorescence is indicative of a polar environment.

The correlated changes in adhesion and contact angle strongly suggest that the polar MC isomer plays a role. No MC absorbance can be detected before UV irradiation, possibly because its concentration was so low that its absorbance was below the 0.01 absorbance sensitivity of the instrument. But by using more sensitive fluorescence detection with 532 nm laser excitation, we were able to observe some MC fluorescence in the unirradiated SP/ZX films, as shown in Figure 3.5. In the SP/ZX film, this fluorescence spectrum was blue-shifted by 40 nm with respect to the neutral MC isomer, whose emission dominated after UV exposure. The blue-shifted fluorescence is characteristic of the zwitterionic form of the MC isomer, which forms in more polar environments[27, 33, 34] or as a result of protonation.[35] The glass surface can generate both situations due to the presence of highly polar silanol groups which can also act as acids. The observed fluorescence blue-shift is

not as large as that observed for protonated MC[35], so we attribute it to MC isomers, formed either via thermal or photo-induced SP isomerization at the glass-polymer interface.

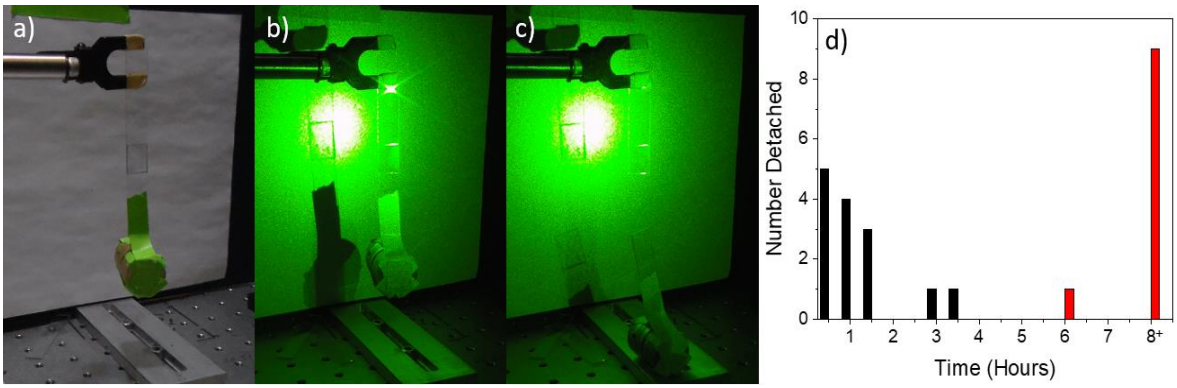

Figure 3.6: **a)** The initial payload release setup with weight attached to glass by a 30% SP/ZX film that has been exposed to UV light, leaving a purple tinged square in the middle. **b)** The same setup immediately after turning the laser on. **c)** The broken sample with detached weight after approximately 1 hr of laser exposure. **d)** A histogram showing the 532 nm irradiation times required to drop the weight (black) and a histogram of times required for the sample to drop without irradiation (red). The unirradiated samples that did not drop after 8 hours are placed in the 8+ bin.

Zwitterionic MC, formed either by protonation or by polar environments, is resistant to photoisomerization back to the SP form. [27, 36, 37] After the MC/ZX films were converted back to SP/ZX films, i.e. after a full cycle of UV/Visible exposure, the blue-shifted MC fluorescence signal increased by about 20%, suggesting that light cycling generated excess residual zwitterionic MC. This residual MC signal was less than 1% of the peak MC signal at 670 nm after 365 nm irradiation but persisted even in films that were exposed to the 532 nm laser light for 1 hour or longer. The excess zwitterionic MC would help explain the fact that the original weak adhesion was not fully recovered after visible light irradiation. Even though the increase is relatively small (20%) relative to the adhesion increase (~100%), they could have a large effect on the adhesion if these highly polar molecules are localized near the glass surface. But we cannot rule out that the ZX also undergoes local

morphology changes that enhance the mechanical adhesion, albeit to a much smaller degree than PS.

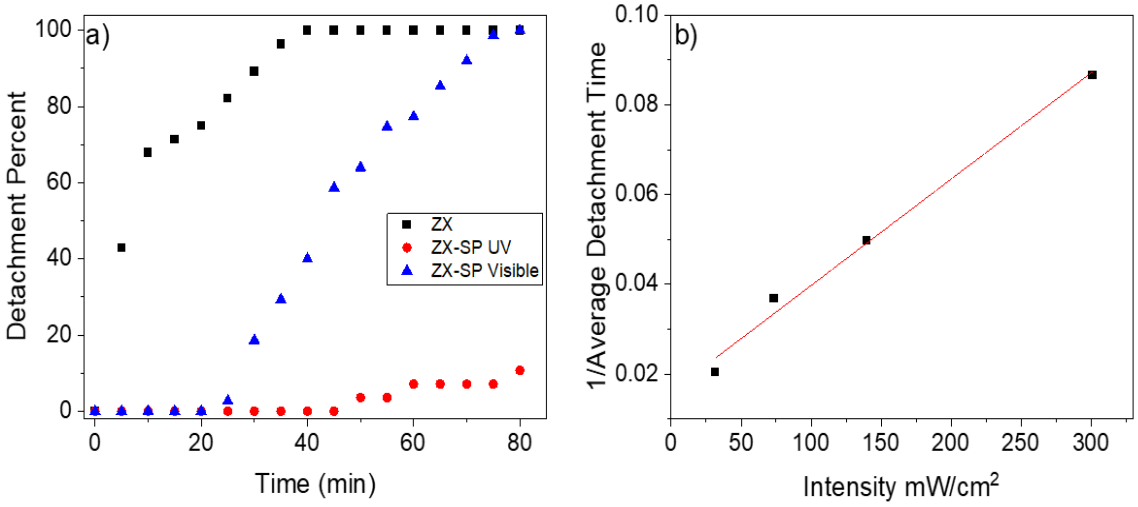

Figure 3.7 a) The detachment of thin films in stirred water as a function of time. Neat ZX films (black) detach quickly, while the 11% w/w SP/ZX films detach much more slowly after UV exposure (red). When the SP/ZX films are exposed to the 532 nm laser with an intensity of 30 mW/cm^2, the detachment speeds up (blue). **b)** The mean detachment rate appears to have a linear dependence on the 532 nm laser intensity.

The identification of a robust photoswitchable adhesion allows us to explore possible applications. We first tested whether the ability to turn off adhesion using visible light persists when the adhering layer is under a constant load. A 130 g weight was attached to a glass slide that had been "glued" to a second glass slide by a 30% MC/ZX film that had been exposed to UV light. In the absence of visible light, the weight typically remained stably suspended for more than 8 hours. But when the sample was exposed to visible light at 300 mW/cm^2, the surfaces broke apart and the weight dropped after 1-2 hours. This sequence of events is illustrated in Figures 3.6a-c. The accelerated detachment under visible light was a robust result, as shown by the histogram of drop times in Figure 3.6d. Note that for all tests, the polymer never showed any signs of melting or softening, and the

temperature rise of the sample was limited to <3°C, as measured by an infrared sensing thermometer.

The effect of visible light was even more pronounced on the delamination rate of polymer films in stirred water. In our previous work, water delamination was measured after multiple hours of visible irradiation, followed by placement of the films in water.[22, 23] The large adhesion changes of the ZX films made it practical to monitor the film detachment time (τ_{detach}) in real time during illumination. We compared the detachment of neat ZX films, MC/ZX films after UV exposure, and MC/ZX films after UV exposure that were then continuously irradiated with 532 nm light. As expected, the neat ZX films rapidly detached, since the polar-nonpolar interaction is relatively weak. From the data in Figure 3.7a, the average time to detach for a ZX film was 10 min. The addition of SP had little effect on τ_{detach}, increasing it by about 20%. But when the SP was converted to the MC isomer by UV light exposure for a period of 1 min, the average delamination time increased to 1000 min. When these MC/ZX films were subsequently exposed to 532 nm light with an intensity of 30 mW/cm^2, the average delamination time decreased to 40 min. Increasing the visible light intensity accelerated the delamination, and the average delamination time approached that of neat ZX at 300 mW/cm^2. Figure 3.7b shows the average detachment rate, defined as $1/\langle\tau_{detach}\rangle$, as a function of 532 nm light intensity. The linear relationship between detachment rate and light intensity is consistent with this rate being controlled by the rate of MC→SP photoisomerization.

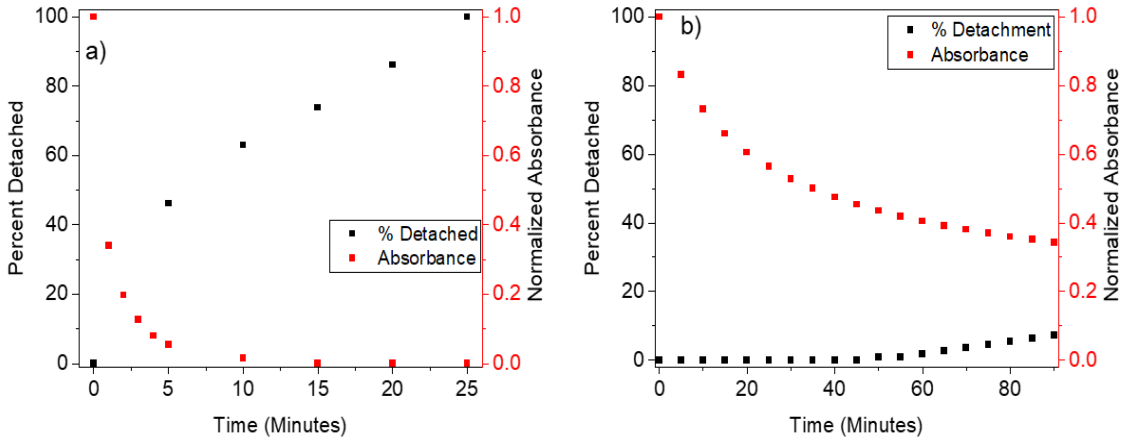

Figure 3.8: a) The MC absorbance (red) decreases faster than ZX/SP dots detach in water during exposure to 532 nm laser light at 300mW/cm^2. **b)** The MC absorbance decreases faster than the polymer film detachment even with no light exposure. Both film samples were 11% w/w SP/ZX.

Although the MC→SP reaction rate clearly influences the delamination rate, they are not identical. For example, in Figure 3.7a, there is a significant lag between the start of the irradiation (photoisomerization) and the onset of film detachment. This can be seen more clearly in Figure 3.8, which plots both the decrease of the MC absorbance and the fraction of detached film spots (f_{detach}) for 532 nm illumination at the relatively high intensity of 300 mW/cm^2. Even though the MC absorbance almost completely vanishes by 10 min, only about 60% of the films have detached by this point. At the other extreme, if no visible light is present, the MC absorbance decreases slowly due to thermal isomerization back to the SP form, as shown in Figure 3.8b, and the detachment of the films lags even farther behind. We think this feature of the delamination process results from diffusion of water along the polymer-glass interface that follows the MC→SP photoisomerization.[22, 38, 39] This diffusion is usually slower than the photoisomerization but is required in order to rupture the weak glass-polymer adhesive bond. If H_2O diffusion

across the polymer-glass interface is required for delamination, then the average time should scale as the distance squared, i.e. $\langle \tau_{\text{detach}} \rangle \propto d_{film}^2$, where d_{film} is the diameter of the polymer film. To test this hypothesis, we measured the visible light induced delamination for two different sets of MC/ZX polymer films, one with an average diameter of 6.2 mm and one with a diameter of 7.8 mm. The $<\tau_{detach}>$ values for the different diameters were 12.5 min and 27.5 min, respectively during 532 nm exposure. The diameter ratio of 7.8/6.2 then predicts a $<\tau_{detach}$(7.8 mm)>/$<\tau_{detach}$ (6.2 mm)> ratio of $(7.8/6.2)^2$=1.6, which is somewhat less than the experimental value of 2.2±0.2. But the fact that the film area affects the detachment time suggests that water diffusion plays some role. A full understanding of the delamination process will probably require a model that takes into account how the MC→SP reaction facilitates water penetration across the interface.

Finally, we return to the mechanism of the reversible adhesion. We attribute the high reversibility of the SP/ZX blends to the resistance of ZX to nanoscale deformations driven by local heating after photon absorption. This resistance is determined by its relatively high T_g value. SP photoisomerization can cause a host polymer to undergo photomechanical distortions[40, 41], and we first assumed that a higher bulk elastic modulus of the polymer host would be a good predictor of its resistance to nanoscale deformations that influence adhesion. But polystyrene actually has a higher elastic modulus (2-8 GPa)[22, 42] than Zeonex (1.5-2.5 GPa)[43, 44] and should be more resistant to nanomechanical deformation at room temperature. We found that another high elastic modulus polymer, polymethylmethacrylate (T_g~110°C)[26], also showed poor reversibility when doped with SP. A second requirement is that the polymer host be very nonpolar, so it does not have

intrinsically strong adhesion that overwhelms the SP→MC switching effect. The combination of high T_g and nonpolarity is satisfied by ZX, but other polymers with these two attributes could also support this effect. A different approach would be to dispense with the polymer host entirely, and the development of SP derivatives that efficiently switch in solid form[45, 46] provides another potential route to photoswitchable adhesion.

3.4 Conclusion

This work demonstrates that combining a high-T_g nonpolar polymer host (ZX) with a photochromic molecular dopant (SP) that undergoes a large polarity change can create a light switchable polymer-glass adhesive bond. The adhesion switching relies on modulating the noncovalent forces between two solid surfaces, as opposed to changes in mechanical adhesion induced by melting or softening. Both shear and pull-off adhesive strengths can be increased or decreased by a factor of 5 by switching between the SP and MC isomers, while the delamination time can be accelerated by a factor of 100 when a MC/ZX film is exposed to green light. Interestingly, the adhesion appears to be influenced by the presence of zwitterionic MC isomers even in unirradiated films. One possible route to larger adhesion changes would be to utilize a photochromic molecule that can be converted to its polar form only by light, as opposed to the thermal isomerization pathway that is available for SP.

Although the strength of adhesion based on noncovalent forces will always be weaker than that based on covalent cross-linking or mechanical interlocks, it has the advantages of simplicity and reversibility that may lead to applications in areas where ultra-strong bonding is not required. The light-controlled release of a suspended payload,

demonstrated in Figure 3.6, is one example, but this technology could also be used as a solvent-free method to remove protective coatings or to disassemble structures by using light to deactivate a polymer "glue".

3.5 Supporting Information

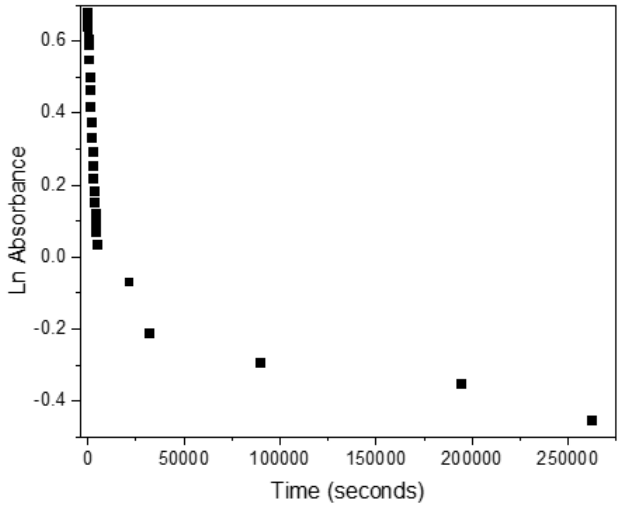

Figure S3.9: The long-time scale reversion of MC to SP in ZX.

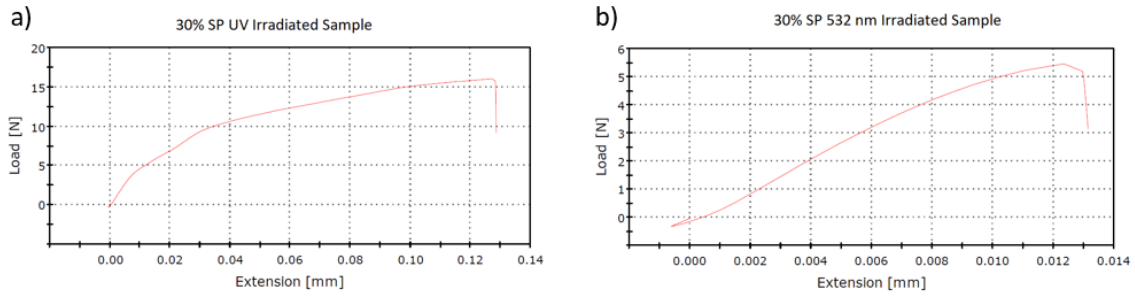

Figure S3.10 Example shear force curves obtained for a 30% w/w SP/ZX film on the Instron 5942, **a)** after UV exposure, and **b)** after UV and Visible light exposure. The sudden drop at the largest extension represents the break point where the adhesion (Force/Area) is measured.

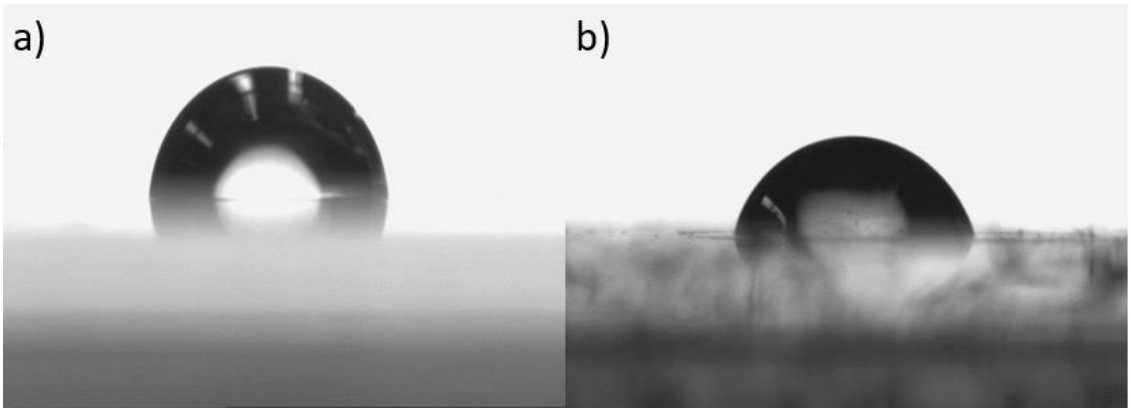

Figure S3.11: Photos of the contact angle measurements of **a)** neat ZX showing a contact angle of 88°; **b)** 30% w/w SP/ZX post UV irradiation showing a contact angle of 71°.

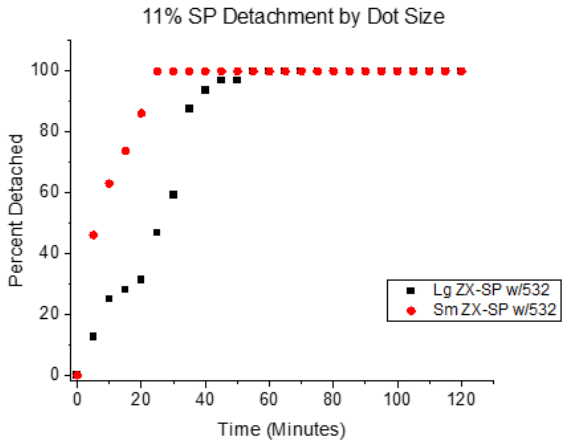

Figure S3.12: Size dependence of polymer film detachment. The small diameter (6.2 mm, red circles) and large diameter (7.8 mm, black squares) 11% w/w SP/ZX films were exposed to identical 532 nm laser intensities after UV conversion to the high adhesion state. The larger diameter films detached more slowly.

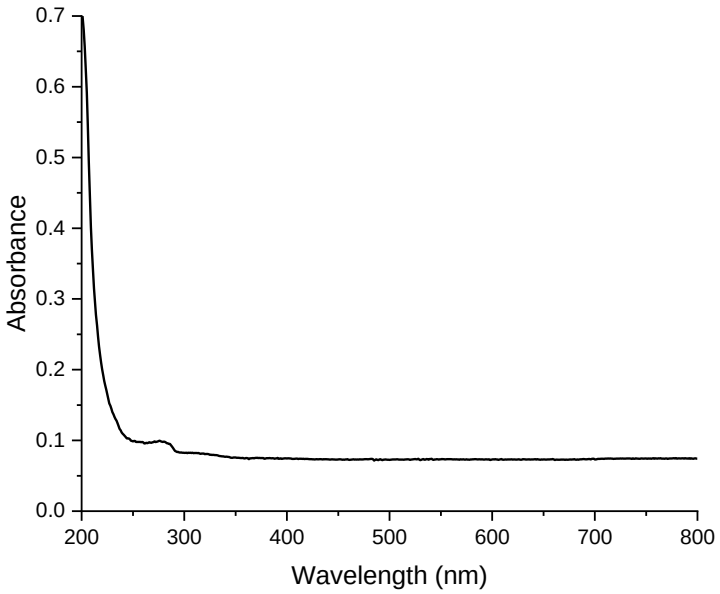

Figure S3.13: The absorbance of a ZX film.

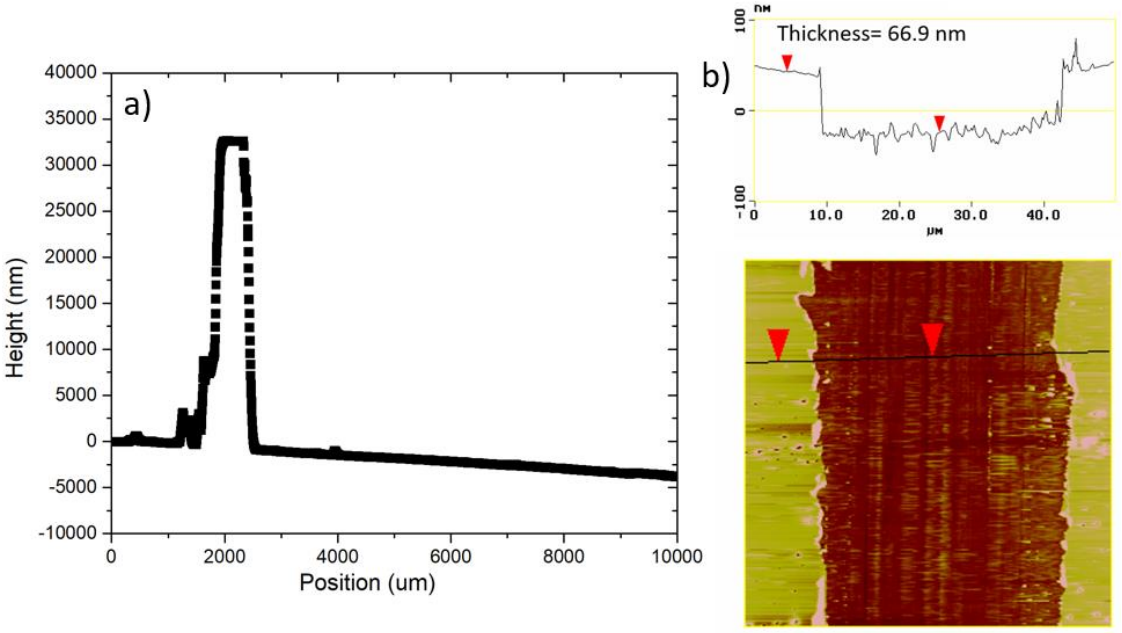

Figure S3.14: a) The Dektak profilometry of the polymer surface on the glass following the break. **b)** The AFM measurement of the same sample. The AFM showed the average thickness of this film on this sample was 66.9 nm.

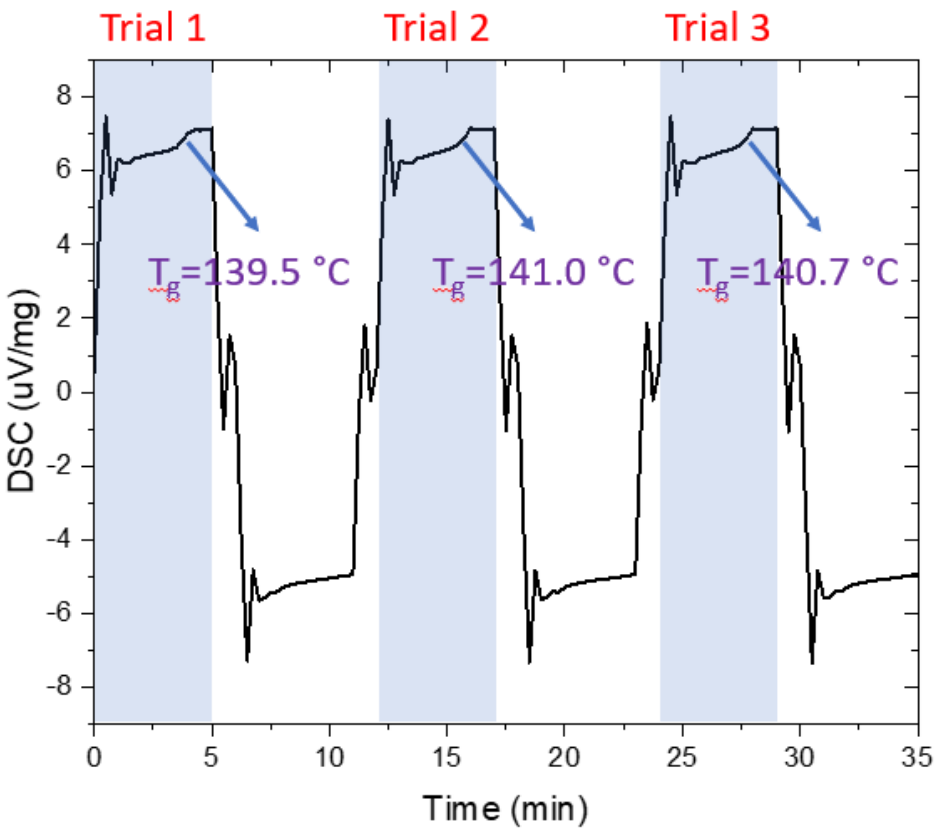

Figure S3.15: DSC results showing the glass transition temperature for Zeonex Z480. The average Tg measurement was 140.4 °C.

3.6 References

1. Hohl, D. K.; Weder, C., (De)bonding on Demand with Optically Switchable Adhesives. *Adv. Opt. Mater.* 2019, *7*, 1900230.

2. M.Yan; Harnish, B., A Simple Method for the Attachment of Polymer Films on Solid Substrates. *Adv. Mater.* 2003, *15*, 244-248.

3. Vitale, A.; Trusiano, G.; Bongiovanni, R., UV-Curing of Adhesives: a Critical Review. *Rev. Adhesion Adhesives* 2017, *5*, 105-161.

4. Gurney, R. S.; Dupin, D.; Nunes, J. S.; Ouzineb, K.; Siband, E.; Asua, J. M.; Armes, S. P.; Keddie, J. L., Switching Off the Tackiness of a Nanocomposite Adhesive in 30 s via Infrared Sintering. *ACS Appl. Mater. Interfaces* 2012, *4*, 5442-5452.

5. Gao, Y.; Wu, K.; Suo, Z., Photodetachable Adhesion. *Adv. Mater.* 2019, *31*, 1806948/1-7.

6. Saito, S.; Nobusue, S.; Tsuzaka, E.; Yuan, C.; Mori, C.; Hara, M.; Seki, T.; Camacho, C.; Irle, S.; Yamaguchi, S., Light-Melt Adhesive Based on Dynamic Carbon Frameworks in a Columnar Liquid-Crystal Phase. *Nat. Comm.* 2016, *7*, 12094/1-7.

7. Norikane, Y.; Uchida, E.; Tanaka, S.; Fujiwara, K.; Nagai, H.; Akiyama, H., Photoinduced Phase Transitions in Rod-shaped Azobenzene with Different Alkyl Chain Length. *J. Photopolymer Sci. Tech.* 2016, *29*, 149-157.

8. Akiyama, H.; Fukata, T.; Yamashita, A.; Yoshida, M.; Kihara, H., Reworkable Adhesives Composed of Photoresponsive Azobenzene Polymer for Glass Substrates. *J. Adhesion* 2017, *93*, 823–830.

9. Yamamoto, T.; Norikane, Y.; Akiyama, H., Photochemical liquefaction and softening in molecular materials, polymers, and related compounds. *Polym. J.* 2018, *50*, 551–562.

10. Zha, R. H.; Vantomme, G.; Berrocal, J. A.; Gosens, R.; Bas de Waal; Meskers, S.; Meijer, E. W., Photoswitchable Nanomaterials Based on Hierarchically Organized Siloxane Oligomers. *Adv. Funct. Mater.* 2017, 1703952.

11. Xu, W.-C.; Sun, S.; Wu, S., Photoinduced Reversible Solid-to-Liquid Transitions for Photoswitchable Materials. *Angew. Chem. Int. Ed.* 2019, *58*, 9712 –9740.

12. Zhou, H.; Xue, C.; Weis, P.; Suzuki, Y.; Huang, S.; Koynov, K.; Auernhammer, G. K.; Berger, R.; Butt, H.-J.; Wu, S., Photoswitching of glass transition

temperatures of azobenzene-containing polymers induces reversible solid-to-liquid transitions. *Nat. Chem.* 2017, *9*, 145-151.

13. Wu, Z.; Ji, C.; Zhao, X.; Han, Y.; Müllen, K.; Pan, K.; Yin, M., Green-Light-Triggered Phase Transition of Azobenzene Derivatives toward Reversible Adhesives. *J. Am. Chem. Soc.* 2019, *141*, 7385−7390.

14. Blass, J.; Bozna, B. L.; Albrecht, M.; Krings, J. A.; Ravoo, B. J.; Wenz, G.; Bennewitz, R., Switching Adhesion and Friction by Light Using Photosensitive Guest-Host Interactions. *Chem. Commun.* 2015, *51*, 1830-1833.

15. Goulet-Hanssens, A.; Sun, K. L. W.; Kennedy, T. E.; Barrett, C. J., Photoreversible Surfaces to Regulate Cell Adhesion. *Biomacromolecules* 2012, *13*, 2958-2963.

16. Grzelczak, M.; Liz-Marzan, L. M.; Klajn, R., Stimuli-Responsive Self-Assembly of Nanoparticles. *Chem. Soc. Rev.* 2019, *48*, 1342-1361.

17. Kadem, L. F.; Holz, M.; Suana, K. G.; Li, Q.; Lamprecht, C.; Herges, R.; Selhuber-Unkel, C., Rapid Reversible Photoswitching of Integrin-Mediated Adhesion at the Single-Cell Level. *Adv. Mater.* 2016, *28*, 1799-1802.

18. Lamping, S.; Stricker, L.; Ravoo, B. J., Responsive Surface Adhesion Based on Host–Guest Interaction of Polymer Brushes with Cyclodextrins and Arylazopyrazoles. *Polymer J.* 2019, *10*, 683–690.

19. Yang, J.; Bai, R.; Chen, B.; Suo, Z., Hydrogel Adhesion: A Supramolecular Synergy of Chemistry, Topology, and Mechanics. *Adv. Funct. Mater.* 2019.

20. Zhang, J.; Ma, W.; He, X.-P.; Tian, H., Taking Orders from Light: Photo-Switchable Working/Inactive Smart Surfaces for Protein and Cell Adhesion. *ACS Appl. Mater. Interfaces* 2017, *9*, 8498-8507.

21. Tannouri, P.; Arafeh, K. M.; Krahn, J. M.; Beaupré, S. L.; Menon, C.; Branda, N. R., A Photoresponsive Biomimetic Dry Adhesive Based on Doped PDMS Microstructures. *Chem. Mater.* 2014, *26*, 4330−4333.

22. Mostafavi, S. H.; Tong, F.; Dugger, T. W.; Kisailus, D.; Bardeen, C. J., Noncovalent Photochromic Polymer Adhesion. *Macromolecules* 2018, *51*, 2388−2394.

23. Mostafavi, S. H.; Li, W.; Clark, K. D.; Stricker, F.; Alaniz, J. R. d.; Bardeen, C. J., Photoinduced Deadhesion of a Polymer Film Using a Photochromic Donor−Acceptor Stenhouse Adduct. *Macromolecules* 2019, *52*, 6311−6317.

24. Berkovic, G.; Krongauz, V.; Weiss, V., Spiropyrans and Spirooxazines for Memories and Switches. *Chem. Rev.* 2000, *100*, 1741-1753.

25. Klajn, R., Spiropyran-Based Dynamic Materials. *Chem. Soc. Rev.* 2014, *43*, 148-184.

26. Nunes, P. S.; Ohlsson, P. D.; Ordeig, O.; Kutter, J. r. P., Cyclic Olefin Polymers: Emerging Materials for Lab-on-a-Chip Applications. *Microfluid. Nanofluid.* 2010, *9*, 145–161.

27. Wojtyk, J. T. C.; Wasey, A.; Kazmaier, P. M.; Hoz, S.; Buncel, E., Thermal Reversion Mechanism of N-Functionalized Merocyanines to Spiropyrans: A Solvatochromic, Solvatokinetic, and Semiempirical Study. *J. Phys. Chem. A* 2000, *104*, 9046-9055.

28. Gorner, H., Photochromism of nitrospiropyrans : e† ects of structure, solvent and temperature. *Phys. Chem. Chem. Phys.* 2001, *3*, 416-423.

29. Richert, R., Merocyanine-Spiropyran Photochemical Transformation in Polymers, Probing Effects of Random Matrices. *Macromolecules* 1988, *21*, 923-929.

30. Levitus, M.; Talhavini, M.; Negri, R. M.; Atvars, T. D. Z.; Aramendi, P. F., Novel Kinetic Model in Amorphous Polymers. Spiropyran-Merocyanine System Revisited. *J. Phys. Chem. B* 1997, *101*, 7680-7686.

31. Athanassiou, A.; Lygeraki, M. I.; Pisignano, D.; Lakiotaki, K.; Varda, M.; Mele, E.; Fotakis, C.; Cingolani, R.; Anastasiadis, S. H., Photocontrolled Variations in the Wetting Capability of Photochromic Polymers Enhanced by Surface Nanostructuring. *Langmuir* 2006, *22*, 2329-2333.

32. Rosario, R.; Gust, D.; Hayes, M.; Jahnke, F.; Springer, J.; Garcia, A. A., Photo-Modulated Wettability Changes on Spiropyran-Coated Surfaces. *Langmuir* 2002, *18*, 8062-8069.

33. Rosario, R.; Gust, D.; Hayes, M.; Springer, J.; Garcia, A. A., Solvatochromic Study of the Microenvironment of Surface-Bound Spiropyrans. *Langmuir* 2003, *19*, 8801-8806.

34. Kim, D.; Zhang, Z.; Xu, K., Spectrally Resolved Super-Resolution Microscopy Unveils Multipath Reaction Pathways of Single Spiropyran Molecules. *J. Am. Chem. Soc.* 2017, *139*, 9447−9450.

35. Cui, L.; Zhang, H.; Zhang, G.; Zhoua, Y.; Fan, L.; Shi, L.; Zhang, C.; Shuang, S.; Dong, C., Substituent effect on the acid-induced isomerization of spiropyran compounds. *Spectrochim. Acta A* 2018, *202*, 13–17.

36. Xiao, N.; Chen, Y.; Lemieux, R.; Buncel, E.; Iftime, G.; Kazmaier, P. M., Spiropyran-Merocyanine Equilibrium in Presence of Organic Acids and Bases. *Mol. Cryst. Liq. Cryst.* 2005, *431*, 337-344.

37. Kortekaas, L.; Chen, J.; Jacquemin, D.; Browne, W. R., Proton-Stabilized Photochemically Reversible E/Z Isomerization of Spiropyrans. *J. Phys. Chem. B* 2018, *122*, 6423−6430.

38. Kook, S.-Y.; Dauskardt, R. H., Moisture-Assisted Subcritical Debondingn of a Polymer/Metal Interface. *J. Appl. Phys.* 2002, *91*, 1293-1303.

39. Sharratt, B. M.; Wang, L. C.; Dauskardt, R. H., Anomalous Debonding Behavior of a Polymer/Inorganic Interface. *Acta Mater.* 2007, *55*, 3601-3609.

40. Santos, E. A. G.-d. l.; Lozano-Gonzalez, M. J.; Johnson, A. F., Photoresponsive Polyurethane-Acrylate Block Copolymers. II. Photomechanical Effects in Copolymers Containing 6'-Nitro Spiropyranes and 6'-Nitro-bis-Spiropyranes. *J. Appl. Polym. Sci.* 1999, *71*, 267-272.

41. Athanassiou, A.; Kalyva, M.; Lakiotaki, K.; S.Georgiou; Fotakis, C., All-Optical Reversible Actuation of Photochromic-Polymer Microsystems. *Adv. Mater.* 2005, *17*, 988-992.

42. Guo, D.; Li, J.; Xie, G.; Wang, Y.; Luo, J., Elastic Properties of Polystyrene Nanospheres Evaluated with Atomic Force Microscopy: Size Effect and Error Analysis. *Langmuir* 2014, *30*, 7206−7212.

43. Rasmussen, H. K.; Fasano, A.; Stajanca, P.; Woyessa, G.; Schukar, M.; Bang, O., Mechanical characterization of drawn Zeonex, Topas, polycarbonate and PMMA microstructured polymer optical fibres. *Opt. Mater. Express* 2018, *8*, 334388.

44. Srivastava, V.; Chester, S. A.; Ames, N. M.; Anand, L., A thermo-mechanically-coupled large-deformation theory for amorphous polymers in a temperature range which spans their glass transition. *Int. J. Plasticity* 2010, *26*, 1138–1182.

45. Wu, Z.; Pan, K.; Mo, S.; Wang, B.; Zhao, X.; Yin, M., Tetraphenylethene-Induced Free Volumes for the Isomerization of Spiropyran toward Multifunctional Materials in the Solid State. *ACS Appl. Mater. Interfaces* 2018, *10*, 30879−30886.

46. Wu, Z.; Wang, Q.; Li, P.; Fang, B.; Yin, M., Photochromism of neutral spiropyran in the crystalline state at room temperature. *J. Mater. Chem. C* 2021, *9*, 6290–6296.

Chapter 4 Effect of Halogen Substitution on Energies and Dynamics of Reversible Photomechanical Crystals Based on 9-Anthracenecarboxylic Acid

4.1 Abstract

9-anthracene carboxylic acid derivatives comprise a family of thermally reversible photomechanical molecular crystals. The photomechanical response relies on a [4+4] photodimerization followed by dissociation that occurs on timescales of seconds to minutes. A combined theoretical and experimental investigation is undertaken to better understand how chemical modification of the anthracene core influences energetics of both the isolated molecule and the crystal lattice. We use both density functional theory and dispersion-corrected Moller-Plesset perturbation theory computational methods to establish orbital energies, photodimerization reaction energies, and lattice energies for a set of substituted 9-anthracene carboxylic acid molecules. The calculations reveal that steric interactions play a dominant role in the ability to form photodimers and indicate an energetic threshold of 80-90 kJ/mole for the dimerization reaction. Examination of intermolecular bonding in a subset of fluorinated **9ACs** revealed the absence of H…F intermolecular bond formation and energy differences that can explain observed trends in the dissociation kinetics and mechanical reset times. Fluorescence recovery after photobleaching experiments show that the photodimer dissociation kinetics depend on the amount of initial photodimer, preventing a straightforward correlation between halogen atom substitution and dissociation rates using the Bell-Evans-Polanyi principle. The results clarify how molecular structure affects intermolecular interactions and

photoreactivity in this family of molecular crystals, but the origin of the complex photodimer dissociation dynamics remains an open question.

4.2 Introduction

Crystals composed of photoreactive molecules (photochromes) can transform light energy directly into mechanical work.[1-3] They do this by organizing the molecules so that geometrical changes associated with the geometric photoisomerization, photodimerization, or photocyclization add together in specific directions determined by the crystal axes. Various classes of both intra- and intermolecular reactions have been harnessed to generate this work. In the latter class, [2+2] [4-12] and [4+4] [13-16] photodimeriztion reactions are commonly used. To realize thermally reversible (T-type) photomechanical crystals based on photodimerization, the photodimer must be sufficiently unstable so that its dissociation proceeds rapidly at room temperature. In this context, we have synthesized and studied a class of substituted 9-anthracenecarboxylic acid (**9AC**) derivatives that crystallize in a head-to-head (*hh*) geometry due to intermolecular hydrogen bonding between neighboring stacks.[17] The *hh* geometry gives rise to steric interactions between the COOH groups on cofacial molecules that destabilize the C-C bridge bonds of the photodimer and cause it to spontaneously dissociate back into the monomer pair.[18-21] This ability of the crystal to reset itself after photodimerization makes it a T-type photomechanical material that could have practical applications.

The **9AC** core provides the basis for an entire class of photomechanical molecular crystals because chemical substituents can be added to the anthracene ring in order to tune the material properties. The effects of halogen atom and methyl group substitution on the

photodimerization and recovery kinetics have been investigated in two previous papers.[22, 23] One surprising result was that F-atom substitution at different carbons around the anthracene ring led to photodimer dissociation rates that varied by more than an order of magnitude, despite virtually identical crystal packing geometries. To explain this observation, we hypothesized that intermolecular H…F interactions might affect the relative stabilities of the monomer and photodimer in the different molecular crystals.[23] If the rate of photodimer dissociation can be controlled by the F substitution pattern, this would provide a strategy to design molecular crystals with desired properties, like fast mechanical recovery times.

In this chapter, we undertake a combined theoretical and experimental investigation to better understand how chemical modification of the **9AC** core influences energetics of both the isolated molecule and the crystal lattice. The goal is to determine the relative importance of local (pairwise) versus nonlocal (crystal) interactions in determining the photochemical reactivity of monomer pairs and the stability of photodimers. We examine a large set of substituted **9AC** molecules (Figure 4.1) using both density functional theory (DFT) and dispersion-corrected Moller-Plesset perturbation theory (MP2D)[24] computational methods to establish orbital energies, photodimerization reaction energies, and lattice energies. The Bell-Evans-Polanyi (BEP) principle provides a way to correlate the energy difference between a monomer pair and photodimer with the activation energy and thus the thermal dissociation rate.[25-28] These calculations reveal that steric interactions play a dominant role in the ability to form photodimers and suggest there exists an energetic threshold for the formation of the photodimer, but they fail to show any relation between

enthalpy differences and observed photodimer dissociation rates. Additional kinetic experiments show that the photodimer dissociation, as measured by the recovery of the monomer fluorescence, is highly nonlinear and depends on the amount of initial photodimer created by the ultraviolet (UV) pulse. The complex reaction kinetics in the crystals prevent a straightforward correlation between halogen atom substitution and dissociation rates. This work clarifies how molecular structure affects intermolecular interactions and photoreactivity in the crystal, but the origin of the complex reaction dynamics in this class of hydrogen-bonded crystals remains unclear.

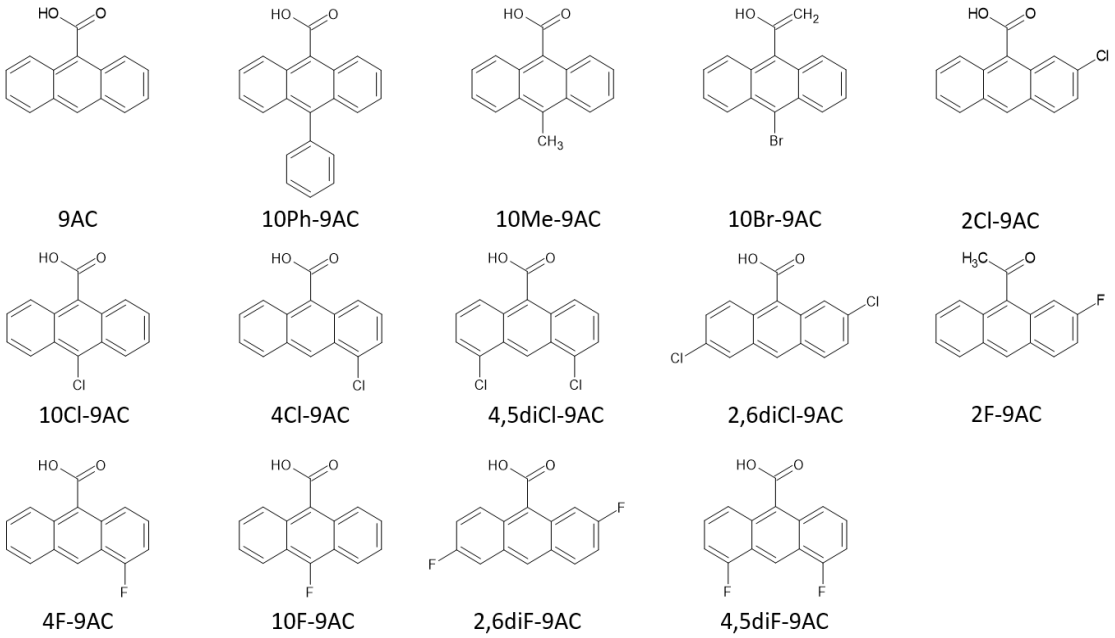

Figure 4.1: 9-anthracene carboxylic acid derivatives studies in this paper, along with abbreviations use in the text.

4.3 Experimental Methods

The syntheses of the **10F-9AC**, **10Methyl-9AC**, **10Cl-9AC**, **10Br-9AC**, and **10Ph-9AC** were previously reported.[22] The syntheses of **2F-9AC**, **4F-9AC**, and **2,6diF-9AC** were described previously.[23] Detailed synthetic procedures for **4,5diF-9AC**, **2Cl-9AC**, **4Cl-9AC**, and **4,5diCl-9AC** is described in the Supporting Information. Crystal structures for all molecules except **4Cl-9AC** and **2Cl-9AC** are also given in the Supporting Information.

The measurement of the fluorescence recovery process was performed using an Olympus IX70-inverted microscope. Crystals of the compounds were placed on glass microscope slides. Large rectangular crystals were used for measurements because of their resistance to bending and deformation, preventing misalignment of the pump and probe beams. The alignment of each crystal was confirmed after UV exposure to ensure accurate fluorescence recovery data. Utilizing a pump-probe setup a 405 nm laser was used to irradiate samples for a predetermined time then probed using a less intense 405 nm beam. A Melles Griot Electronic Shutter Controller (04 ISC 850) and a custom LabView program were used to control the pump exposure. The probe spot radius of 17 μm was three times smaller than the 55 μm pump beam. The beam was modulated by a chopper at a frequency of 100 Hz. The resulting signal was obtained using a lock-in amplifier with a photomultiplier tube. To reduce probe beam exposure, intermittent blocking was performed manually during the data collection.

The interpretation of the fluorescence recovery experiments relies on the assumption that the fluorescence is linearly proportional to the monomer population. Previous

experiments showed that the fluorescence of the monomer crystal originates from an excimer and is redshifted about 100 nm below the absorption edge[29], allowing us to assume that reabsorption of the fluorescence by monomer or photodimers is negligible and these optical nonlinearities can be neglected. In the same work, it was found that the loss of fluorescence was linearly proportional to the UV photon dose, again consistent with a linear relation between the loss of monomer and loss of fluorescence. Thus the available data suggests that the fluorescence signal is a good surrogate for the monomer pair population.

4.4 Computational Methods

The geometries of gas-phase monomers, dimers, and tetramers of the **F-9AC** species and their photodimerized analogs were optimized using the BLYP[30, 31] generalized gradient approximation (GGA) density functional with the D3(BJ) dispersion correction[32, 33] and the def2-TZVP basis set.[34] Frontier orbital energies and quasi-particle gaps were then computed for gas-phase **F-9AC** monomers using single-point energies computed with the range-separated hybrid ωB97X-D density functional[35] in the aug-cc-pVTZ basis set.[36] The highest-occupied molecular orbital (HOMO) energy was equated to the negative of the ionization potential, while the lowest-unoccupied molecular orbital (LUMO) energy was the set to be the negative of the electron affinity. The ionization potentials and electron affinities were computed via the ΔSCF approach[37], taking the energy difference between the neutral species and its corresponding cation or anion. Optical gaps corresponding to vertical excitations were computed via time-dependent density functional theory (TDDFT)

using the same ωB97X-D/aug-cc-pVTZ model in implicit cyclohexane polarizable continuum solvent.[38]

The energetics of anthracene photodimerization are notoriously difficult to model, and the results from many common density functionals are both quantitatively and qualitatively incorrect.[24, 39] Therefore, the **F-9AC** species and their gas-phase photodimerization reactions in dimer and tetramer clusters were computed with dispersion-corrected second-order Møller-Plesset perturbation theory (MP2D)[24], which has been shown to model anthracene photodimerization energetics to within a few kcal/mol of coupled cluster theory benchmarks. The MP2D calculations were extrapolated to the complete basis set (CBS) limit by combining Hartree-Fock/aug-cc-pVQZ results with correlation energies extrapolated from the aug-cc-pVTZ and aug-cc-pVQZ basis sets.[40] These large basis sets were chosen to help converge the energetics and to reduce basis set superposition error. Because the counterpoise correction[41] is ill-defined for intramolecular interactions, it was not employed here to avoid inconsistencies between the description of the intermolecular π-stacking interactions in the reactants versus the intramolecular interactions in the photodimer product. The TDDFT calculations were performed using Gaussian 16 RevC.01.[42] All other gas-phase calculations were performed using PSI4[43], employing density fitting algorithms and the default auxiliary basis sets throughout. The MP2D dispersion correction is available in the current developmental version of PSI4 or can be downloaded as a stand-alone library for use with any MP2 implementation.

Solid-state calculations on **F-9AC** crystals were performed using the B86bPBE generalized gradient approximation functional[44, 45] and the exchange-hole dipole moment

(XDM) dispersion correction[46] using QuantumEspresso 6.4.1[47, 48], a 50 Ry planewave cutoff, and Monkhorst-Pack grids with a k-point density of ~0.04 A^{-1}. Core electrons were treated via the projector augmented wave (PAW) approach using PAW potentials for H, C, and F generated with A. Dal Corso's Atomic code v6.1. Experimental crystal structures were relaxed with lattice parameters held fixed at their experimental values. For higher accuracy and consistency with the gas-phase calculations, the single-point crystal lattice energies of the optimized structures were then refined by extracting the key reactive tetramer (two π-stacked pairs of hydrogen bonded dimers), then replacing the DFT energy of that gas-phase tetramer with the corresponding MP2D energy. This approximation is essentially the same as the monomer-correction approach[49] that has proved extremely useful in a number of other organic crystals,[49-51] including the related 9-tertbutyl anthracene ester.[52] The approximation amounts to describing the most important local interactions—those within the key reactive tetramer—with MP2D, while the longer-range contributions arising from the interaction of that tetramer with the surrounding crystal lattice are modeled with periodic DFT. For further insight, the lattice energies were decomposed into contributions arising from within the central tetramer, between the tetramer and the rest of the crystal, and the energy required to distort the monomer from its optimal gas-phase geometry to the crystalline conformation. The interactions in the tetramer were further decomposed into all possible pairwise interactions (consisting of hydrogen bonded pairs, π-stacked pairs, and "diagonal" pairs) plus the residual non-pairwise-additive "many-body" contribution.

4.5 Results and Discussion

4.5.1 Effect of Halogen Substitution on Molecular Electronic Properties

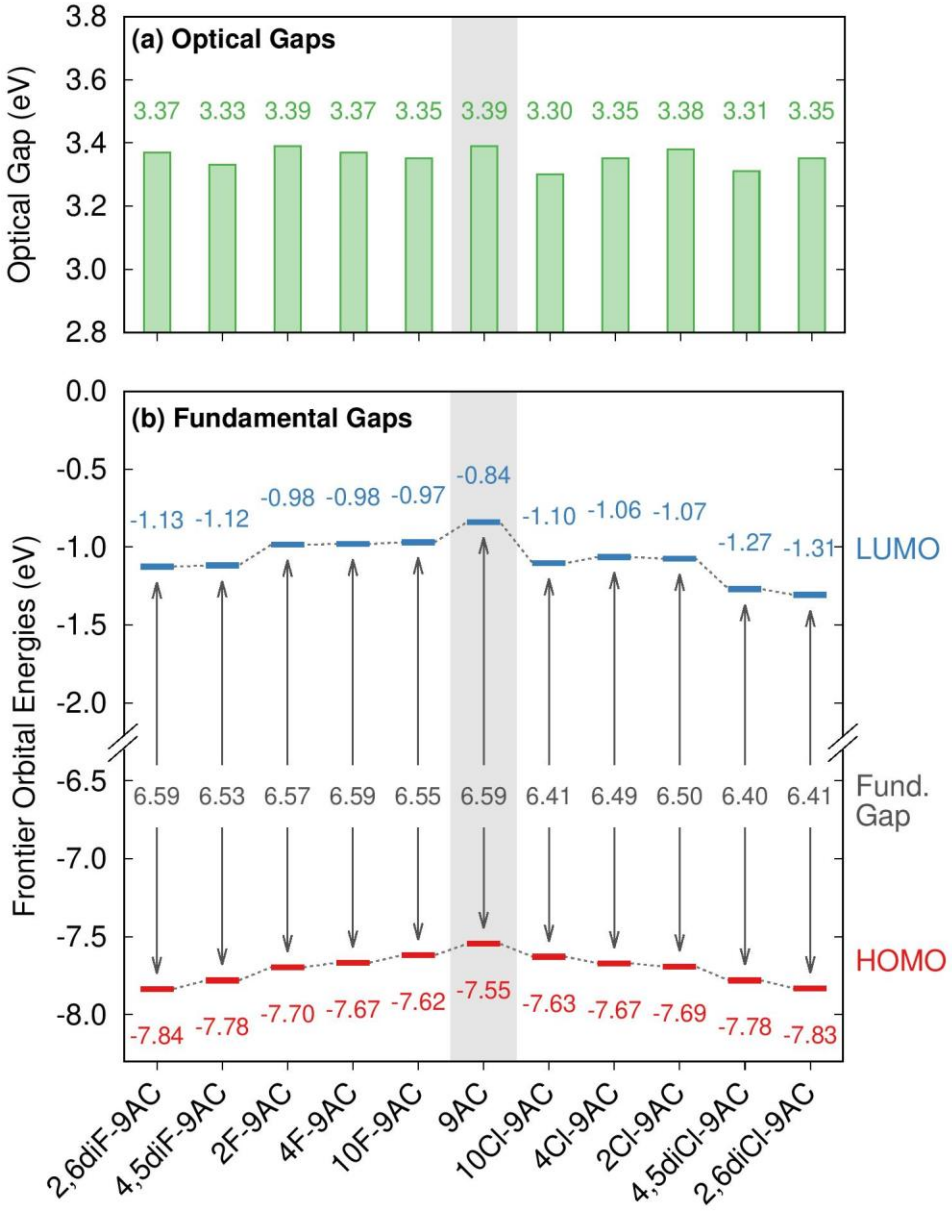

Figure 4.2: a) Optical gaps calculated for various 9AC derivatives shown in Figure 4.1. **b**) Effect of halogen substitution pattern on the HOMO/LUMO levels of 9AC.

We first wanted to understand how chemical substitution affects the photophysical properties of individual molecules. In the simplest limit, electron withdrawing groups are expected to lower the HOMO and LUMO energies. From a practical standpoint, this should make the molecule more difficult to oxidize and increase its stability, since reaction with ambient O_2 molecules at the C10 and C9 carbons is a major side reaction for photoexcited anthracene molecules leading to 9,10-endoperoxyanthracene derivative that can rearrange to give anthraquinones.[53, 54] Figure 4.2 shows the calculated gas-phase HOMO/LUMO energy level shifts for the various **9AC** derivatives in Figure 4.2. As expected, the addition of electron-withdrawing atoms like Cl and F systematically lowers both orbital energies. Surprisingly, Cl substitution seems to have a slightly larger effect, even though it is less electronegative than F. But although the individual orbitals shift by as much as 0.5 eV upon halogen substitution, the HOMO/LUMO shifts tend to offset each other, with the net result that the HOMO/LUMO gap does not change by more than 0.2 eV.

The stability of the HOMO-LUMO gap with respect to chemical substitution is mirrored by the calculated optical gap. Figure 4.3a shows representative absorption spectra for **9AC** and some fluorinated derivatives. All derivatives retain the characteristic anthracene vibronic lineshape, suggesting that the S_0-S_1 transition has a similar electronic character in all of them. In Figure 4.3b we plot the experimental S_0-S_1 transition energies in cyclohexane, as well calculated S_0-S_1 optical energies in implicit cyclohexane solvent for **9AC**, **10F-9AC**, **2F-9AC**, **4F-9AC**, **2,6diF-9AC** and **4,5diF-9AC**. Fluorine substitution causes the measured absorption peak to shift by up to 0.1 eV, while the calculated S_0-S_1 gaps show more scatter but the same magnitude of variation. The

calculated S_0-S_1 energies are consistently about 0.1 eV greater than the experimental energies, which is within the typical accuracy for TDDFT calculations.[55, 56] The experimental and calculated S_0-S_1 energies and absorption lineshapes are consistent with previous work showing that halogen atom substitution on the anthracene ring can shift the absolute HOMO/LUMO positions but has little effect on the molecule's optical properties.[57, 58]

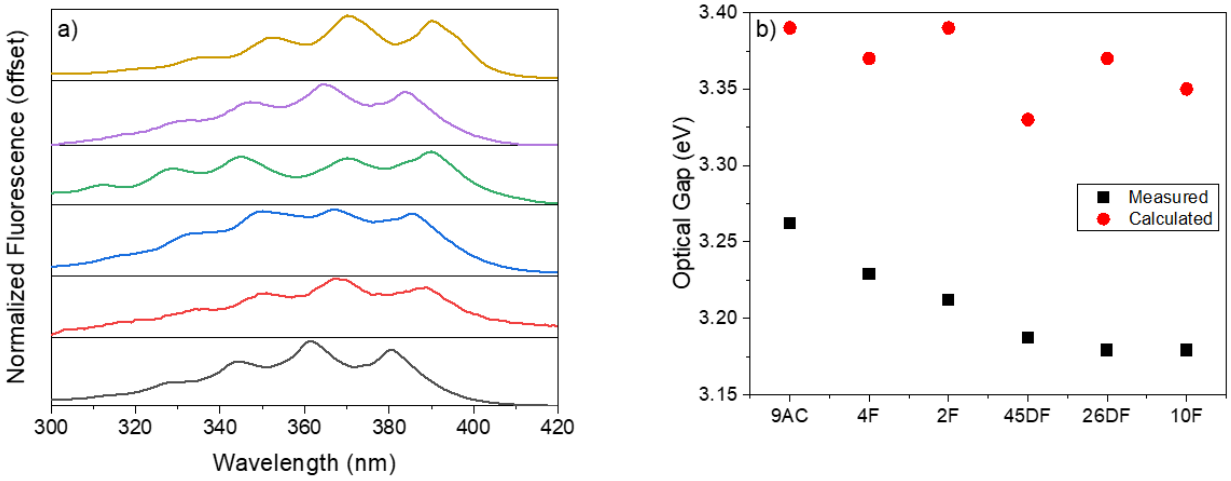

Figure 4.3 a) Normalized absorption spectra of **10F-9AC** (brown), **4F-9AC** (purple), **2,6diF-9AC**, **2F-9AC** (blue), **4,5diF-9AC** (red), and **9AC** (black) in cyclohexane b) Comparison of calculated (red) and measured (black) optical gaps for fluorinated **9AC** compounds.

4.5.2 Effect of Halogen Substitution on Dimer Energetics

In solution, anthracene carboxylic acids photodimerization typically favors the head-to-tail (*ht*) conformation.[59, 60] In the crystal form, hydrogen bonds between COOH groups on opposing molecules lock the molecules in the *hh* conformation along the one-dimensional stacks. Gas-phase MP2D calculations comparing the *hh* and *ht* arrangements of the photodimer (Table 1) show that the *hh* photodimer geometry is generally ~32-35 kJ/mol less stable than the *ht* one due to the steric clash introduced by having the two

COOH groups on the same side in the *hh* geometry. In contrast, the energy differences between the *hh* and *ht* geometries of the unreacted gas-phase dimers are only ~3-7 kJ/mol. Taken together, this means that the reaction energies ΔE_{rxn} = *E(photodimer) – E(unreacted)* for the *hh* dimerization are considerably more endothermic than the *ht* ones (Table 1). This explains why the photodimerization is so easily reversible in the **9AC** crystals at room temperature, since only the highly endothermic *hh* dimerization can occur in the crystalline state. Most of the fluorine substitutions considered impact the energy difference between the *ht* and *hh* photodimers minimally (*i.e.* by 2—3 kJ/mol), except for **10F-9AC** where the *hh* photodimer is actually 14 kJ/mol more stable than the *ht* photodimer. In this case, the unfavorable electrostatic repulsion between the COOH and/or F groups on the adjacent anthracene units mean that neither the *ht* nor *hh* arrangement is particularly favored. Moreover, both *hh* and *ht* configurations of **10F-9AC** exhibit more endothermic gas-phase photodimerization energies ΔE_{rxn} than any of the other derivatives (Table 4.1), according to these calculations.

Next, we consider the gas-phase MP2D *hh* photodimerization energies ΔE_{rxn}*(hh)* across a broader set of **9AC** derivatives in Table 2, including both ones that have been tested experimentally and other hypothetical mono-halogenated **9AC** derivatives. The crystal photoreactivity was determined by direct observation of the loss of monomer fluorescence and mechanical changes under 405 nm irradiation. Figure 4.4 plots ΔE_{rxn} for several **9AC** derivatives and indicates whether they exhibit experimental reactivity in the crystal form. The photodimerization of these **9AC** derivatives is consistently endothermic, and there seems to be a ΔE_{rxn} threshold at around 90 kJ/mol, above which dimer formation

is prevented. These higher-energy photodimerization reactions have larger substituents located at the 10-position that cannot avoid interacting with each other. Among the hypothetical cases, dimerization appears energetically feasible for any fluorine, chlorine, or bromine mono-halogenation at the 2, 3, or 4 positions, with dimerization reaction energies 62--73 kJ/mol. Mono-fluorination at the 1 position also exhibits a dimerization energy comparable to that of **10F-9AC**, while reactions involving larger Cl and Br substituents in the 1 position are unlikely, since they have ΔE_{rxn} of 100 kJ/mol or more. Similar to the **10X-9AC** derivatives, these highly endothermic reaction energies stem from steric clashes between the COOH and the halogen groups. It should be noted that ΔE_{rxn} is the difference between ground state isomers and thus in principle provides no information about the excited state potential energy surface that determines the photodimerization yield. However, we suspect that it indicates the degree of steric interference within the dimer, which is an important factor in determining whether photodimerization proceed on the excited state. This correlation with sterics probably explains why it correlates with photoreactivity as well.

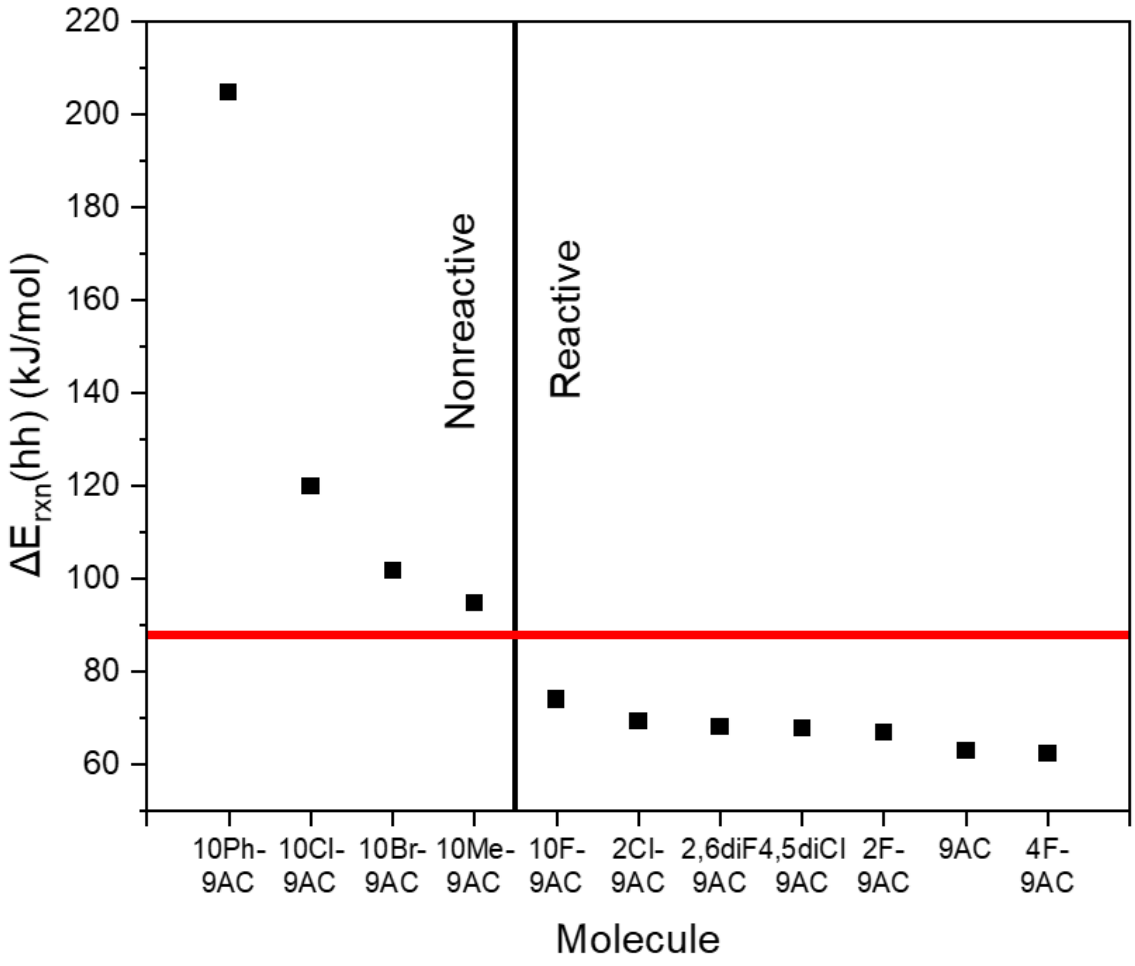

Figure 4.4: Predicted gas-phase ΔE_{rxn} dimerization energies for various **9AC** derivatives, calculated for monomer pairs. The red line represents the approximate energy threshold above which photodimerization is not observed in the crystal form.

Species	Monomer Pair ($E_{hh} - E_{ht}$) (kJ/mol)	Photodimer ($E_{hh} - E_{ht}$) (kJ/mol)	ΔE_{rxn}(hh) (kJ/mol)	ΔE_{rxn}(ht) (kJ/mol)
9AC	4.0	34.3	63.1	32.8
2F-9AC	7.3	34.8	67.0	39.4
4F-9AC	-5.0	35.1	62.3	22.2
10F-9AC	-4.7	-13.5	74.0	82.8
2,6diF-9AC	6.8	32.3	68.1	42.6
4,5diF-9AC	-3.3	32.1	60.4	25.0

Table 4:1 Gas-phase MP2D dimer energy differences comparing **9AC** derivatives with head-to-head (*hh*) and head-to-tail (*ht*) geometries. 1st column: *hh* versus *ht* energy difference for unreacted monomer pair; 2nd column: *hh* versus *ht* energy difference for dimerized pair; 3rd column: dimerization reaction energy for *hh* pair; 4th column: dimerization reaction energy for *ht* pair.

Molecule	X=F	X=Cl	X=Br	X=Me	X=Ph
9AC	63.1[a]	—	—	—	—
1X-9AC	76.5[c]	100.0[c]	106.2[c]	—	—
2X-9AC	67.0[a]	69.3[a]	72.8[c]	—	—
3X-9AC	66.5[c]	67.9[c]	71.7[c]	—	—
4X-9AC	62.3[a]	66.2[c]	67.1[c]	—	—
10X-9AC	74.0[a]	119.9[b]	101.7[b]	94.9[b]	204.7[b]
2,6diF-9AC	68.1[a]	—	—	—	—
4,5diF-9AC	60.4[a]	67.8[a]	—	—	—

Table 4:2 Gas-phase MP2D predicted dimerization energies (ΔE_{rxn}(*hh*)) for various **9AC** compounds in the *hh* configuration, in kJ/mol. a) reactive; b) non-reactive; c) not tested.

4.5.3 Effect of Halogen Substitution on Tetramer and Crystal Energetics

In order to test our hypothesis that intermolecular bonding plays an important role in the reaction kinetics, we had to examine larger systems. The metastable nature the **9AC** photodimer has prevented experimental characterization of its neat crystal structure, although solvates have been investigated.[61] Without knowledge of the photodimer crystal structures, the computational modeling instead focused on a gas-phase tetramer cluster model in which two pairs of hydrogen bonded monomers could be photodimerized, as illustrated in Figure 4.5. These more expensive calculations were performed on a subset of the experimentally investigated molecules in Section B. These clusters were extracted from the unreacted monomer crystal, and then either one or both of the monomer pairs in the tetramer were converted to photodimers and the tetramer structure was relaxed. The photodimerization reaction energy in the tetramer is moderately less favorable than in the dimer. As shown in Table 3, the first dimerization within the tetramer is ~11 kJ/mol more endothermic on average, while the second one is ~19 kJ/mol more endothermic. These higher reaction energies reflect the geometric constraints associated with preserving the COOH hydrogen bonds between the stacks. Nevertheless, the qualitative trends in the reaction energies for the different F substitution patterns in the tetramer remain similar to those in the isolated dimer. **4F-9AC** again exhibits the lowest ΔE_{rxn}, while **10F-9AC** has largest ΔE_{rxn} and thus would be predicted to be the least stable photodimer.

Species	Dimer ΔE_{rxn}(hh) (kJ/mol)	Tetramer ΔE_{rxn}(hh) (kJ/mol)	$\Delta E_{rxn,2}$(hh) (kJ/mol)	$\Delta E_{rxn,avg}$(hh) (kJ/mol)
9AC	63.1	73.2	81.7	77.5
2F-9AC	67.0	79.6	83.8	81.7
4F-9AC	62.3	72.1	80.6	76.4
10F-9AC	74.0	84.3	93.4	88.9
2,6diF-9AC	68.1	79.3	88.2	83.8

Table 4:3 Comparison of dimerization reaction energies of fluorinated **9AC** compounds in dimer, tetramer with one pair reacted, and tetramer with both pairs reacted ($\Delta E_{rxn,2}$). The 4th column is an average of the two tetramer reaction energies.

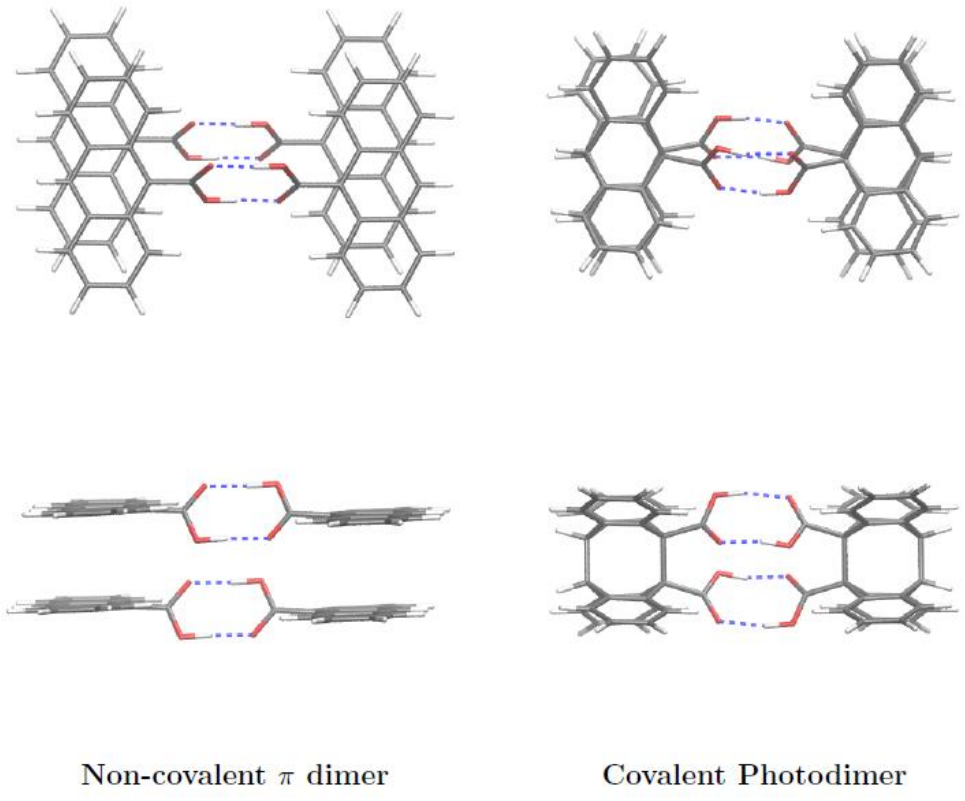

Figure 4.5 Top and side view of the **9AC** tetramer before and after double photodimerization. The photodimer structure was optimized in the gas phase.

The similarities of the dimer and tetramer cluster results motivated us to examine the energetics of the monomer crystal lattice in more detail. The goal was to look for any variations in the intermolecular forces that arise from fluorine substitution. The crystal lattice energies are analyzed by decomposing them into contributions arising from (i) distortion of the monomer from its gas-phase to crystalline conformation, (ii) the interaction energy within the key tetramer unit, and (iii) the interaction of that tetramer with the rest of the crystal lattice. As shown in Figure 4.6a, the intermolecular interactions within the tetramer represent the strongest contribution to the lattice energy, but the interactions between the tetramer and the lattice energy are almost as large.

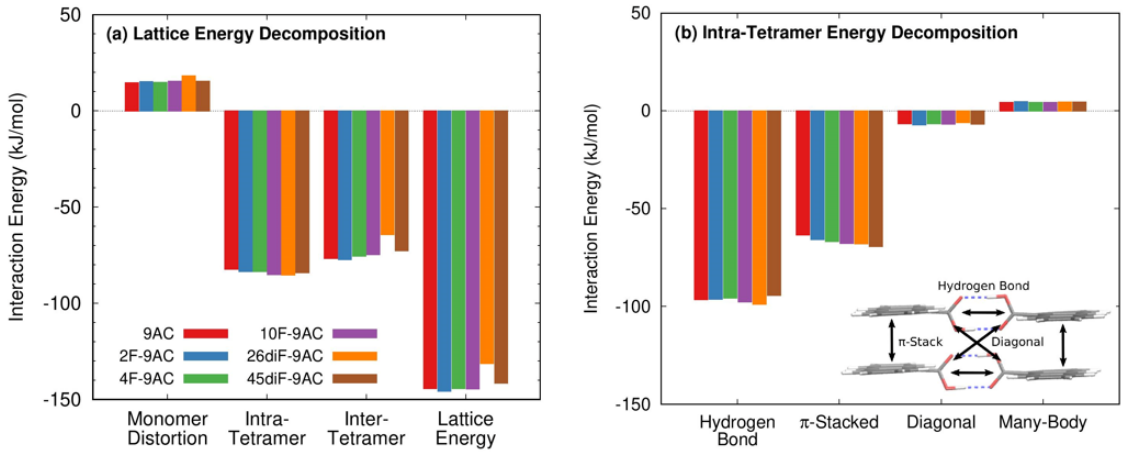

Figure 4.6 a) Effect of fluorine substitution on various lattice energy terms for six different **9AC** derivatives. **b)** Effect of fluorine substation on tetramer energy terms for the same **9AC** derivatives. In all cases, the changes induced by different locations of the F-atom amount to only a few kJ/mol.

One might anticipate the fluorine substitution could create additional hydrogen bonding between tetramer units that would increase the lattice energy. However, the data provides little evidence for the role of intermolecular H…F bonding. With typical H...F distances of 2.3-2.5 Angstroms, the intermolecular H…F bonds are relatively weak. If

such H…F bonds were important, they would impact the interaction energy between the tetramer and the rest of the lattice, but these interactions vary by only a few kJ/mol across most of the derivatives (Figure 4.6a). The only notable exception occurs for **2,6-diF-9AC**, for which F…F repulsion actually weakens these interactions by about ~10 kJ/mol relative to the other derivatives. Fluorine substitution has only minor impacts on the other energy contributions as well. For example, the interactions within the tetramer vary by only ~2 kJ/mol across the derivatives, and the differences among the monomer distortion energies are similarly small (with **2,6-diF-9AC** again being a moderate exception). In the end, the total lattice energies for all derivatives lie in the 141-146 kJ/mol range, except for **2,6-diF-9AC** at 131 kJ/mol (due to the aforementioned F…F repulsion and larger distortion energy penalties).

It seemed surprising the F substitution had such small impacts on the tetramer energies, since it is known that halogenation can impact pi-stacking interactions appreciably.[62] Figure 4.6b further decomposes the intermolecular interactions within the key tetramer into the sum of the two pairwise hydrogen bond interactions, the sum of the two π-stacking energies, the two pairs of "diagonal" interactions, and the residual many-body contribution arising from the beyond-pairwise interactions within the tetramer. As expected, we do observe that fluorination systematically increases the strength of the π-stacking interactions by up to 5 kJ/mol, and the di-fluorinated species stacks are stabilized more than the mono-fluorinated ones. However, the other interactions vary less systematically with fluorine substitution, and the net effect is that the improved π -stacking energetics are largely cancelled out in the tetramer as a whole. This conclusion is consistent with the fact that

most of the derivatives exhibit almost identical crystal packing (except for **10F-9AC**). Overall, these results highlight how the details of crystal packing stability on the whole can defy simple intuitive logic derived from knowledge of individual pairwise intermolecular interactions.

Given the weak effect of F-substitution on the crystal energetics, it is perhaps not surprising that we find no strong correlation between the energetics and the dimer dissociation rate. According to the BEP principle, ΔE_{rxn} should also correlate with the dissociation rate through its activation energy. In Figure 4.7a, we plot the dissociation half lives ($\tau_{1/2}$ from reference [23])versus the dimer ΔE_{rxn} for molecules **9AC**, **10F-9AC**, **2F-9AC**, **4F-9AC**, and **2,6diF-9AC**. Unlike Figure 4.4, there is no obvious correlation. The inclusion of dimer-dimer interactions by using a tetramer cluster does not change this situation, as shown in Figure 4.7b. In both cases, the largest predicted *hh* photodimerization energy ΔE_{rxn} in Table 1 is found for **10F-9AC**, while the smallest one occurs for **4F-9AC**. If the dimer→monomer pair reactions of the different derivatives have similar transition state structures, the BEP principle would predict the **10F-9AC** dimer to have the fastest dissociation rate and **4F-9AC** to have the slowest rate. This is precisely the opposite of what is observed experimentally.

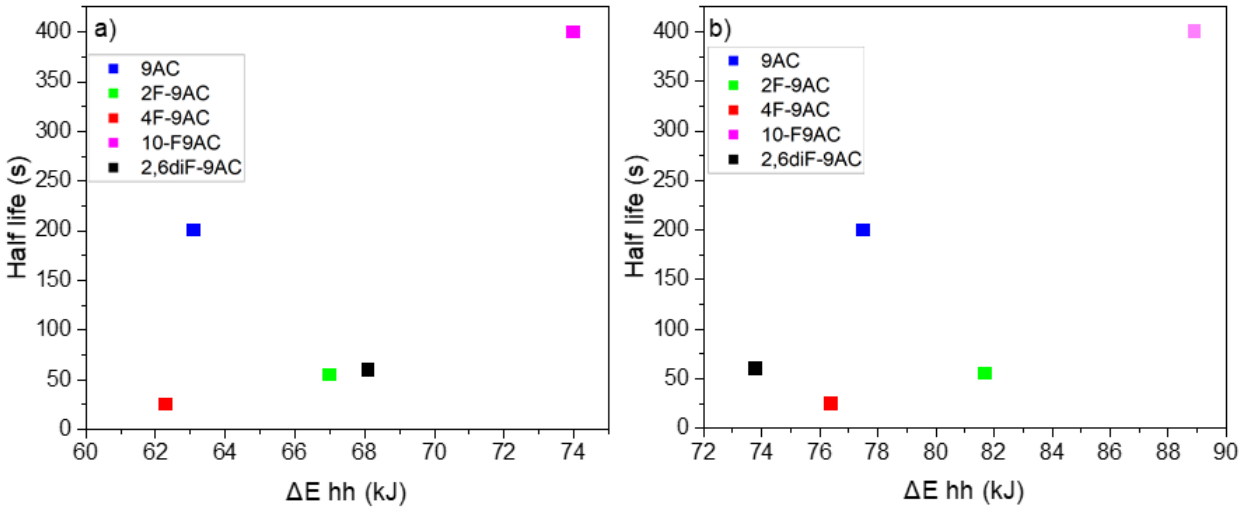

Figure 4.7 Fluorescence recovery times ($\tau_{1/2}$) taken from reference [23] plotted versus the calculated **a)** dimer and **b)** tetramer photodimerization energies.

4.5.4 Nonlinear Photodimer Dissociation Kinetics

The absence of a correlation between ΔE_{rxn} and the photodimer lifetimes in Figure 4.7 suggests that the BEP principle cannot be naively applied to this class of reactions. One assumption of the BEP model is that the Arrhenius prefactors and transition state structures are similar within the family of compounds under study. While this assumption seems reasonable for the **9AC**s, it may be that the transition state is much more sensitive to the surrounding crystal environment than the minimum energy monomer and dimer configurations. A second possibility is that the accurate calculation of the photodimer energies requires taking the full crystal lattice into account, rather than isolated clusters. However, there is no hint from the monomer calculations that the inclusion of such terms would shift the relative energies by more than a few kJ/mol. Rather than focusing on energetics, a third explanation centers on the possibility that the bulk photodimer

dissociation kinetics are more complicated than the simple two-state model that underlies the BEP principle.

In the ideal case, the photodimerization can be described by a simple two-state model subject to well-defined forward and backward first-order rate constants that are independent of concentration. This assumption is usually valid in dilute solution, where the molecules react independently in a homogeneous environment. But in a crystal, where the reacting molecules are in intimate contact, the surrounding can change as the fraction of dimers evolves, leading to a time-dependent rate that changes as the reaction progresses.[63-65] In this limit, a single rate cannot describe the process and it is no longer possible to make a straightforward connection between equilibrium energies and dynamics. One hallmark of such nonlinear kinetics is their dependence on initial concentrations. Recent studies on the kinetics of the dimer dissociation in **4F-9AC** crystals showed strong deviations from first-order exponential behavior, where a larger initial photodimer concentration slowed down the dissociation reaction and the recovery of the monomer fluorescence signal.[29] The recovery was also sensitive to the presence of a 100× weaker probe beam that could stall the monomer recovery. We interpreted these concentration-dependent decays as evidence of cooperative dynamics, perhaps related to nucleation.

To determine whether the linear kinetic model is valid for the other **9AC** derivatives, we measured the kinetics of monomer recovery using a fluorescence recovery after photobleaching (FRAP) experiment. We were careful to only use an intermittent probe technique, so the fluorescence detection did not perturb the recovery and found concentration-dependent kinetics in all of them to varying degrees. Figure 4.8 compares

the high and low bleach (initial photodimer concentration) recovery curves for molecules **9AC**, **10F-9AC**, **2F-9AC**, **4F-9AC**, and **2,6diF-9AC**. All exhibit slower decays for large bleach depths (high initial photodimer conversion), with the effect being most pronounced for **9AC** and least pronounced for **2,6diF-9AC** and **10F-9AC**. Note that **9AC** can be grown in two different polymorphs, monoclinic and triclinic.[22] This different symmetry arises from the slightly different arrangement of the one-dimensional stacks along the *b*-axis, as detailed in the Supporting Information. The same nonlinear behavior was seen in both polymorphs (Supporting Information), providing additional experimental evidence that subtle changes in stack orientation do not strongly affect the dissociation kinetics.

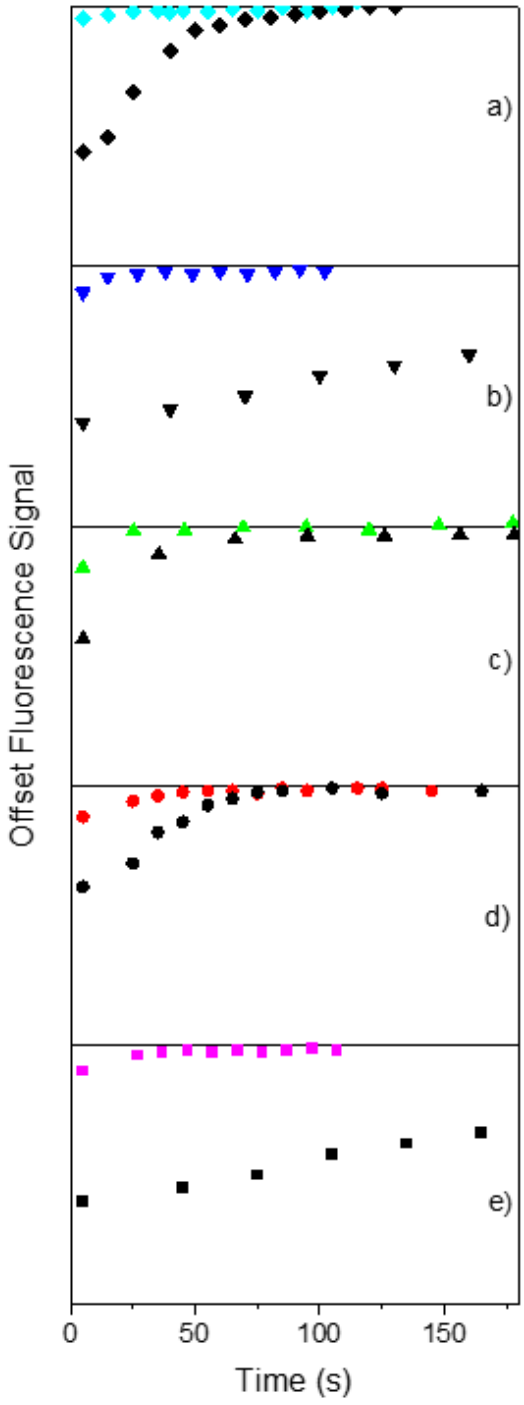

Figure 4.8 Fluorescence recovery after photobleaching curves for **a) 4F-9AC, b) 10F-9AC, c) 2,6diF-9AC, d) 2F-9AC**, and **e) 9AC** after small (~5% colored symbols) and large (~50% black symbols) photodimer conversions. The data in **a)** is taken from reference [29].

As in our previous paper[23], we can to parameterize the data in Figure 4.8 by extracting $\tau_{1/2}$, the time required for the fluorescence recovery to achieve 50% of its pre-bleach value. These values are summarized in Table 4. For low bleach depths (low initial photodimer concentrations), the $\tau_{1/2}$ recovery times are similar for all molecules except **10F-9AC**, as shown in Figure 4.9a. For deeper bleaches, Figure 4.9b shows how the $\tau_{1/2}$ times diverge by a factor of 10. From Figure 4.9a, it appears that any discrepancy between the $\tau_{1/2}$ values for different compounds is magnified when large (>20%) photodimer conversions are measured. The similarity of the low conversion recovery rates among the different compounds suggests that local energetic considerations, predicted by theory to be similar, are controlling the dissociation of dilute dimers. At higher concentrations, however, it is possible that many-body effects become important, and these cannot be identified by the dimer and tetramer level of theory employed here. We note that **10F-9AC** continues to be an outlier, even for low conversions.

	Shallow Bleach Recovery ($\tau_{1/2}$) (s)	Deep Bleach Recovery ($\tau_{1/2}$) (s)
9AC	7.2	174.5
2F-9AC	15.3	54.4
4F-9AC	6.5	31.5
10F-9AC	270.1	333.2
2,6diF-9AC	6.8	21.5

Table 4:4: The half times from shallow (~10%) and deep (~50%) fluorescence bleaches (fraction of crystal converted to the nonfluorescent photodimer) for selected **9AC** compounds.

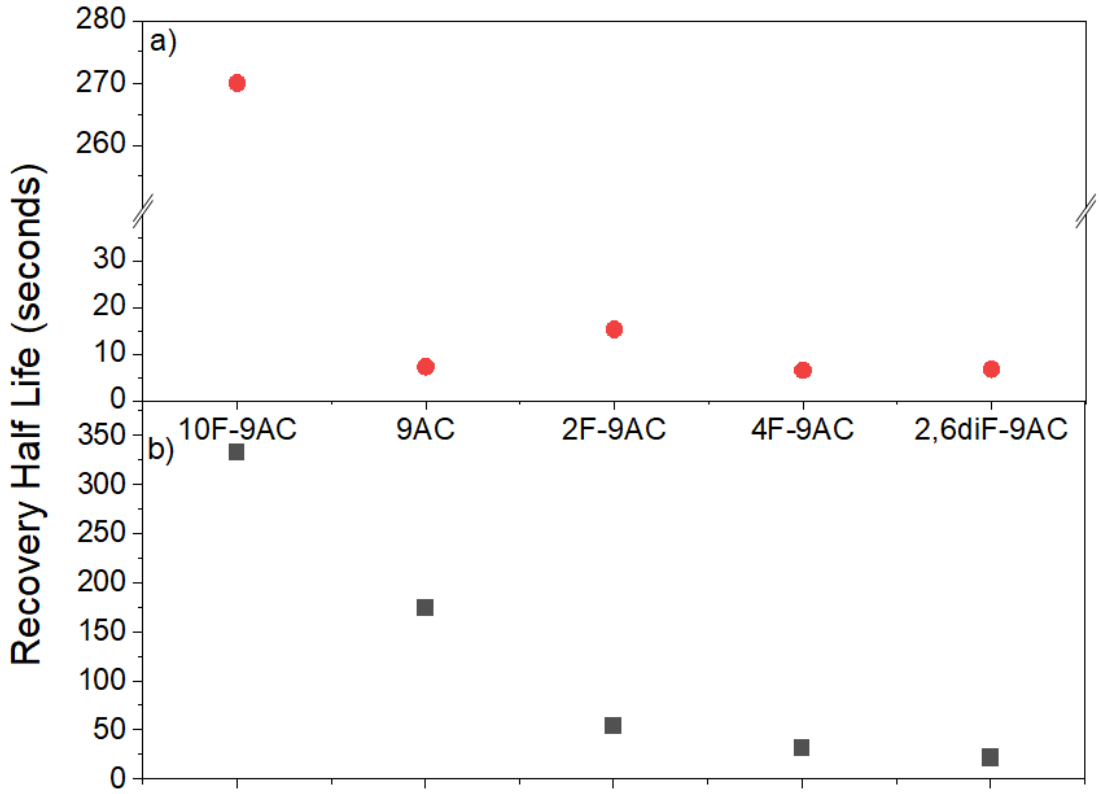

Figure 4.9: Fluorescence recovery times ($\tau_{1/2}$) for **9AC**, **10F-9AC**, **2F-9AC**, **4F-9AC**, and **2,6diF-9AC** compounds after **a)** small (~5%) photodimer conversion and **b)** large (~50%) photodimer conversion.

In an earlier paper, we did not realize that the bleach depth and the presence of the probe beam could have a significant effect on the recovery dynamics.[23] Although the qualitative conclusions from that work are still valid, the quantitative comparison of recovery times is considerably more complex than we appreciated at that time. The origin of the variable dissociation behavior among the **9AC** derivatives remains a mystery. The kinetic behavior of a photodimer surrounded by monomer pairs must be quite different from that of one surrounded by other photodimers. It is possible that the strong intermolecular hydrogen-bond interactions in the **9AC** family make these compounds more

susceptible to such cooperative phenomena. It is also possible that this kinetic phenomenon is affected by presence of crystal defects, which could vary between derivatives. One clue to the origin of the nonlinear kinetics is that **2,6-diF-9AC** appears to be the least susceptible to the cooperative effects, with the recovery times at both high and low bleach depths being quite similar. This relative insensitivity is consistent with its weaker intermolecular interactions as predicted by calculations shown in Figure 4.6a. Weaker interactions can allow the dissociation kinetics to be more effectively decoupled from neighboring sites and lead to more standard first-order kinetics. Even though a direct connection to the rate is not possible because there is no single, well-defined Arrhenius rate, this observation provides a starting point for future investigations.

4.6 Conclusion

To summarize, extensive calculations of the crystal energetics and kinetic measurements for a series of **9AC** derivatives have provided insight into the reaction dynamics of this class of T-type photomechanical crystals. The important role of steric interactions and *hh* packing in determining the ability to create a metastable photodimer in the crystal was confirmed and clarified. Careful examination of intermolecular bonding in a subset of fluorinated **9AC**s revealed an absence of H…F intermolecular bond formation and a lack of clear energy differences that could explain observed trends in the dissociation kinetics and mechanical reset times. Instead, it appears that differences between molecules reflect variations in cooperative phenomena that give rise to highly nonlinear (concentration dependent) kinetics. It is possible that such kinetics are especially

pronounced in the **9AC** series due to the presence of strong intermolecular COOH bonds. With a more detailed understanding, it may be possible to design molecular structures that optimize intermolecular interactions to amplify or suppress such collective phenomena and create light-responsive crystals with novel properties.

4.7 Supporting Information

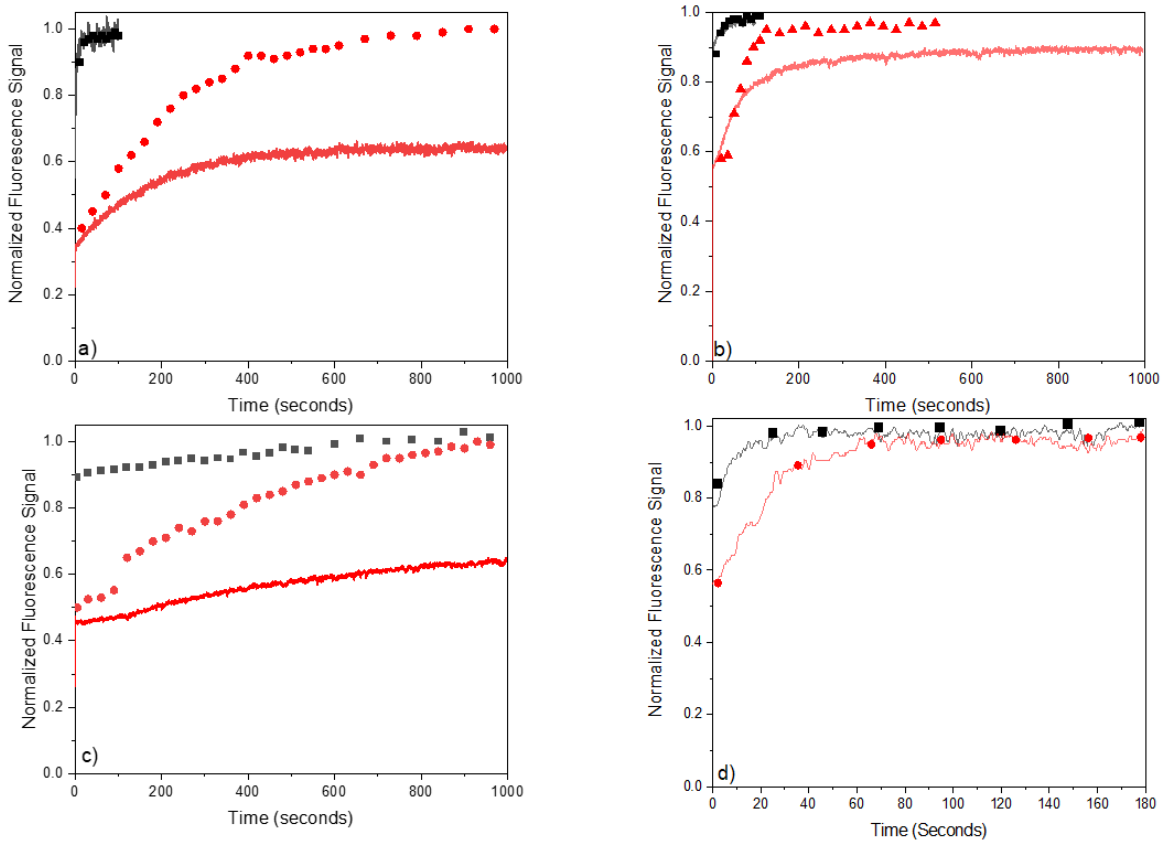

Figure S4.10: Fluorescence recovery data on long timescales for compounds: **a) 9AC**, **b) 2F-9AC**, **c) 10F-9AC**, and **d) 2,6-diF-9AC**. Red points are for ~50% photoconversion, while black points are for ~10% photoconversion, all with intermittent probe. Continuous lines show data for continuous probe exposure, which tends to slow down the recovery for large photoconversions.

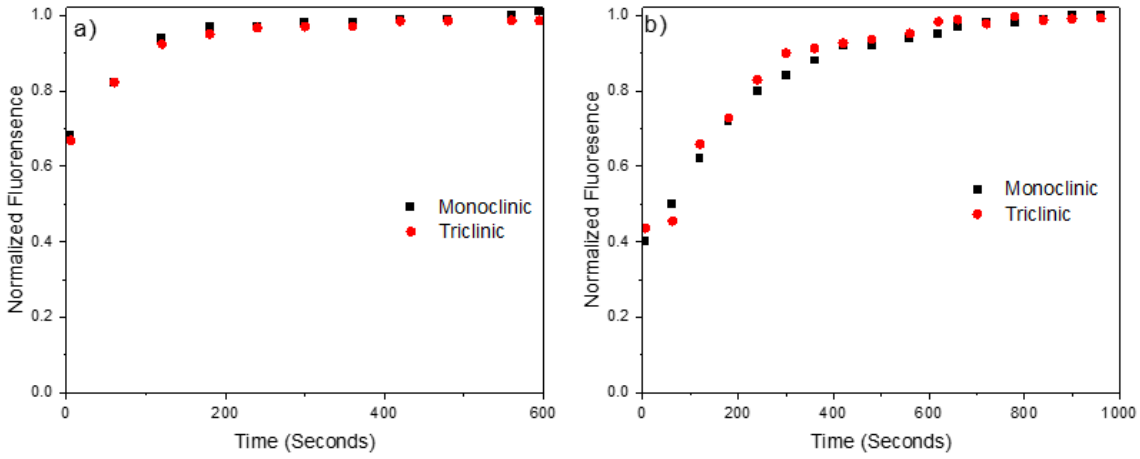

Figure S4.11: The fluorescence recoveries of monoclinic and triclinic **9AC** polymorphs are effectively identical for both **a)** 30% photodimerization and **b)** 60% photodimerization. Note the different time axes.

4.7.1 S3: Synthesis of 4,5diF-9AC, 2Cl-9AC, 4Cl-9AC, 4,5diCl-9AC

Materials: 9-Anthracene carboxylic acid (9AC, 99%), 1-Chloroanthracene (95%), Cesium Fluoride (99%, anhydrous), Zinc (99.9%, powder), Lithium (99%, ribbon), and 1-Bromobutane (99%), and n-Butyllithium (2.5 M hexanes) were purchased from Merck Sigma-Aldrich and used without further purification. 1,8-Dichloroanthraquinone (95% GC) was purchased from TCI-America and used without further purification. 2-Chloroanthracene was purchased from Santa Cruz Biotechnology and used without further purification. Dry diethyl ether (Et_2O) was prepared by distillation over $LiAlH_4$ and stored over activated molecular sieves (4 Å). All other organic solvents were distilled over CaH_2 and stored over activated molecular sieves (4 Å). Glassware were kept dry in an oven at 60 °C prior to use. Equipment: Melting points were determined using a Stuart Melting Point SMP30 with sealed capillary tubes

Synthesis of 4,5-Difluoroanthracene-9-carboxylic acid (4,5diF-9AC): Synthetic Figure 4.12 was followed

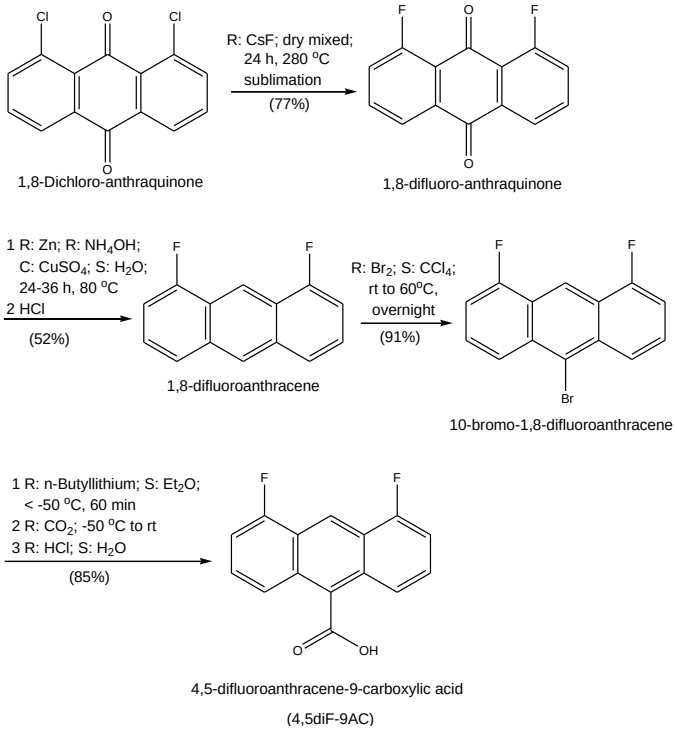

Figure S4.12: The synthesis of 4,5diF-9AC

Synthesis of 1,8-Difluoro-anthraquinone: The use of dry CsF is crucial for the chemical yield and purity of 1,8-Difluoro-anthraquinone. CsF (4 g, 26 mmole) was placed in a Schlenk tube (25 ml) and heated to 200 ^{o}C for two hours under vacuum (5 mbar). The anhydrous CsF was cooled to room temperature under a blanket of Argon gas. 1,8-Dichloroanthraquinone (1.1 g, 4 mmoles) was mixed thoroughly with the anhydrous CsF using a mortar and pestle while gently purging the mixture under a stream of Argon gas. The dry mixture was transferred into a small 50 ml tall form beaker, sealed with aluminum foil and placed over a hot plate set at 280 ^{o}C for 15 hours. 1,8-Difluoro-anthraquinone sublimes and deposits in the form of yellow needle crystals on the walls of the beaker.

Obtained yellow crystalline needles (0.6g, 62% yield) with a mp of 227-229 °C (literature mp: 228 °C) [66]. ^{1}H NMR (400 MHz, DMSO-d_6) δ (ppm): 8.03 (2H, dd, J = 7.8 Hz, 0.9Hz), 7.79 (2H, ddd, J_{H-F} = 4.6 Hz, J = 7.8 Hz, 8.2 Hz), 7.54 (2H, ddd, J_{H-F} = 11 Hz, 8.2 Hz, 0.9 Hz).

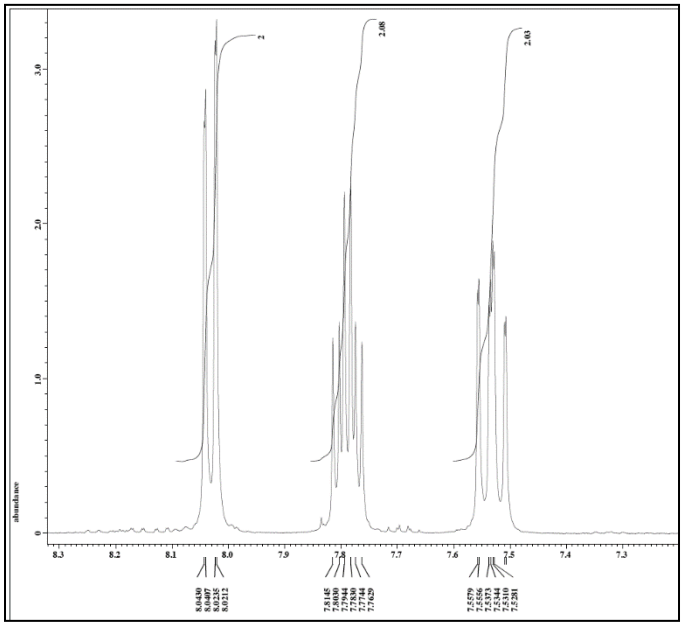

Figure S4.13: ^{1}H NMR of 1,8-Difluoroanthraquinone in 10% DMSO-d_6 in CCl_4

Synthesis of 1,8-Difluoroanthracene: Into a 100 mL round-bottom flask was suspended 1,8-Difluoro-anthraquinone (0.4 g, 1.6 mmoles) in 27% NH_4OH solution (10 mL), water (10 mL). Zinc powder (1.1 g, 17 mmoles), prewashed with dilute hydrochloric acid and dried, was added to the mixture along with catalytic amount of $CuSO_4$ (0.05 g) and stirred vigorously at 80 °C. The flask was fitted with an air-cooled Snyder column that allows excess ammonia gas to escape while stopping air from flowing back inside the flask. The reaction changes from deep red to a gray after 24 to 36 h or when all the 1,8-Difluoro-anthraquinone is reduced to the corresponding 1,8-Difluoroanthracene. The progress of the

reaction was monitored by TLC using Ethyl acetate: Hexanes (1:4) as mobile phase. The reaction mixture was cooled to room temperature and concentrated HCl solution was slowly added till all the excess Zn and ZnO dissolve and the solution becomes acidic. The product was extracted with ethyl acetate (40 ml) followed by washing the organic phase with brine and drying using anhydrous $MgSO_4$. The organic phase was decanted and the solvent removed under reduced pressure to obtain light yellow crude solid. Recrystallization from boiling ethanol/ water offers pale-yellow crystals (0.18 g, 52% yield) mp of 140-142 °C (literature mp: 142°C[67]). ^{1}H NMR (400 MHz, DMSO-d_6) δ (ppm): 8.83 (1H, s), 8.49 (1H, s), 7.78 (2H, d, J_{H-F} = 8.5 Hz), 7.40 (2H, dd, J_{H-F} = 7.8 Hz, 2.3Hz), 7.1 (2H, dd, J_{H-F} = 10.5 Hz, 7.3 Hz)

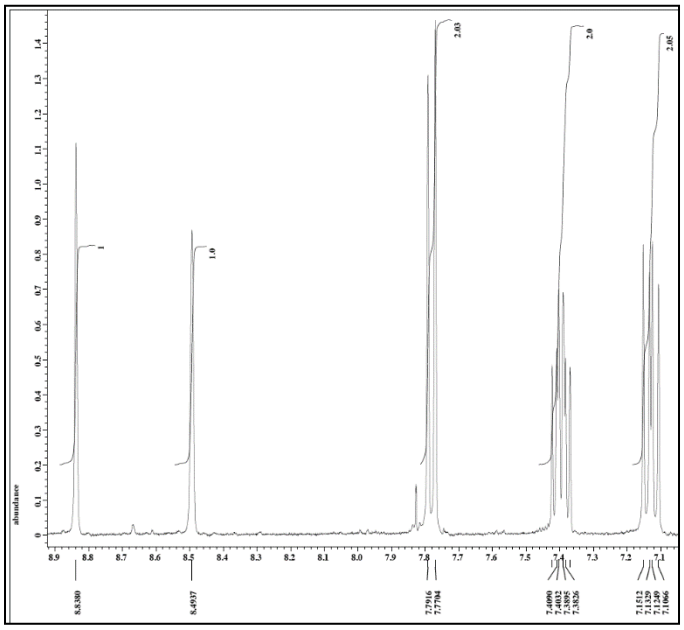

Figure S4.14: ^{1}H NMR of 1,8-Difluoroanthracene in 10% DMSO-d_6 in CCl_4

Synthesis of 10-Bromo-1,8-Difluoroanthracene: Bromine (0.18 g, 1.1 mmoles) was dissolved in CCl_4 (5 ml) and added slowly to a solution of 1,8-Difluoroanthracene (0.12 g, 0.56 mmoles) in CCl_4 (5 ml). The mixture was stirred at room temperature for 2 hours

followed by overnight stirring at 60 ^{o}C. The reaction mixture was passed through a silica gel plug (5 g, flash chromatography grade) and eluted with hexanes. The organic solvent was removed under reduced pressure to obtain yellow crystals of 10-Bromo-1,8-Difluoroanthracene (0.15 g, 91% yield) with a mp of 134-136 °C (recrystallized from Ethanol/ water). ^{1}H NMR (400 MHz, DMSO-d_6) δ (ppm): 8.92 (1H, s), 8.24 (2H, d, J_{H-F} = 9.2 Hz), 7.56 (2H, ddd, J_{H-F} = 5.6 Hz, 9.2 Hz, 7.6 Hz), 7.22 (2H, dd, J_{H-F} = 10 Hz, 7.6 Hz).

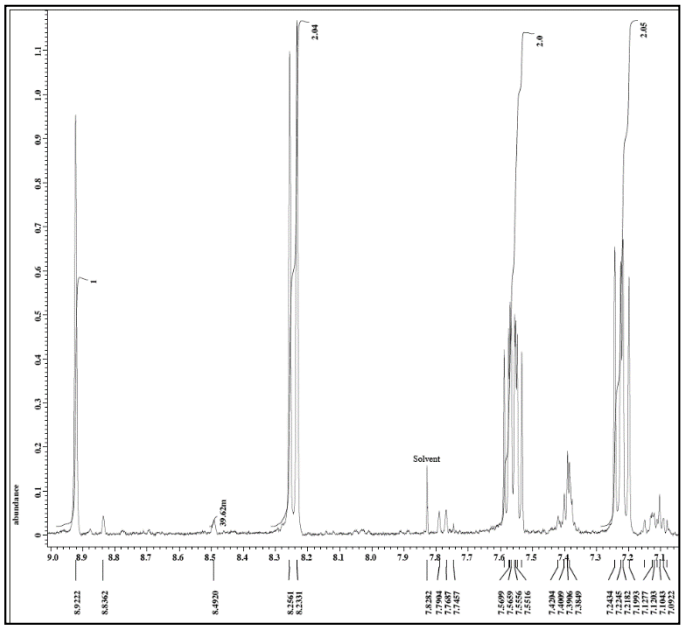

Figure S4.15: ^{1}H NMR of 10-Bromo-1,8-Difluoroanthracene in DMSO-d_6

Synthesis of 4,5-Difluoroanthracene-9-Carboxylic acid (4,5diF-9AC): In a 50 mL oven dried Schlenk flask, 10-Bromo-1,8-Difluoroanthracene (0.2 g, 0.73 mmoles) was dissolved in dry diethyl ether (20 ml) and cooled to < -50 ^{o}C using previously cooled Lab Armor dry bath beads. n-Butyllithium (2.5 molar in hexane, 0.32 ml, 1.1 equivalent) was added to the solution and allowed to react for 1 hour while maintaining the temperature < -50 ^{o}C. Dry

CO_2 gas was bubbled for 20 minutes while the reaction was allowed to slowly warm to room temperature. The reaction mixture was quenched by adding it to crushed ice (50 ml) followed by extracting the aqueous phase with ethyl acetate (50 ml) followed by hexanes (2 x 50 ml). The carboxylic acid was precipitated out of the aqueous phase by adding concentrated HCl (3 ml) to offer a yellow precipitate of crude 4,5diF-9AC that was suction filtered and recrystallized from boiling ethanol (10 ml) and water (10 ml). Obtained a yellow crystalline powder (0.22 g, 85% yield) with a mp of 274-275 °C . ^{1}H NMR (400 MHz, Acetone-d_6) δ (ppm): 8.97 (H, s), 8.01 (2H, d, J_{H-F} = 8.9 Hz), 7.64 (2H, ddd, J_{H-F} = 5.8 Hz, 8.9 Hz, 7.3 Hz), 7.37 (2H, dd, J_{H-F} = 10.8 Hz, 7.3 Hz). ^{13}C NMR (100 MHz, Acetone-d_6) δ (ppm): 168.77 (C=O), 159.92-157.40 (C-F, J = 252 Hz), 129.88, 129.30, 127.55-127.47 (C-C-C-F, J = 8 Hz), 122.19, 121.61-121.57 (J = 4 Hz), 114.35, 108.96-108.77 (C-C-F, J = 20 Hz).

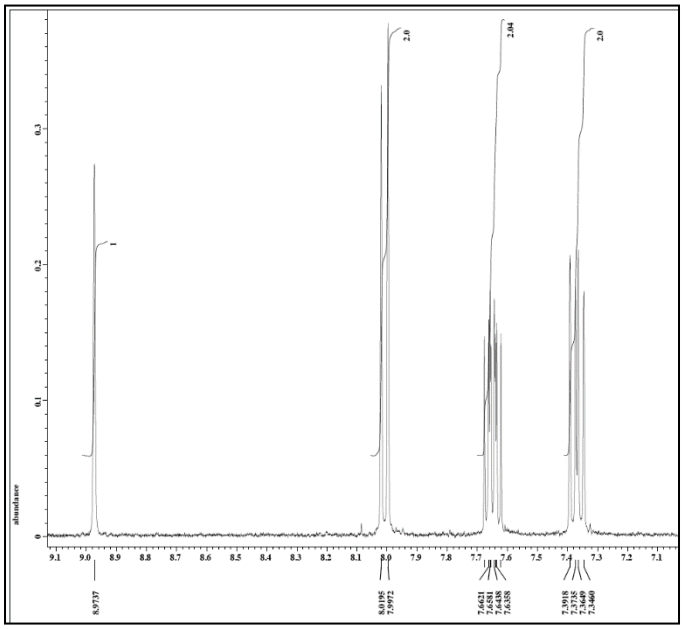

Figure S4.16: ^{1}H NMR of 4,5-Difluoroanthracene-9-Carboxylic acid in Acetone-d_6

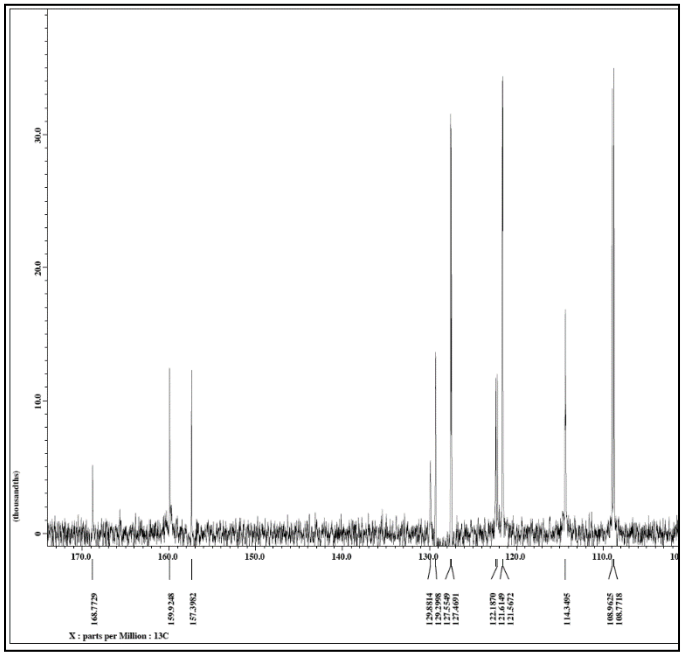

Figure S4.17: ^{13}C NMR of 4,5-Difluoroanthracene-9-Carboxylic acid in Acetone-d_6

Synthesis of 2-Chloroanthracene-9-carboxylic acid (2Cl-9AC): Synthetic Figure S4.18 was followed

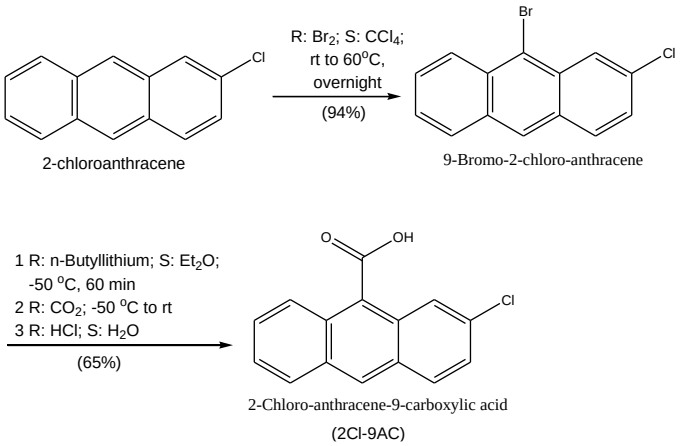

Figure S4.18: The synthesis of 2Cl-9AC

Synthesis of 9-Bromo-2-chloro-anthracene: Bromine (0.15 g, 0.56 mmoles, 1 eq.) was dissolved in CCl_4 (5 ml) and added slowly over a period of 10 min to a solution of 2-Chloroanthracene (0.2 g, 0.56 mmoles, 1 eq.) in CCl_4 (40 ml). The mixture was stirred at

room temperature for 2 hours followed by overnight stirring at 60 ºC. The reaction mixture was passed through a silica gel plug (5 g, flash chromatography grade) and eluted with hexanes. The organic solvent was removed under reduced pressure to obtain relatively pure yellow crystals of 9-Bromo-2-chloro-anthracene (0.26 g, 94% yield). A small quantity was recrystallized from acetic acid to give yellow crystals with mp of 138.5-141 °C (literature mp: 139-140 °C)[68]. ^{1}H NMR (400 MHz, DMSO-d_6) δ (ppm): 8.50 (1H, s), 8.43 (2H, d, J = 8.9 Hz), 8.02 (2H, dd, J = 3.4 Hz, 8.9 Hz), 7.61 (1H, ddd, J = 0.9 Hz, 1.4 Hz, 6.8 Hz), 7.52 (1H, ddd, J = 1.4 Hz, 1,1 Hz, 8.2 Hz), 7.41 (1H, dd, J = 1.8 Hz, 9.1 Hz)

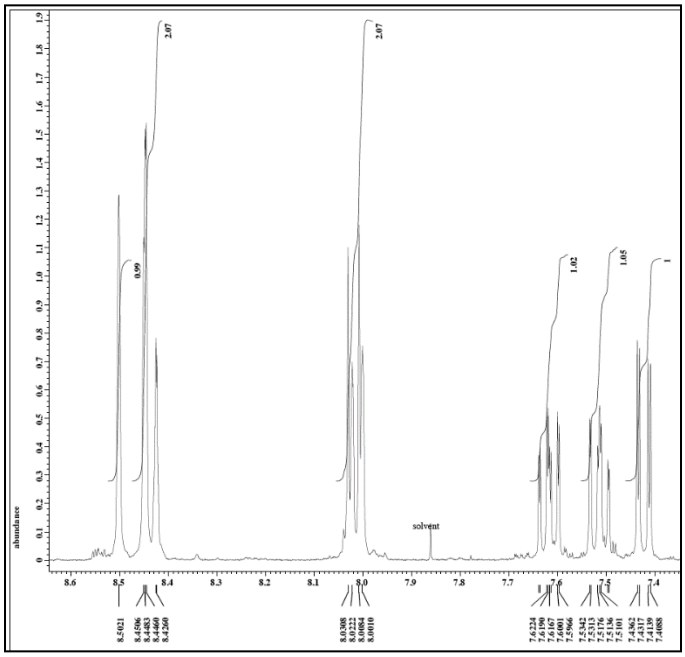

Figure S4.19: ^{1}H NMR of 9-Bromo-2-chloro-anthracene in DMSO-d_6

Synthesis of 2-Chloro-anthracene-9-carboxylic acid (2Cl-9AC): In a 50 mL oven dried Schlenk flask, 9-Bromo-2-chloro-anthracene (0.23 g, 0.78 mmoles) was dissolved in dry diethyl ether (20 ml) and cooled to -50 ºC using previously cooled Lab Armor dry bath

beads. n-Butyllithium (2.5 molar in hexane, 0.31 ml, 1.0 equivalent) was added to the solution and allowed to react for 1 hour while maintaining the temperature < -50 ^{o}C. Dry CO_2 gas was bubbled for 20 minutes while the reaction was allowed to slowly warm to room temperature. The reaction mixture was quenched by adding it to crushed ice (50 ml) followed by extracting the aqueous phase with ethyl acetate (50 ml) followed by hexanes (2 x 50 ml). The carboxylic acid was precipitated out of the aqueous phase by adding concentrated HCl (3 ml) to offer a yellow precipitate of crude 2Cl-9AC that was suction filtered and recrystallized from boiling ethanol/ water. Obtained a yellow crystalline powder (0.13 g, 65% yield) with a mp of 226-228 °C . ^{1}H NMR (400 MHz, DMSO-d_6) δ (ppm): 8.77 (1H, s), 8.20 (1H, d, J = 9.6 Hz), 8.14 (1 H, d, J = 8.9 Hz), 8.03 (1H dd, J = 1.1 Hz, 0.9 Hz), 7.61 (3H, m). ^{13}C NMR (100 MHz, DMSO-d_6) δ (ppm): 170.12 (C=O), 132.44, 131.72, 131.29, 129.70, 129.32, 129.18, 128.45, 128.26, 127.69, 126.97, 126.71, 125.45, 123.49

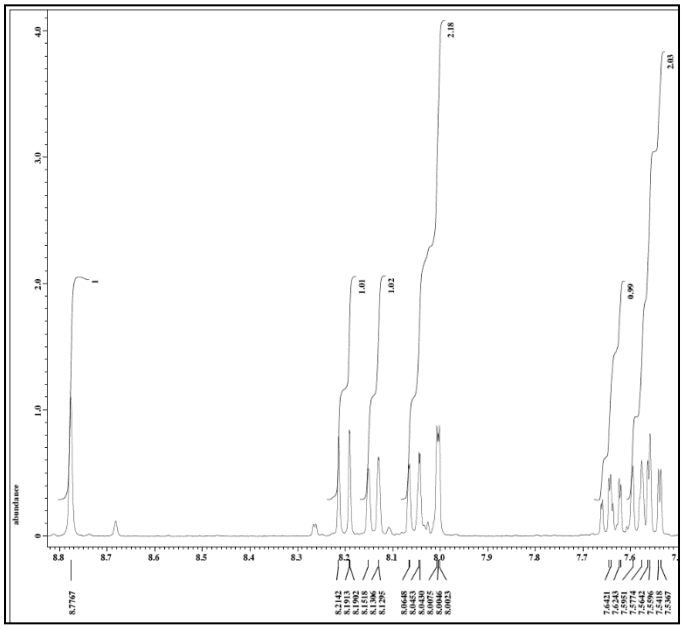

Figure S4.20: ^{1}H NMR 2-Chloro-anthracene-9-carboxylic acid in DMSO-d_6

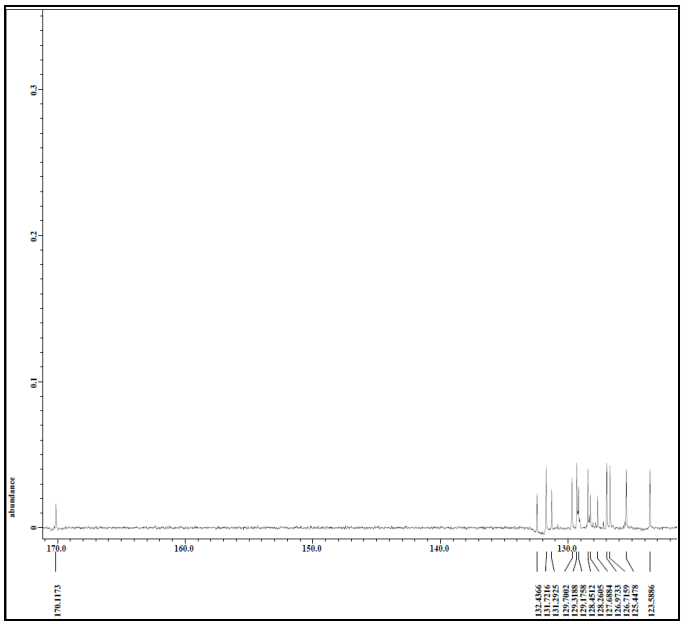

Figure S4.21: ^{13}C NMR 2-Chloro-anthracene-9-carboxylic acid in DMSO-d_6

Synthesis of 4-Chloroanthracene-9-carboxylic acid (4Cl-9AC): Synthetic Figure S4.22 was followed

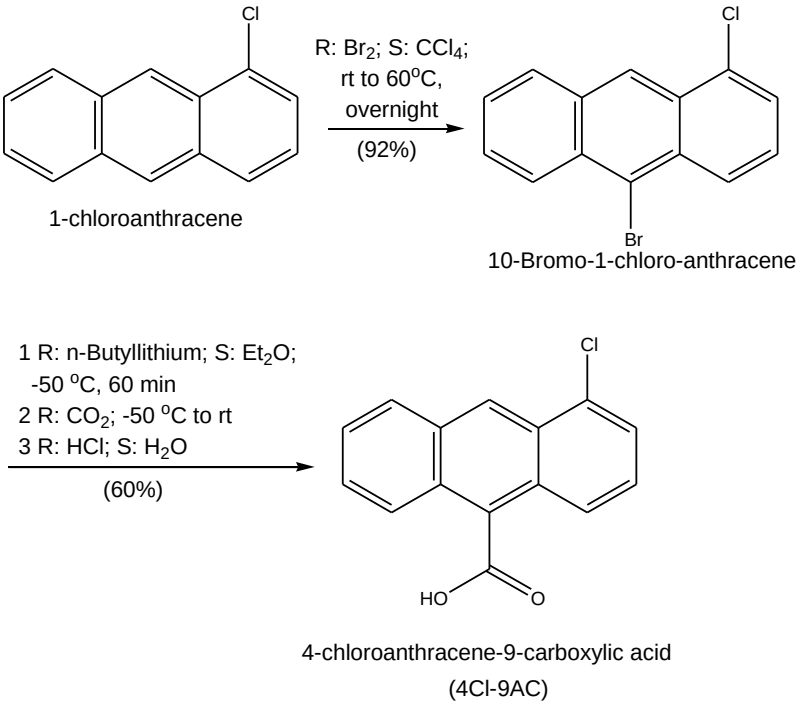

Figure S4.22: The synthesis of 4Cl-9AC

Synthesis of 10-Bromo-1-chloro-anthracene: Synthesis of this compound was done using a procedure similar to the one used for the synthesis of Synthesis of 9-Bromo-2-chloro-anthracene. Obtained yellow crystals (92% yield) with a mp = 132-134 ^{o}C. ^{1}H NMR (DMSO-d_6) δ (ppm): 8.95 (1H, s), 8.39 (2H, dd, J= 8.9 Hz, 0.7 Hz), 8.29 (1H, dd, J = 0.7 Hz, 9.1 Hz), 7.77 (2H), 7.63 (2H, m)

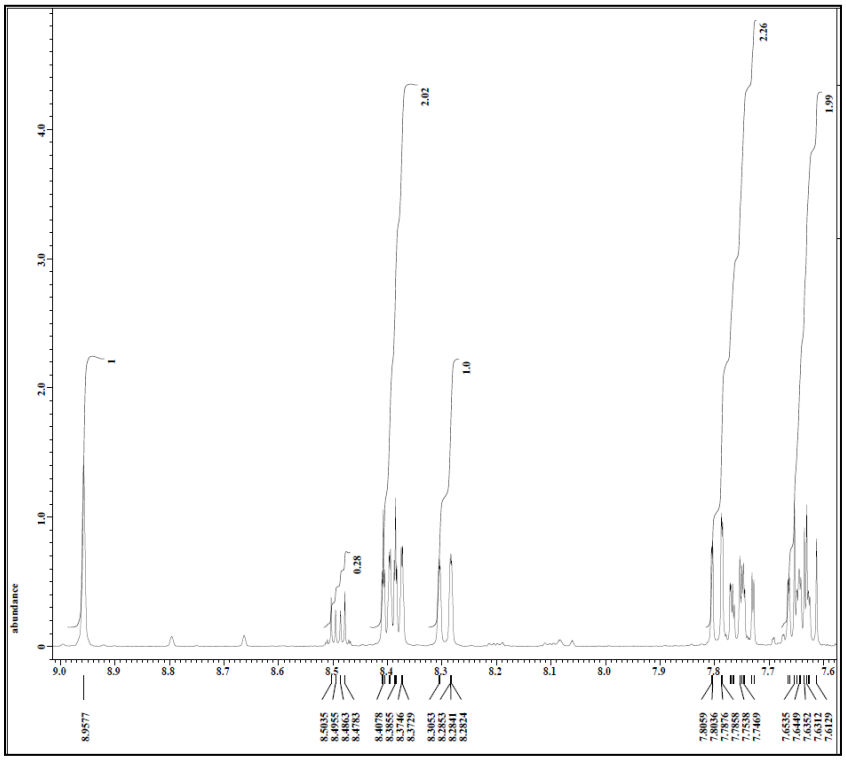

Figure S4.23: ^{1}H NMR 10-Bromo-1-chloro-anthracene in DMSO-d6

Synthesis of 4-Chloro-anthracene-9-carboxylic acid (4Cl-9AC): Synthesis of this compound was done using a procedure similar to the one used for the synthesis of Synthesis of 2-Chloro-anthracene-9-carboxylic acid. Obtained yellow crystals (60% yield) with a mp = 256 ^{o}C with decomposition (Literature mp = 258 ^{o}C[69]). ^{1}H NMR (400 MHz, DMSO-d_6) δ (ppm): 8.97 (1H, s), 8.30 (1H, d, J = 8.2 Hz), 8.09 (2H, dd, J = 1.4 Hz, 8.9 Hz), 7.76 (1H, dd, J = 0.7 Hz, 7.1 Hz), 7.63 (2H, m), 7.55 (1H, dd, J = 8.9 Hz, 7.3 Hz). ^{13}C NMR

(100 MHz, DMSO-d_6) δ (ppm): 170.33 (C=O), 131.73, 131.61, 129.66, 128.76, 128.57, 128.08, 128.04, 127.75, 127.25, 127.16, 126.57, 126.22, 125.31, 125.26

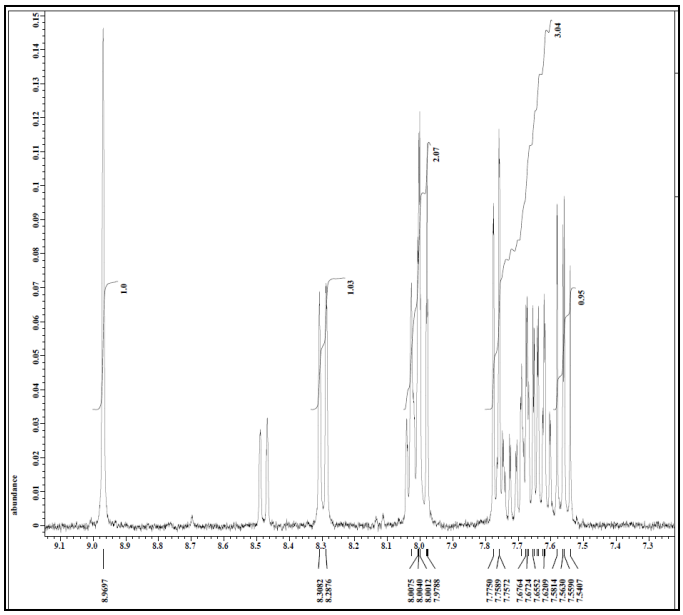

Figure S4.24: ^{1}H NMR 4-Chloro-anthracene-9-carboxylic acid in DMSO-d6

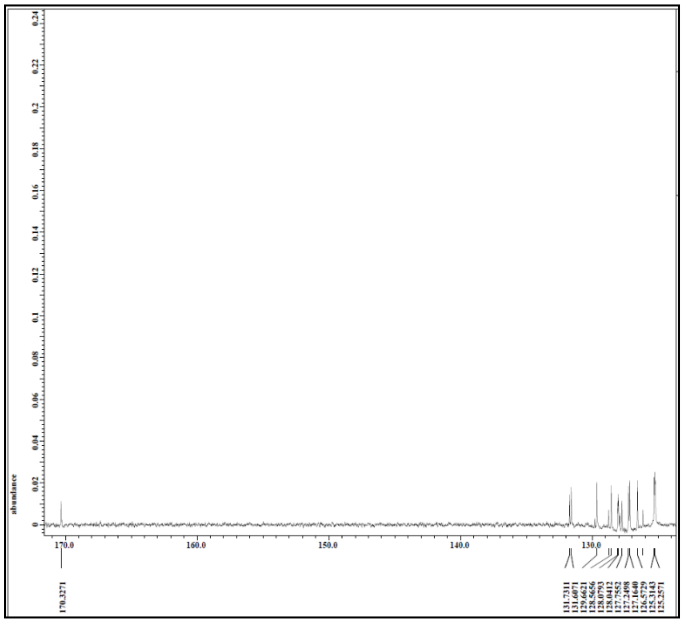

Figure S4.25: ^{13}C NMR 4-Chloro-anthracene-9-carboxylic acid in DMSO-d6

Synthesis of 4,5-dichloroanthracene-9-carboxylic acid (4,5diCl-9AC): Synthetic Scheme 4 was followed

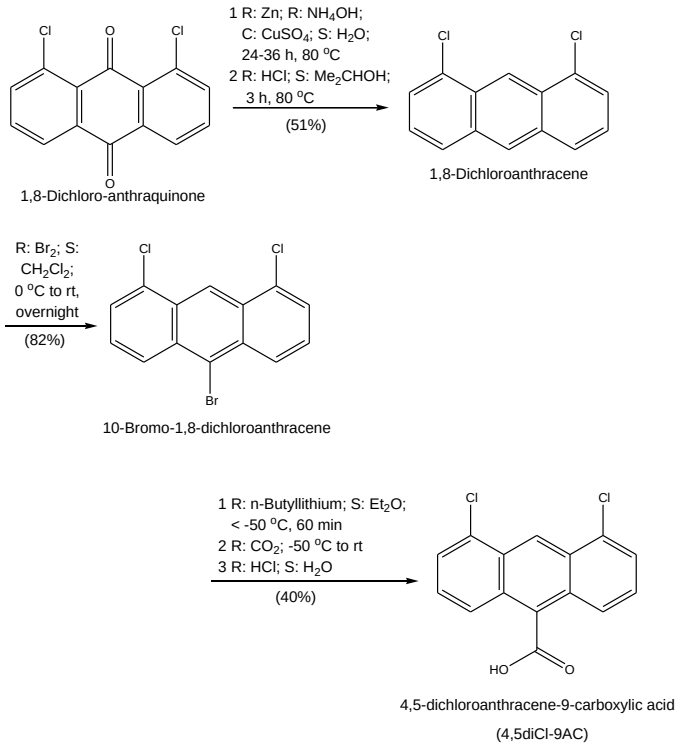

Figure S4.26: The synthesis of 4,5diCl-9AC

Synthesis of 1,8-Dichloroanthracene: Synthesis of this compound was done following the literature procedure[70]. Obtained yellow needles (51% yield) with a mp = 157-158 °C (Lit. 156.5-158 °C[5]). ^{1}H NMR (400 MHz, DMSO-d_6) δ (ppm): 9.17 (1H, s), 8.54 (1H, s), 7.97 (2H, d, J = 8.5 Hz), 7.62 (2H, d, J = 7.3 Hz), 7.43 (2H, dd, J = 7.1 Hz, 8.5 Hz)

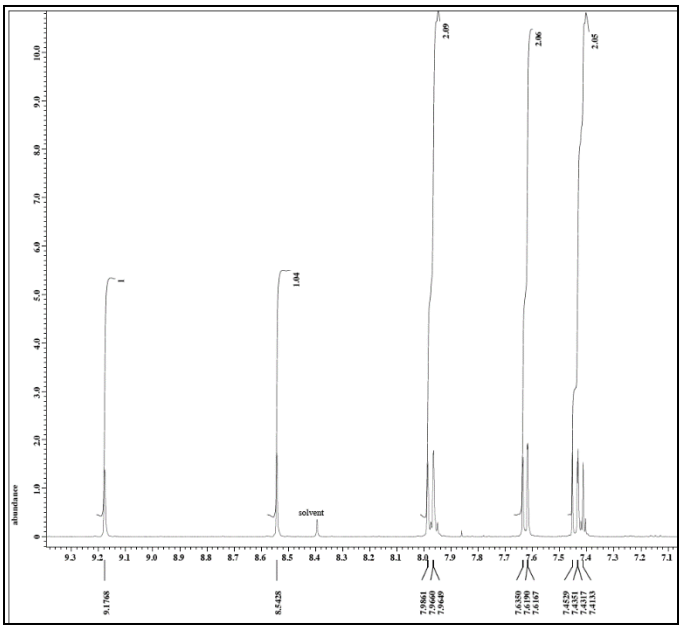

Figure S4.27: ^{1}H NMR 1,8-Dichloroanthracene in DMSO-d_6

Synthesis of 10-Bromo-1,8-dichloroanthracene: Synthesis of this compound was done following the literature procedure[71]. Obtained yellow crystals (82% yield) with a mp = 199-201 ^{o}C. ^{1}H NMR (DMSO-d_6) δ (ppm): 9.32 (1H, s), 8.46 (2H, dd, J = 8.9 Hz, 0.9 Hz), 7.71 (2H, d, J = 7.1 Hz), 7.58 (2H, dd, J = 7.3 Hz, 8.9 Hz)

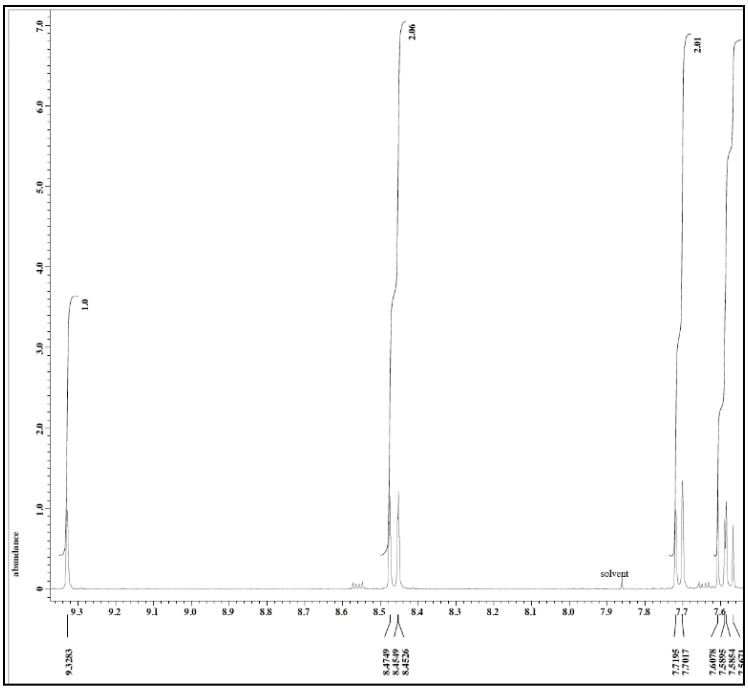

Figure S4.28: ^{1}H NMR 10-Bromo-1,8-dichloroanthracene in DMSO-d_6

Synthesis of 4,5-dichloroanthracene-9-carboxylic acid (4,5diCl-9AC): Synthesis of this compound was done using a procedure similar to the one used for the synthesis of Synthesis of 4-Chloro-anthracene-9-carboxylic acid. Obtained yellow crystals (40% yield) with a mp > 270 ^{o}C. ^{1}H NMR (400 MHz, DMSO-d_6) δ (ppm): 9.19 (1H, s), 8.02 (2H, ddd, *J* = 0.9 Hz, 1.8 Hz, 8.9 Hz), 7.87 (2H, d, J = 6.6 Hz), 7.65 (2H, dd, J = 7.2 Hz, 8.7 Hz). ^{13}C NMR (100 MHz, DMSO-d_6) δ (ppm): 169.88 (C=O), 132.79, 131.87, 128.63, 128.47, 128.37, 127.60, 125.23, 121.36

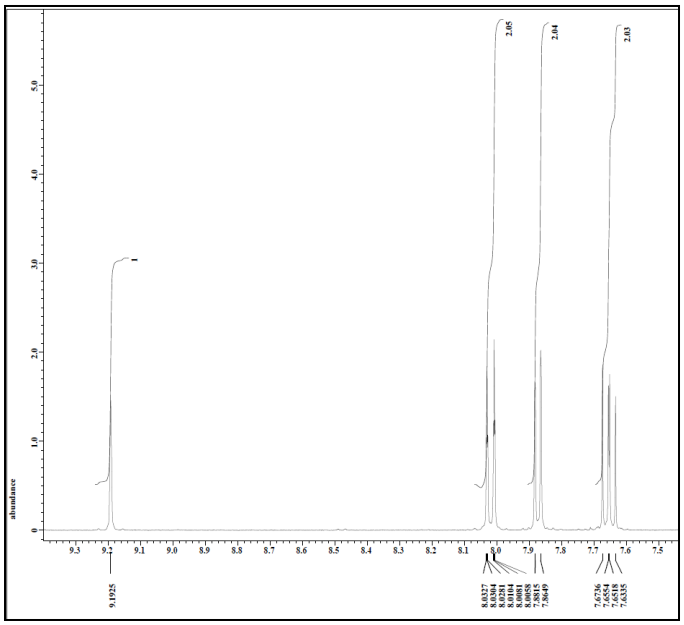

Figure S4.29: ^{1}H NMR 4,5-dichloroanthracene-9-carboxylic acid in DMSO-d_6

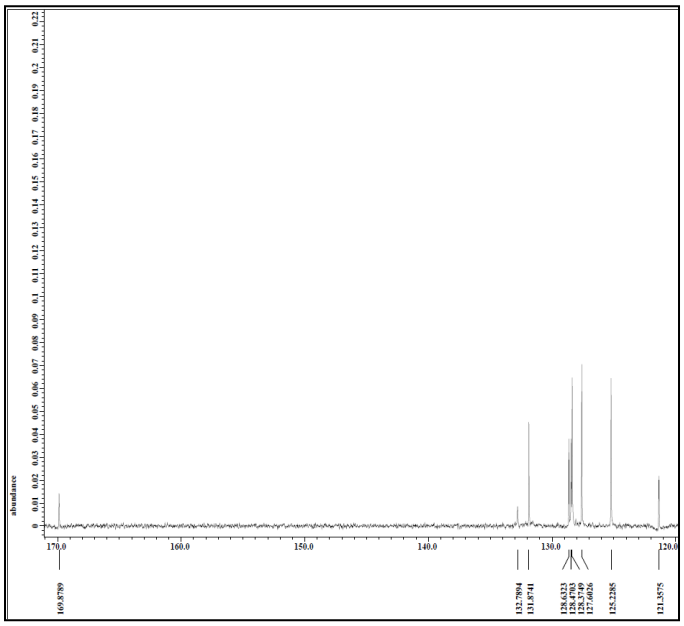

Figure S4.30: ^{13}C NMR 4,5-dichloroanthracene-9-carboxylic acid in DMSO-d_6

4.7.2 S4: Crystallographic information for 4,5diF-9AC:

Procedure:

A light-yellow thin needle fragment (0.475 x 0.032 x 0.010 mm^3) was used for the single crystal x-ray diffraction study of $C_{15}H_8F_2O_2$ (sample cb71_0m). The crystal was coated with paratone oil and mounted on to a cryo-loop glass fiber. X-ray intensity data were collected at 100(2) K on a Bruker APEX2[72] platform-CCD x-ray diffractometer system (fine focus Mo-radiation, λ = 0.71073 Å, 50KV/30mA power). The CCD detector was placed at a distance of 5.0600 cm from the crystal.

A total of 3600 frames were collected for a hemisphere of reflections (with scan width of 0.3^o in ω and ϕ, starting ω and 2θ angles of -30^o, and ϕ angles of 0^o, 90^o, 180^o, and 270^o for every 600 frames, and 1200 frames with ϕ-scan from 0^o-360^o, 180 sec/frame exposure time). The frames were integrated using the Bruker SAINT software package[73] and using a narrow-frame integration algorithm. Based on a monoclinic crystal system, the integrated frames yielded a total of 13979 reflections at a maximum 2θ angle of 50.698^o (0.83 Å resolution), of which 1979 were independent reflections (R_{int} = 0.0976, R_{sig} = 0.0591, redundancy = 7.1, completeness = 100%) and 1318 (66.6%) reflections were greater than $2\sigma(I)$. The unit cell parameters were, **a** = 3.7462(11) Å, **b** = 9.5568(27) Å, **c** = 29.9042(84) Å, β = $90.3574(47)^o$, V = 1072.6(5) $Å^3$, Z = 4, calculated density D_c = 1.602 g/cm^3. Absorption corrections were applied (absorption coefficient μ = 0.129 mm^{-1}; min/max transmission = 0.941/0.999) to the raw intensity data using the SADABS program[74].

The Bruker SHELXTL software package[75] was used for phase determination and structure

refinement. The distribution of intensities (E^2-1 = 1.006) and systematic absent reflections indicated one possible space group, P2(1)/n. The space group P2(1)/n (#14) was later determined to be correct. Direct methods of phase determination followed by two Fourier cycles of refinement led to an electron density map from which most of the non-hydrogen atoms were identified in the asymmetric unit of the unit cell. With subsequent isotropic refinement, all of the non-hydrogen atoms were identified. There was one molecule of $C_{15}H_8F_2O_2$ present in the asymmetric unit of the unit cell. The intermolecular hydrogen bond distances and angles are given in the crystal structure refinement section.

Atomic coordinates, isotropic and anisotropic displacement parameters of all the non-hydrogen atoms were refined by means of a full matrix least-squares procedure on F^2. The H-atoms were included in the refinement in calculated positions riding on the atoms to which they were attached, except the OH hydrogen atom involved in intermolecular hydrogen bonding was refined unrestrained. The refinement converged at R1 = 0.0478, wR2 = 0.1117, with intensity I>2s (I). The largest peak/hole in the final difference map was 0.283/-0.334 e/$Å^3$.

Crystal data and structure refinement for 4,5diF-9AC.

Identification code	cb71_0m
Empirical formula	C15 H8 F2 O2
Formula weight	258.21
Temperature	100(2) K
Wavelength	0.71073 Å
Crystal system	Monoclinic

Space group	P 21/n	
Unit cell dimensions	a = 3.7462(11) Å	a= 90°.
	b = 9.557(3) Å	b= 90.357(5)°.
	c = 29.904(8) Å	g = 90°.
Volume	1070.6(5) $Å^3$	
Z	4	
Density (calculated)	1.602 Mg/m^3	
Absorption coefficient	0.129 mm^{-1}	
F(000)	528	
Crystal size	0.475 x 0.032 x 0.010 mm^3	
Theta range for data collection	1.362 to 25.349°.	
Index ranges	-4<=h<=4, -11<=k<=11, -36<=l<=36	
Reflections collected	13979	
Independent reflections	1979 [R(int) = 0.0976]	
Completeness to theta = 25.242°	100.0 %	
Absorption correction	Semi-empirical from equivalents	
Refinement method	Full-matrix least-squares on F^2	
Data / restraints / parameters	1979 / 0 / 173	
Goodness-of-fit on F^2	1.034	
Final R indices [I>2sigma(I)]	R1 = 0.0478, wR2 = 0.1117	
R indices (all data)	R1 = 0.0856, wR2 = 0.1273	
Extinction coefficient	n/a	

Largest diff. peak and hole 0.283 and -0.334 e.Å^{-3}

S5: Crystallographic information for **4,5diCl-9AC**:

Procedure:

A light-yellow thin needle fragment (0.500 x 0.042 x 0.032 mm^3) was used for the single crystal x-ray diffraction study of $C_{15}H_8Cl_2O_2$ (sample cb72_0m). The crystal was coated with paratone oil and mounted on to a cryo-loop glass fiber. X-ray intensity data were collected at 100(2) K on a Bruker APEX2[72] platform-CCD x-ray diffractometer system (fine focus Mo-radiation, l = 0.71073 Å, 50KV/30mA power). The CCD detector was placed at a distance of 5.0600 cm from the crystal.

A total of 4800 frames were collected for a sphere of reflections (with scan width of 0.3^o in w and f, starting w and 2q angles of –30^o, and f angles of 0^o, 90^o, 120^o, 180^o, 240^o, and 270^o for every 600 frames, and 1200 frames with f-scan from 0^o-360^o, 60 sec/frame exposure time). The frames were integrated using the Bruker SAINT software package[73] and using a narrow-frame integration algorithm. Based on a monoclinic crystal system, the integrated frames yielded a total of 30670 reflections at a maximum 2q angle of 60.068^o (0.71 Å resolution), of which 3482 were independent reflections (R_{int} = 0.0692, R_{sig} = 0.0388, redundancy = 8.8, completeness = 100%) and 2910 (83.6%) reflections were greater than 2s(I). The unit cell parameters were, **a** = 18.665(2) Å, **b** = 3.8338(4) Å, **c** = 33.213(4) Å, **b** = 95.3374(17)^o**,** V = 2366.4(4) Å^3, Z = 8, calculated density D_c = 1.621 g/cm^3. Absorption corrections were applied (absorption coefficient m = 0.524 mm^{-1}; min/max transmission = 0.779/0.983) to the raw intensity data using the SADABS program[74].

The Bruker SHELXTL software package[75] was used for phase determination and structure refinement. The distribution of intensities (E^2-1 = 1.001) and systematic absent reflections indicated one possible space group, C2/c. The space group C2/c (#15) was later determined to be correct. Direct methods of phase determination followed by two Fourier cycles of refinement led to an electron density map from which most of the non-hydrogen atoms were identified in the asymmetric unit of the unit cell. With subsequent isotropic refinement, all of the non-hydrogen atoms were identified. There was one disordered molecule of $C_{15}H_8Cl_2O_2$ present in the asymmetric unit of the unit cell. The Cl-atoms bonded to C4 and C5 were modeled with disordered. The disordered Cl/H site occupancy ratio was 96%/4%. The intermolecular hydrogen bond distances and angle are given in crystal data and structure section.

Atomic coordinates, isotropic and anisotropic displacement parameters of all the non-hydrogen atoms were refined by means of a full matrix least-squares procedure on F^2. The H-atoms were included in the refinement in calculated positions riding on the atoms to which they were attached, except the OH hydrogen atom involved in intermolecular hydrogen bonding was refined unrestrained. The refinement converged at R1 = 0.0443, wR2 = 0.1126, with intensity I>2s (I). The largest peak/hole in the final difference map was 0.938/-0.389 e/$Å^3$.

Crystal data and structure refinement for 4,5diCl-9AC.

Identification code	4,5diCl-9AC
Empirical formula	C15 H8.07 Cl1.93 O2
Formula weight	288.70

Temperature	100(2) K	
Wavelength	0.71073 Å	
Crystal system	Monoclinic	
Space group	C 2/c	
Unit cell dimensions	a = 18.665(2) Å	a= 90°.
	b = 3.8338(4) Å	b= 95.3374(17)°.
	c = 33.213(4) Å	g = 90°.
Volume	2366.4(4) $Å^3$	
Z	8	
Density (calculated)	1.621 Mg/m^3	
Absorption coefficient	0.524 mm^{-1}	
F(000)	1175	
Crystal size	0.500 x 0.042 x 0.032 mm^3	
Theta range for data collection	2.192 to 30.034°.	
Index ranges	-26<=h<=26, -5<=k<=5, -46<=l<=46	
Reflections collected	30670	
Independent reflections	3482 [R(int) = 0.0692]	
Completeness to theta = 25.242°	100.0 %	
Absorption correction	Semi-empirical from equivalents	
Refinement method	Full-matrix least-squares on F^2	
Data / restraints / parameters	3482 / 0 / 177	
Goodness-of-fit on F^2	1.066	

Final R indices [I>2sigma(I)]	R1 = 0.0443, wR2 = 0.1126
R indices (all data)	R1 = 0.0546, wR2 = 0.1199
Extinction coefficient	n/a
Largest diff. peak and hole	0.938 and -0.389 e.Å^{-3}

4.8 References

1. Kim, T.; Zhu, L.; Al-Kaysi, R. O.; Bardeen, C. J., Organic photomechanical materials. *ChemPhysChem* 2014, *15*, 400-414.

2. Naumov, P.; Chizhik, S.; Panda, M. K.; Nath, N. K.; Boldyreva, E., Mechanically Responsive Molecular Crystals. *Chem. Rev.* 2015, *115*, 12440-12490.

3. White, T. J., *Photomechanical Materials, Composites, and Systems*. 1 ed.; Wiley: Hoboken, New Jersey, 2017.

4. Naumov, P.; Kowalik, J.; Solntsev, K. M.; Baldridge, A.; Moon, J.-S.; Kranz, C.; Tolbert, L. M., Topochemistry and photomechanical effects in crystals of green fluorescent protein-like chromophores: effects of hydrogen bonding and crystal packing. *J. Am. Chem. Soc.* 2010, *132*, 5845-5857.

5. Kim, T.; Zhu, L.; Mueller, L. J.; Bardeen, C. J., Dependence of the solid-state photomechanical response of 4-chlorocinnamic acid on crystal shape and size. *CrystEngComm* 2012, *14*, 7792-7799.

6. Medishetty, R.; Husain, A.; Bai, Z.; Runceviski, T.; Dinnebier, R. E.; Naumov, P.; Vittal, J. J., Single crystals popping under UV light: a photosalient effect triggered by a [2+2] cycloaddition reaction. *Angew. Chem. Int. Ed.* 2014, *53*, 5907-5911.

7. Medishetty, R.; Sahoo, S. C.; Mulijanto, C. E.; Naumov, P.; Vittal, J. J., Photosalient Behavior of Photoreactive Crystals. *Chem. Mater.* 2015, *27*, 1821-1829.

8. Wang, H.; Chen, P.; Wu, Z.; Zhao, J.; Sun, J.; Lu, R., Bending, Curling, Rolling, and Salient Behavior of Molecular Crystals Driven by [2+2] Cycloaddition of a Styrylbenzoxazole Derivative. *Angew. Chem. Int. Ed.* 2017, *56*, 9463 –9467.

9. Samanta, R.; Ghosh, S.; Devarapalli, R.; Reddy, C. M., Visible Light Mediated Photopolymerization in Single Crystals: Photomechanical Bending and Thermomechanical Unbending. *Chem. Mater.* 2018, *30*, 577−581.

10. Samanta, R.; Kitagawa, D.; Mondal, A.; Bhattacharya, M.; Annadhasan, M.; Mondal, S.; Chandrasekar, R.; Kobatake, S.; Reddy, C. M., Mechanical Actuation and Patterning of Rewritable Crystalline Monomer−Polymer Heterostructures via Topochemical Polymerization in a Dual-Responsive Photochromic Organic Material. *ACS Appl. Mater.* 2020, *12*, 16856−16863.

11. Yadava, K.; Vittal, J. J., Photosalient Behavior of Photoreactive Zn(II) Complexes. *Cryst. Growth De.* 2019, *19*, 2542-2547.

12. Tong, F.; Xu, W.; Guo, T.; Lui, B. F.; Hayward, R. C.; Palffy-Muhoray, P.; Al-Kaysi, R. O.; Bardeen, C. J., Photomechanical molecular crystals and nanowire assemblies based on the [2+2] photodimerization of a phenylbutadiene derivative. *J. Mater. Chem. C* 2020, *8*, 5036-5044.

13. Al-Kaysi, R. O.; Muller, A. M.; Bardeen, C. J., Photochemically driven shape changes of crystalline organic nanorods. *J. Am. Chem. Soc.* 2006, *128*, 15938-15939.

14. Koshima, H.; Uchimoto, H.; Taniguchi, T.; Nakamura, J.; Asahi, T.; Asahi, T., Mechanical motion of molecular crystals induced by [4 + 4] photodimerisation. *Cryst. Eng. Comm.* 2016, *18*, 7305-7310.

15. Salzillo, T.; Brillante, A., Commenting on the Photoreactions of Anthracene Derivatives in the Solid Stte. *Cryst. Eng. Comm.* 2019, *21*, 3127–3136.

16. Tong, F.; Bardeen, C. J.; Al-Kaysi, R. O., Photomechanical Crystals Made from Anthracene Derivatives. In *Mechanically Responsive Materials for Soft Robotics*, Koshima, H., Ed. Wiley-VCH: Weinheim, Germany, 2020.

17. More, R.; Scholz, M.; Busse, G.; Busse, L.; Paulmann, C.; Tolkiehn, M.; Techert, S., Hydrogen Bond Dynamics in Crystalline b-9-Anthracene Carboxylic Acid -- a Combined Crystallographic and Spectroscopic Study. *Phys. Chem. Chem. Phys.* 2012, *14*, 10187-10195.

18. Ito, Y.; Fujita, H., Formation of an unstable photodimer from 9-anthracenecarboxylic acid in the solid state. *J. Org. Chem.* 1996, *61*, 5677-5680.

19. Al-Kaysi, R. O.; Bardeen, C. J., Reversible photoinduced shape changes of crystalline organic nanorods. *Adv. Mater.* 2007, *19*, 1276-1280.

20. Zhu, L.; Al-Kaysi, R. O.; Bardeen, C. J., Reversible photoinduced twisting of molecular crystal microribbons. *J. Am. Chem. Soc.* 2011, *133*, 12569-12575.

21. More, R.; Busse, G.; Hallmann, J.; Paulmann, C.; Scholz, M.; Techert, S., Photodimerization of crystalline 9-anthracenecarboxylic acid: a nontopotactic autocatalytic transformation. *J. Phys. Chem. C* 2010, *114*, 4142-4148.

22. Zhu, L.; Al-Kaysi, R. O.; Dillon, R. J.; Tham, F. S.; Bardeen, C. J., Crystal structures and photophysical properties of 9-anthracene carboxylic acid derivatives for photomechanical applications. *Cryst. Growth Des.* 2011, *11*, 4975-4983.

23. Zhu, L.; Tong, F.; Salinas, C.; Al-Muhanna, M. K.; Tham, F. S.; Kisailus, D.; Al-Kaysi, R. O.; Bardeen, C. J., Improved Solid-State Photomechanical Materials by

Fluorine Substitution of 9-Anthracene Carboxylic Acid. *Chem. Mater.* 2014, *26,* 6007–6015.

24. Řezáč, J.; Greenwell, C.; Beran, G. J. O., Accurate Noncovalent Interactions via Dispersion-Corrected Second-Order Møller−Plesset Perturbation Theory. *J. Chem. Theory Comput.* 2018, *14*, 4711-4721.

25. Bell, R. P., The theory of reactions involving proton transfers. *Proc. Royal. Soc. A* 1936, *154*, 414-429.

26. Evans, M. G.; Polanyi, M., Inertia and driving force of chemical reactions. *Trans. Faraday Soc.* 1938, *34,* 11-24.

27. Pla, P.; Wang, Y.; Alcami, M., When is the Bell–Evans–Polanyi principle fulfilled in Diels–Alder reactions of fullerenes?†. *Phys. Chem. Chem. Phys.* 2020, *22*, 8846-8852.

28. Chen, Y.; Chang, K.-H.; Meng, F.-Y.; Tseng, S.-M.; Chou, P.-T., Broadening the Horizon of the Bell–Evans–Polanyi Principle towards Optically Triggered Structure Planarization. *Angew. Chem. Int. Ed.* 2021, *60*, 7205–7212.

29. Easley, C. J.; Tong, F.; Dong, X.; Al-Kaysi, R. O.; Bardeen, C. J., Using light intensity to control reaction kinetics and reversibility in photomechanical crystals. *Chem. Sci.* 2020, *11*, 9852–9862.

30. Becke, A. D., Density-fnnctional exchange-energy approximation with correct asymptotic behavior. *Phys. Rev. A* 1988, *38,* 3098-3100.

31. Lee, C.; Yang, W.; Parr, R. G., Development of the Colic-Salvetti correlation-energy formula into a functional of the electron density. *Phys. Rev. B* 1988, *37,* 785-789.

32. Grimme, S.; Antony, J.; Ehrlich, S.; Krieg, H., A consistent and accurate ab initio parametrization of density functional dispersion correction (DFT-D) for the 94 elements H-Pu. *J. Chem. Phys.* 2010, *132*, 154104.

33. Grimme, S.; Ehrlich, S.; Goerigk, L., Effect of the Damping Function in Dispersion Corrected Density Functional Theory. *J. Comp. Chem.* 2011, *32*, 1456-1465.

34. Weigenda, F.; Ahlrichs, R., Balanced basis sets of split valence, triple zeta valence and quadruple zeta valence quality for H to Rn: Design and assessment of accuracy. *Phys. Chem. Chem. Phys.* 2005, *7*, 3297-3305.

35. Chai, J.-D.; Head-Gordon, M., Systematic optimization of long-range corrected hybrid density functionals. *J. Chem. Phys.* 2008, *128*, 084106.

36. Jr., T. H. D., Gaussian basis sets for use in correlated molecular calculations. I. The atoms boron through neon and hydrogen. *J. Chem. Phys.* 1989, *90*, 1007-1023.

37. Ziegler, T.; Rauk, A.; Baerends, E. J., On the calculation of multiplet energies by the Hartree-Fock-Slater method. *Theor. Chim. Acta* 1977, *43*, 261–271.

38. Scalmani, G.; Frisch, M. J., Continuous surface charge polarizable continuum models of solvation. I. General formalism. *J. Chem. Phys.* 2010, *132*, 114110.

39. Grimme, S.; Diedrich, C.; Korth, M., The Importance of Inter- and Intramolecular van der Waals Interactions in Organic Reactions: the Dimerization of Anthracene Revisited. *Angew. Chem. Int. Ed.* 2006, *45*, 625-629.

40. Helgaker, T.; Klopper, W.; Koch, H.; Noga, J., Basis-set convergence of correlated calculations on water. *J. Chem. Phys.* 1997, *106*, 9639-9646.

41. Boys, S. F.; Bernardi, F., The calculation of small molecular interactions by the differences of separate total energies. Some procedures with reduced errors. *Molec. Phys.* 1970, *19*, 553-566.

42. M. J. Frisch, G. W. T., H. B. Schlegel, G. E. Scuseria, M. A. Robb, J. R. Cheeseman, G. Scalmani, V. Barone, G. A. Petersson, H. Nakatsuji, X. Li, M. Caricato, A. V. Marenich, J. Bloino, B. G. Janesko, R. Gomperts, B. Mennucci, H. P. Hratchian, J. V. Ortiz, A. F. Izmaylov, J. L. Sonnenberg, D. Williams-Young, F. Ding, F. Lipparini, F. Egidi, J. Goings, B. Peng, A. Petrone, T. Henderson, D. Ranasinghe, V. G. Zakrzewski, J. Gao, N. Rega, G. Zheng, W. Liang, M. Hada, M. Ehara, K. Toyota, R. Fukuda, J. Hasegawa, M. Ishida, T. Nakajima, Y. Honda, O. Kitao, H. Nakai, T. Vreven, K. Throssell, J. A. Montgomery, Jr., J. E. Peralta, F. Ogliaro, M. J. Bearpark, J. J. Heyd, E. N. Brothers, K. N. Kudin, V. N. Staroverov, T. A. Keith, R. Kobayashi, J. Normand, K. Raghavachari, A. P. Rendell, J. C. Burant, S. S. Iyengar, J. Tomasi, M. Cossi, J. M. Millam, M. Klene, C. Adamo, R. Cammi, J. W. Ochterski, R. L. Martin, K. Morokuma, O. Farkas, J. B. Foresman, and D. J. Fox *Gaussian 16, Revision C.01*, Gaussian, Inc: Wallingford CT, 2016.

43. Parrish, R. M.; Burns, L. A.; Smith, D. G. A.; Simmonett, A. C.; DePrince, A. E.; Hohenstein, E. G.; Bozkaya, U. u.; Sokolov, A. Y.; Remigio, R. D.; Richard, R. M.; Gonthier, J. r. m. F.; James, A. M.; McAlexander, H. R.; Kumar, A.; Saitow, M.; Wang, X.; Pritchard, B. P.; Verma, P.; Schaefer, H. F.; Patkowski, K.; King, R. A.; Valeev, E. F.; Evangelista, F. A.; Turney, J. M.; Crawford, T. D.; Sherrill, C. D., PSI4 1.1: An Open-Source Electronic Structure Program Emphasizing Automation, Advanced Libraries, and Interoperability. *J. Chem. Theory Comput.* 2017, *13*, 3185−3197.

44. Becke, A. D., On the large-gradient behavior of the density functional exchange energy. *J. Chem. Phys.* 1986, *85*, 7184-7187.

45. Perdew, J. P.; Burke, K.; Ernzerhof, M., Generalized Gradient Approximation Made Simple. *Phys. Rev. Lett.* 1996, *77*, 3865-3868.

46. Otero-de-la-Roza, A.; Johnson, E. R., Van der Waals interactions in solids using the exchange-hole dipole moment model. *J. Chem. Phys.* 2012, *136*, 174109.

47. Giannozzi, P.; Baroni, S.; Bonini, N.; Calandra, M.; Car, R.; Cavazzoni, C.; Ceresoli, D.; Chiarotti, G. L.; Cococcioni, M.; Dabo, I., QUANTUM ESPRESSO: a modular and open-source software project for quantum simulations of materials. *J. Phys.: Condens. Matter* 2009, *21*, 395502.

48. Giannozzi, P.; Andreussi, O.; Brumme, T.; Bunau, O.; Buongiorno, M.; Nardelli; Calandra, M.; Car, R.; Cavazzoni, C.; Ceresoli, D.; Cococcioni, M.; Colonna, N.; Carnimeo, I.; Corso, A. D.; Gironcoli, S. d.; Delugas, P.; Jr, R. A. D.; Ferretti, A.; Floris, A.; Fratesi, G.; Fugallo, G.; Gebauer, R.; Gerstmann, U.; Giustino, F.; Gorni, T.; Jia, J.; Kawamura, M.; Ko, H.-Y.; Kokalj, A.; Küçükbenli, E.; Lazzeri, M.; Marsili, M.; Marzari, N.; Mauri, F.; Nguyen, N. L.; Nguyen, H.-V.; Otero-de-la-Roza, A.; Paulatto, L.; Poncé, S.; Rocca, D.; Sabatini, R.; Santra, B.; Schlipf, M.; Seitsonen, A. P.; Smogunov, A.; Timrov, I.; Thonhauser, T.; Umari, P.; Vast, N.; Wu, X.; Baroni, S., Advanced capabilities for materials modelling with Quantum ESPRESSO. *J. Phys.: Condens. Matter* 2017, *29*, 465901.

49. Greenwell, C.; Beran, G. J. O., Inaccurate Conformational Energies Still Hinder Crystal Structure Prediction in Flexible Organic Molecules. *Cryst. Growth Des.* 2020, *20*, 4875−4881.

50. Dracinsky, M.; Unzueta, P.; Beran, G. J. O., Improving the accuracy of solid-state nuclear magnetic resonance chemical shift prediction with a simple molecular correction. *Phys. Chem. Chem. Phys.* 2019, *21*, 14992-15000.

51. Greenwell, C.; Beran, G. J. O., Rubrene untwisted: common density functional theory calculations overestimate its deviant tendencies. *J. Mater. Chem. C* 2021, *9*, 2848-2857.

52. Beran, G. J. O., Solid state photodimerization of 9-tert-butyl anthracene ester produces an exceptionally metastable polymorph according to firstprinciples calculations. *Cryst. Eng. Comm.* 2019, *21*, 758–764.

53. Stevens, B.; Perez, S. R.; Ors, J. A., Photoperoxidation of unsaturated organic molecules. XIV. O_2 ^{1}Dg acceptor properties and reactivity. *J. Am. Chem. Soc.* 1974, *96*, 6846–6850.

54. Aubry, J.-M.; Pierlot, C.; Rigaudy, J.; Schmidt, R., Reversible Binding of Oxygen to Aromatic Compounds. *Acc. Chem. Res.* 2003, *36*, 668-675.

55. Dreuw, A.; Head-Gordon, M., Single-Reference ab Initio Methods for the Calculation of Excited States of Large Molecules. *Chem. Rev.* 2005, *105*, 4009–4037.

56. Leang, S. S.; Zahariev, F.; Gordon, M. S., Benchmarking the performance of time-dependent density functional methods. *J. Chem. Phys.* 2012, *136*, 104101.

57. Tannaci, J. F.; Noji, M.; McBee, J.; Tilley, T. D., 9,10-Dichlorooctafluoroanthracene as a Building block for n-Type Organic Semiconductors. *J. Org. Chem.* 2007, *72*, 5567-5573.

58. Medina, B. M.; Beljonne, D.; Egelhaaf, H. J.; Gierschner, J., Effect of Fluorination on the Electronic Structure and Optical Excitations of p-Conjugated Molecules. *J. Chem. Phys.* 2007, *126*, 111101/1-111101/6.

59. Wolff, T.; Müller, N., Regioselective photodimerization of polar 9-substituted anthracenes in micellar solutions. *J. Photochem.* 1983, *23*, 131-140.

60. Schutz, A.; Wolff, T., Regioselectivity in the photodimerization of 9-hydroxy-methylanthracene and 9-anthracene carboxylic acid esters in surfactant systems. *J. Photochem. Photobio. A* 1997, *109*, 251–258.

61. Salzillo, T.; Venuti, E.; Femoni, C.; Valle, R. G. D.; Tarroni, R.; Brillante, A., Crystal Structure of the 9-Anthracene−Carboxylic Acid Photochemical Dimer and Its Solvates by X-ray Diffraction and Raman Microscopy. *Cryst. Growth Des.* 2017, *17*, 3361−3370.

62. Wheeler, S. E., Understanding Substituent Effects in Noncovalent Interactions Involving Aromatic Rings. *Acc. Chem. Res.* 2013, *46*, 1029–1038.

63. McBride, J. M.; Segmuller, B. E.; Hollingsworth, M. D.; Mills, D. E.; Weber, B. A., Mechanical Stress and Reactivity in Organic Solids. *Science* 1986, *234*, 830-835.

64. Peachey, N. M.; Eckhardt, C. J., Energetics of Organic Solid-State Reactions: Lattice Dynamics in the 2,5-Distyrlpyrazine Photoreaction. *J. Phys. Chem.* 1993, *97*, 10849–10856.

65. Luty, T.; Eckhardt, C. J., General Theoretical Concepts for Solid State Reactions: Quantitative Formulation of the Reaction Cavity, Steric Compression, and Reaction-Induced Stress Using an Elastic Multipole Representation of Chemical Pressure. *J. Am. Chem. Soc.* 1995, *117*, 2441–2452.

66. Echegoyen, L.; Hafez, Y.; Lawson, R. C.; Mendoza, J. d.; Torres, T., Efficient synthesis of alkoxyanthraquinones from fluoroanthraquinones and their preliminary electrochemistry. *J. Org. Chem.* 1993, *58*, 2009–2012.

67. Haenel, M. W.; Oevers, S.; Bruckmann, J.; Kuhnigk, J.; Krüger, C., Facile Syntheses of 1,8-Bis(diphenylphosphino)anthracene and 1,8-Bis(dimethylamino)anthracene by Nucleophilic Substitution of 1,8-Difluoroanthracene. *SynLett* 1998, 301-303.

68. Kawada, Y.; Iwamura, H., Correlated rotation in bis(9-triptycyl)methanes and bis(9-triptycyl) ethers. Separation and interconversion of the phase isomers of labeled bevel gears. *J. Am. Chem. Soc.* 1983, *105*, 1449-1459.

69. Liebermann, C., Über die Einwirkung des Oxalylchlorids auf aromatische Kohlenwasserstoffe. *Berichte der deutschen chemischen Gesellschaft* 1912, *45*, 1186-1217.

70. House, H. O.; Ghali, N. I.; Haack, J. L.; VanDerveer, D., Reactions of the 1,8-diphenylanthracene system. *J. Org. Chem.* 1980, *45*, 1807–1817.

71. Lamm, J.-H.; Vishnevskiy, Y. V.; Ziemann, E.; Kinder, T. A.; Neumann, B.; Stammler, H.-G.; Mitzel, N. W., Syntheses and Structures of 10-Trimethylelement-Substituted 1,8-Dichloroanthracenes. *Eur. J. Inorg. Chem.* 2014, 941-947.

72. *APEX 2*, version 2014.1-1, Bruker (2014), Bruker AXS Inc., Madison, Wisconsin, USA.

73. *SAINT*, version V8.34A, Bruker (2012), Bruker AXS Inc., Madison, Wisconsin, USA.

74. *SADABS*, version 2012/1, Bruker (2012), Bruker AXS Inc., Madison, Wisconsin, USA.

75. *SHELXTL*, version 2013/4, Bruker (2013), Bruker AXS Inc., Madison, Wisconsin, USA.

Chapter 5 Characterization of Highly Stable Solid-State Nitrenes Created by Photolysis of Crystalline 4-Azido-2,3,5,6-tetrafluorobenzoic acid

5.1 Abstract

The structure, spectroscopy, and photochemistry of 4-azidobenzoic acid (**4ABC**) and its perfluorinated analog 4-Azido-2,3,5,6-tetrafluorobenzoic acid (**4F4ABC**) are characterized in both frozen glasses and crystals. Photolysis of the parent azides leads to the production of nitrenes and other spin species that are probed by electron paramagnetic resonance (EPR) and optical spectroscopy. Fluorination leads to large, nonintuitive shifts in the nitrene absorption spectra, which were analyzed using density functional calculations. Photolysis generates ~10× higher yield of the triplet nitrene in **4F4ABC** relative to the quintet and radical side-products, while the radical side-product is the dominant species in **4ABC**. The unwanted spin side-products in the **4F4ABC** crystal could be removed through a raised-temperature annealing step, creating a solid where the nitrene was the dominant spin species. In a solution the nitrene survives for less than 1 s, but in the **4F4ABC** crystal it has a lifetime of about 20 days at room temperature in open air. Analysis of the electron spin resonance lineshapes suggests that the remarkable stability of this nitrene results from the **4F4ABC** crystal's different packing that traps N_2 molecules adjacent to the nitrene. This stability makes it possible to photopattern them into a single crystal and characterize their photoluminescence. The ability to create solid-state nitrene samples that are stable for up to a month under ambient conditions suggests that they could form the basis of new materials with potential applications in spintronics and quantum information science.

5.2 Introduction

Unpaired electrons in molecules can give rise to high-spin configurations that have possible applications for magnetic sensing[1], spintronics[2], light emission[3], and nonlinear optics[4]. More recently, such species have attracted attention as elements for quantum information science.[5-7] In this latter application, most work has centered on metal-ligand complexes where the electrons adopt stable, unpaired spin configurations in the central metal atom's *d* and *f* orbitals.[8-11] For organic molecules, open-shell configurations tend to be very unstable, and this area is just beginning to be explored.[12] One high-spin carbon-nitrogen species that has attracted considerable interest for quantum information applications is the diamond vacancy center (DVC), consisting of a nitrogen impurity atom embedded in a diamond lattice.[13-15] It exists in a triplet ground state with three nondegenerate sublevels that can be placed in superposition states using microwave excitation. Thanks to its high fluorescence quantum yield, spin dynamics in single DVC can be probed by optically detected magnetic resonance (ODMR) experiments. The rigid carbon lattice helps prevent decoherence due to phonons and spin-orbit coupling from rapidly degrading the spin superposition states necessary for quantum applications.

Nitrenes are probably the closest organic chemistry analog to the DVC, since they also possess a triplet ground state.[16] But although the possibility of using nitrenes in quantum information science has been raised in the literature[17], their instability has prevented any significant experimental efforts in this direction. Nitrene species are typically created by azide photolysis and intersystem crossing to form the triplet ground state.[18] The triplet nitrene typically has a sub-second lifetime at room temperature in condensed phase environments due to reactions with oxygen[19], hydrogen abstraction[20], and

molecular rearrangements.[21, 22] A nitrene species is often regarded as "stable" or "persistent" if it is stable above liquid nitrogen temperatures[23, 24] or survives for microseconds at room temperature[25], but practical applications require much longer lifetimes.

Some previous work suggests that nitrenes can be stabilized in a crystal environment if they are created *in situ* by photolysis of the parent azide. Moriarty et al. reported a triplet nitrene that survived for approximately one week at room temperature after photolysis of crystalline cyanuric acid.[26] Sugawara and coworkers showed that when 4-azidobenzoic acid (**4ABC**) crystallized in a head-to-head stacking motif, photolysis of the crystal produced a triplet nitrene species that survived for up to 10 days at room temperature.[27, 28] The nitrene stability was attributed to trapped N_2 molecules that slowed down subsequent side reactions of the nitrenes, like hydrogen abstraction and nitrogen insertion. While this work provided evidence that it was possible for nitrenes to survive in a crystalline environment, it also had some limitations. No EPR spectra or detailed characterization of the long-lived nitrene species were provided. The presence of other high-spin signals, like doublets and quintets, suggested that side reactions resulted in a complex mixture of EPR active species. As we show below, the nitrene triplet was actually a minor component in the **4ABC** system. Lastly, irreversible shifting and loss of intensity in the EPR spectrum occurred when the **4ABC** crystal was warmed to room temperature.

These earlier observations of long-lived triplet nitrenes motivated us to revisit the **4ABC** crystal system using additional characterization techniques and new synthetic analogs. Specifically, we reasoned that fluorine substitution could reduce the propensity

for side reactions that involved hydrogen abstraction as well as modify the crystal packing due to stronger electrostatic interactions. To test this hypothesis, we compared the structure, spectroscopy, and photochemistry of **4ABC** with its perfluorinated analog 4-Azido-2,3,5,6-tetrafluorobenzoic acid (**4F4ABC**) in frozen glasses and crystals. Electron paramagnetic resonance (EPR) and optical spectroscopy measurements were used to monitor the production of nitrenes and other spin species. The large, nonintuitive shifts in the nitrene optical properties were analyzed using density functional calculations. Benefits of the fluorinated derivative include much greater stability, the ability to remove unwanted spin side-products through a raised-temperature annealing step, and red-shifted absorption and emission spectra. These advantages appear to result from the modified crystal packing in **4F4ABC** that traps the N_2 produced by azide photolysis inside the crystal and excludes O_2, providing an effective inert gas matrix that preserves the unstable nitrene. The ability to create solid-state nitrene samples that are stable for days in air and at room temperature should enable new types of experimental studies, for example spin measurements that could be used to assess their potential as molecular qubits. Solid-state materials based on open-shell species could have novel properties with applications ranging from nonlinear optics to quantum information science.

5.3 Experimental

5.3.1 Sample Preparation:

4ABC and **4F4ABC** were purchased from Tokyo Chemical Industries (TCI) and used without further preparation. Methyl Tetrahydrofuran (MTHF) was purchased from TCI and used without further purification. Acetone and methanol were obtained from

Fischer Scientific and used as received. Crystals of **4F4ABC** and **4ABC** were grown using solvent evaporation. 20 mg of the compound was placed into a 20 ml vial and 0.7 ml of methanol or acetone were added. The solution was loosely capped, and the solvent slowly evaporated over the course of several days. Needle like crystals formed. Powdered samples for EPR were obtained directly from the bottle or after grinding using a mortar and pestle. Both sample preparation methods gave the same EPR signals. Glasses of **4F4ABC** and **4ABC** were prepared using a 10^{-3} M solution in MTHF that had been stored in the dark. The solution was poured into a Type 32 Standard Cylindrical Polarimeter Cell (Firefly Scientific) with a path length of 2 mm. The cell opening was capped with a Teflon stopper. The cell was covered with indium metal and mounted in a Janis ST-100 cryostat. The cryostat was cooled using liquid nitrogen for at least four hours to ensure the sample attained thermal equilibrium.

5.3.2 Characterization:

To photolyze the samples, they were irradiated for one minute with a 15 W 365 nm mercury lamp immediately before analysis. Solution and glass absorption spectra were acquired using a Cary 60 UV-Vis Spectrometer. Diffuse reflectance measurements on crystalline samples were taken using a Shimadzu UV-3101PC. The crystal powders were reacted prior to being pressed into a barium sulfate matrix. For EPR measurements, the powders were placed in 4 mm Thin Wall Suprasil Economy EPR tubes, and spectra were acquired using a Brucker EMX X-band spectrometer with a high sensitivity cavity. Temperature control was accomplished by a Eurotherm temperature control unit. EPR spectra were fit using EasySpin. Data was imported into the program and fit utilizing the

esfit function. Initial zero-field parameters were obtained from previous literature.[28] A Gaussian line broadening setting of 1 was used and all parameters were varied until the root-mean-square-deviation was minimized.

5.3.3 Computational Details:

Molecular geometries were optimized in vacuum using density functional theory (DFT) in combination with the (unrestricted) B3LYP exchange-correlation functional[29] and the 6-31+G(d,p) basis set. Vibrational frequencies were computed for all the molecular geometries and no imaginary frequencies were found, confirming that all the geometries correspond to minima of the potential energy surface. Singlet-to-singlet (azides) and triplet-to-triplet (nitrenes) vertical transitions have been obtained within the (linear response) time-dependent DFT (TDDFT) using the CAM-B3LYP exchange-correlation functional[30] and the same basis set as in ground state calculations. Dependence of excitation energies with respect to the computational level can be found in the Supporting Information (Table S2). Simulated absorption spectra were generated by the convolution of Gaussian functions (half-bandwidth of 3226.2 cm^{-1}) centered at the computed vertical excitation energies at the Franck-Condon geometries. All calculations were performed with the Gaussian 16 package.[31]

5.4 Results

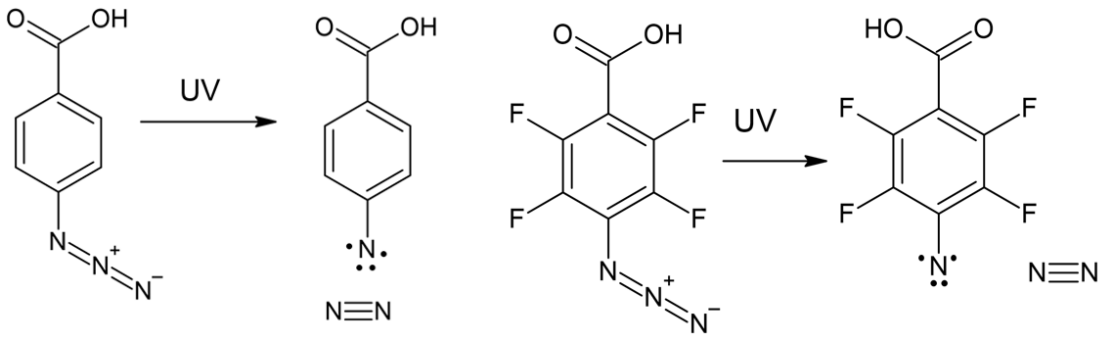

Figure 5.1: The azide group in **4ABC** is cleaved when exposed to UV light, leaving the nitrene attached to the benzoic acid and a separated N_2 molecule. A similar reaction occurs in **4F4ABC**.

The azides **4ABC** and **4F4ABC** differ only by the substitution of F-atoms for the H-atoms on the phenyl ring. The first question is whether this substitution leads to different properties at the molecular level. Calculations indicate that the two molecules adopt identical geometries, but their electronic structures are significantly different. This can be seen by the substantial blue-shift of the **4F4ABC** ultraviolet absorbance relative to **4ABC**, as shown in Figure 2A. This large blue-shift shift is not typically seen when polycyclic aromatic hydrocarbons or their carboxylic acid derivatives are fluorinated.[32-36] To understand the origin of this shift, we turned to TDDFT calculations, and the calculated energy levels and orbitals of the azides are shown in Figure 2B. Fluorine substitution causes both HOMO and LUMO to shift down in energy, but the HOMO is more stabilized, and this opens up a larger gap in **4F4ABC**. The lower lying HOMO-1 orbitals are almost completely unaffected by F-atom substitution but play no role in the lowest energy transition. The calculated energy shift for the $S_1 \leftarrow S_0$ transition of 0.1 eV in **4F4ABC** with respect to **4ABC** is similar to the experimentally observed blueshift of 0.2 eV.

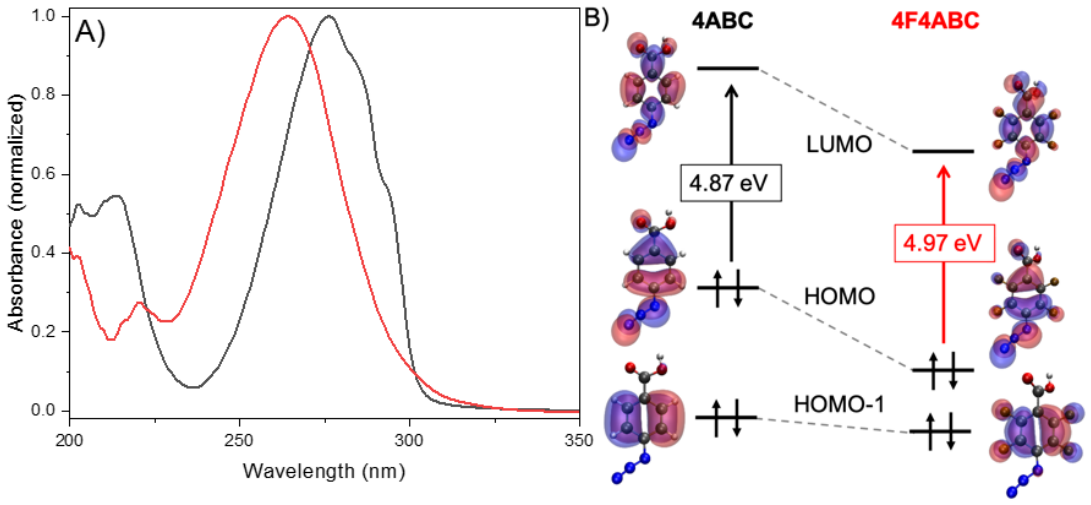

Figure 5.2: A) The absorbance of unreacted azides **4ABC** (black) and **4F4ABC** (red). B) Frontier molecular orbital diagram for the singlet ground state of **4ABC** (left) and **4F4ABC** (right) azides. Vertical arrows (with computed excitation energies) indicate the main contribution to the $S_1 \leftarrow S_0$ transition corresponding to the lowest absorption band in A).

In solution, **4ABC** and **4F4ABC** both undergo azide photolysis as shown in Figure 5.1. The resulting nitrenes react within seconds to generate various species in room temperature solution, causing the solution to turn to a characteristic yellow brown color due to a broad, featureless absorption that extends into the visible region and probably belongs to a nitro species (Supporting Information). The same decomposition also occurs within minutes in an organic glass if the temperature is above 90 K. Only at lower temperatures were we able to trap both nitrenes in a Me-THF glass and characterize them. The presence of the nitrene was confirmed by EPR measurements (Supporting Information, Figure S6). In particular, we could take absorption spectra of the two molecular species, which are shown in Figure 3. The absorption of the **4ABC** nitrene resembles that of other aromatic nitrenes measured in low temperature glasses.[37, 38] Remarkably, F-substitution

shifted the triplet nitrene absorption into the visible region, resulting in a deep purple color after irradiation. We were surprised that a small molecule like **4F4ABC** could give rise to such a strong absorption at visible wavelengths. Previous results on the absorption of fluorinated phenyl nitrenes in their singlet states gave no indication of such large shifts.[39]

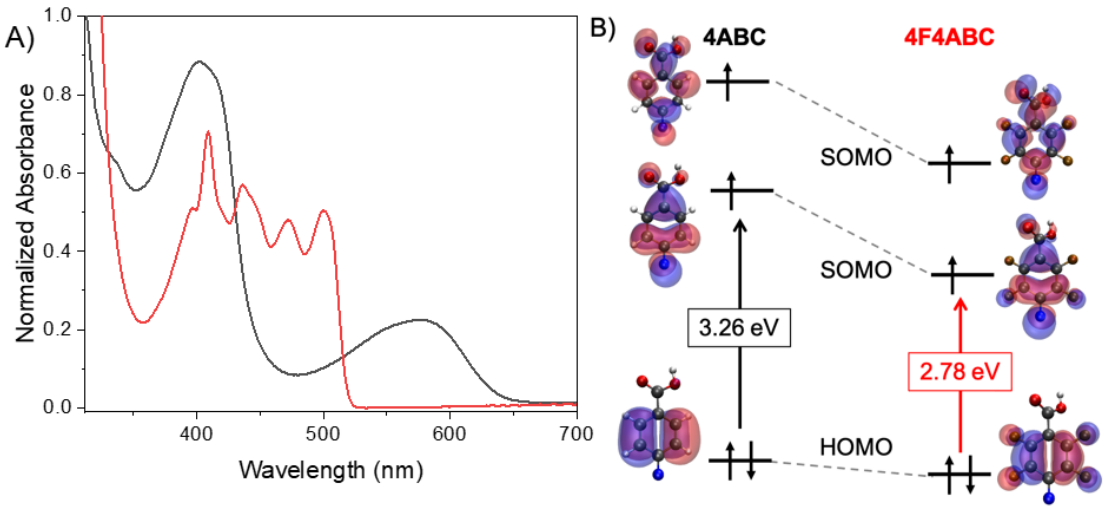

Figure 5.3: A) The absorbance of nitrenes generated from **4ABC** (red) and **4F4ABC** (black) in a Me-THF glass B) Frontier molecular orbital diagram for the triplet ground state of **4ABC** (left) and **4F4ABC** (right) nitrenes. Vertical arrows (with computed excitation energies) indicate the main contribution to the $T_1 \leftarrow T_0$ transition corresponding to the lowest absorption band in A).

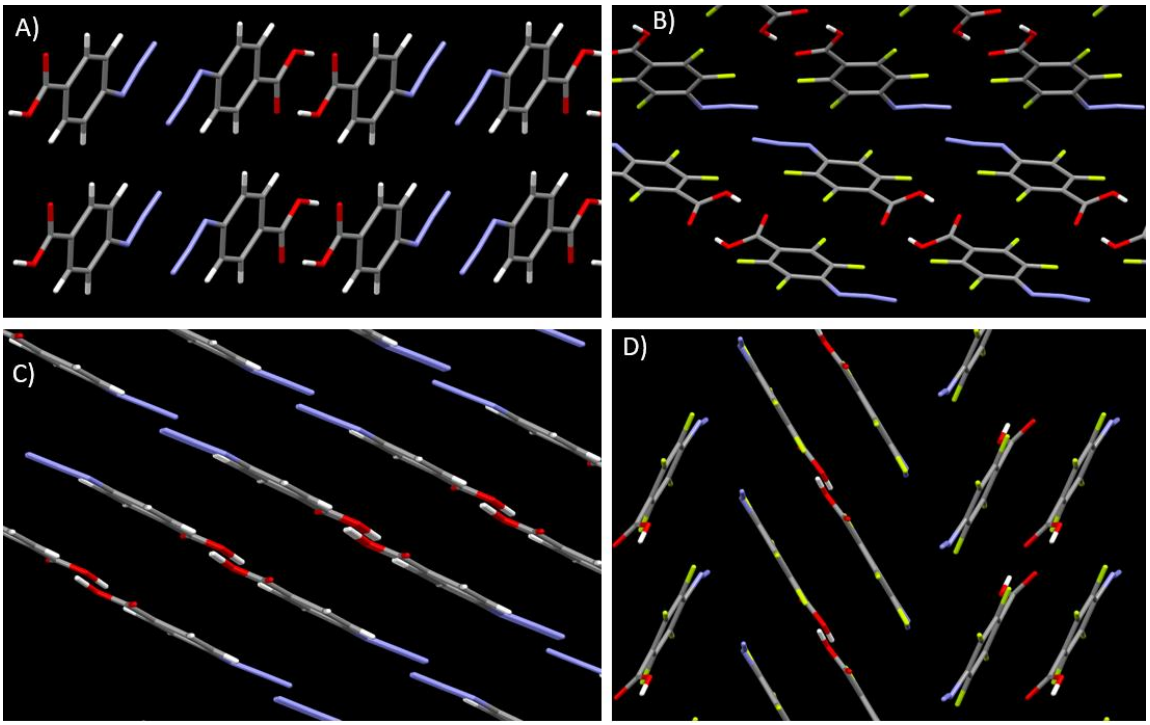

Figure 5.4: Crystal packing of **4ABC** A) and **4F4ABC** C) showing aromatic planes and carboxylic acid interactions. When viewed parallel to the aromatic ring planes, C) **4ABC** forms sheets of molecules while D) **4F4ABC** forms opposing stacks of molecules.

The different spectral shifts induced by fluorination in the nitrenes as compared to the parent azides, along with their large redshifts, motivated us to return to the TDDFT calculations. Stabilization of nitrenes' frontier orbitals by F-atom substitution is similar to that in the azides, but with a different electronic occupancy due to the triplet state nature of the ground state (Figure 3B). In the nitrenes, the azide HOMO-1 orbital evolves to become the HOMO, while the previous HOMO and LUMO become the two singly occupied molecular orbitals (SOMOs). Calculations revealed that the lowest triplet state excitation corresponds to the HOMO→SOMO electron transition, which carries appreciable oscillator strength and can be associated with to the lowest energy band in the absorption spectra (Figure 3A). The lack of sensitivity of the HOMO (previously the

HOMO-1 in the azides) to fluorine substitution means that the optical gap is now controlled by the stabilization of the SOMO (previously the HOMO in the azides). The same F-induced stabilization of this orbital that increased the optical gap in the azides now decreases the optical gap for the nitrenes. The TDDFT calculated shift for the $T_1 \leftarrow T_0$ transition (-0.48 eV) is in reasonable agreement with the observed shift (-0.3 eV). The different absorption shifts seen in the azides and nitrenes arise from the involvement of different molecular orbitals in their electron configurations. We suspect that this counterintuitive shifting will be found in other closed-shell versus open-shell molecules as substituent effects are investigated in more detail.

The spectroscopic characterization of the dilute nitrenes had to be carried out at cryogenic temperatures to prevent decomposition. We wanted to stabilize the nitrenes by trading the disordered environment of the glass for the tightly packed environment of the crystal. **4ABC** crystallizes in two-dimensional sheets, where the COOH groups hydrogen bond to each other and the azide groups face each other within the sheets as shown in Figures 4A, C. This head-to-head stacking motif is seen in other aromatic carboxylic acids because the COOH group is a strong structure directing group.[40, 41] Because the **4ABC** crystal packing is dominated by hydrogen bond interactions, we hypothesized that substitution on the aromatic ring would not lead to major changes. Indeed, **4F4ABC** crystallizes with the same head-to-head hydrogen-bonded pairs as **4ABC** but with one important difference. In **4F4ABC** the hydrogen-bonded pairs crystallize not in sheets but as dimer stacks tilted at opposing angles (Figures 4B, D). This arrangement is reminiscent of herringbone packing in that it allows the F-atoms to interact with the π-conjugated

aromatic rings more directly. The role of F atom substitution in modifying crystal structures is complicated because there are multiple weak intermolecular interactions that can be affected.[42] Both repulsive [43] and attractive[43] forces have been attributed to F···F interactions, making it difficult to predict their effect on molecular packing. However, several experimental results have shown that the presence of F atoms on aromatic rings can disrupt planar stacking[44, 45], consistent with what is observed in this paper. Interestingly, the herringbone pair packing motif requires a significantly more space per molecule, with a single **4ABC** molecule occupying 183.6 $Å^3$ and single **4F4ABC** molecule occupying 196.7 $Å^3$. But even though the **4F4ABC** crystal is less densely packed, the azide corridor is more constricted due to the closer approach of the tilted azide groups. Figure 5 compares the free volume available for N atom movement in both crystal structures, taking the radius of a N atom to be 0.65 Angstroms. A helical pathway can be seen in the **4ABC** crystal that presumably leads to a greater probability for N_2 diffusion and escape. If close association of the N_2 is necessary to stabilize the nitrene, then the **4F4ABC** crystal should give rise to a more long-lived nitrene and fewer side products. The smaller voids in **4F4ABC** would also suppress the penetration of other gases, like O_2, that can react with the nitrene.

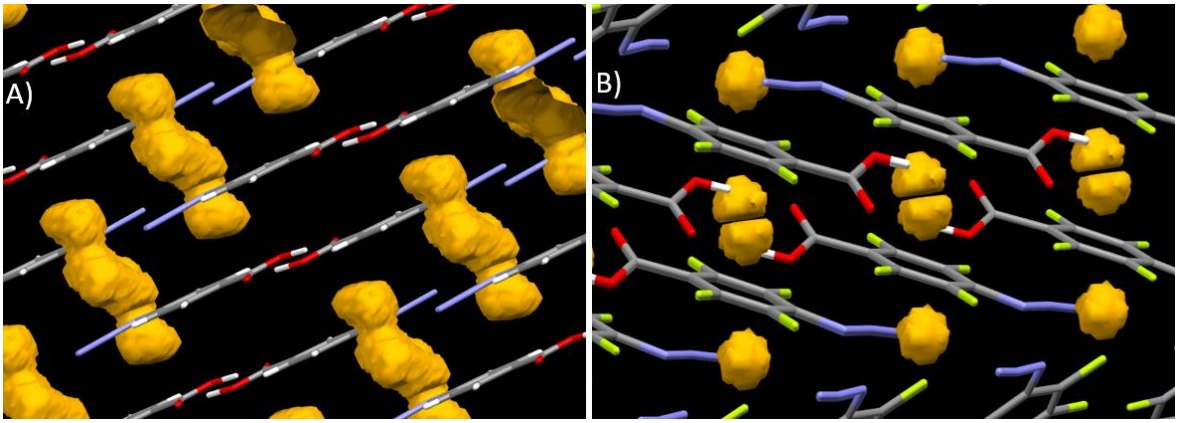

Figure 5.5: A) A comparison of the void space between **4ABC** and B) **4F4ABC**. The voids in **4ABC** form columns running along the azide corridor while **4F4ABC's** voids are more isolated. The total void space is 4.7% in **4ABC** and 0.6% in **4F4ABC** as measured with a probe radius 0.65 Å grid spacing 0.2 Å

EPR measurements confirm that fluorination and its accompanying crystal structure changes dramatically affect nitrene production and stability. When the **4ABC** and **4F4ABC** crystal powders are irradiated at 80 K and analyzed at 100 K, the EPR spectra exhibit three distinct signal regions at 2.5 kG, 3.2 kG and 6.7 kG (Figure 5.6). Sugawara and coworkers assigned these signals to a quintet, biradical, and triplet species, respectively.[28] Preliminary kinetic studies suggest that the quintet and biradical signals are produced by subsequent excitation of the nitrene that is produced by initial photolysis of the azide (Supporting Information). The radical signal is likely a decomposition product of the nitrene, possibly due to hydrogen abstraction at a defect site[20] or molecular rearrangement.[46] The quintet signal is expected if two cofacial azide groups both undergo photolysis because the resulting nitrenes would form a triplet pair that can support quintet states.[47]

	D (MHz)	E (MHz)	Hyperfine N1 (MHz)	Hyperfine N2 (MHz)	Hyperfine N3 (MHz)	G tensor	RMSD
4ABC	29114	27.5	37.9	N/A	N/A	2, 2, 1	.0335
4F4ABC	30161	26.22	44.59	88.7	86.34	2, 2, 1.38	.0983

Table 5:1: The values of the best fits obtained from easyspin.

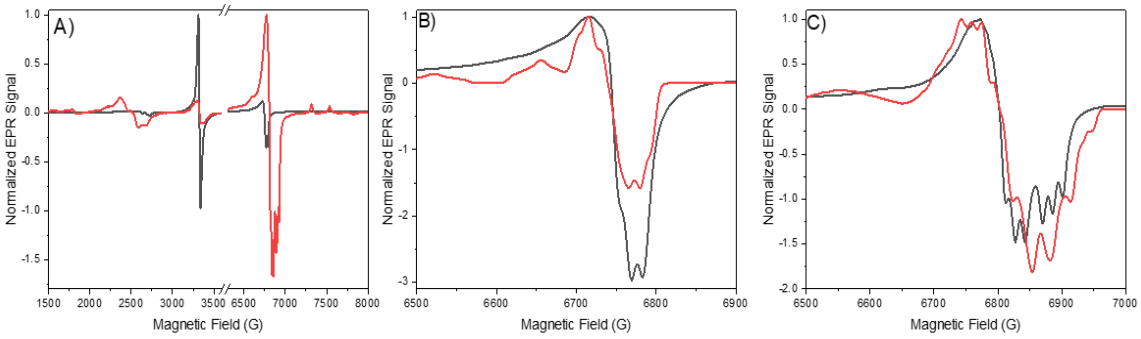

Figure 5.6: A) The EPR spectrum of **4ABC** (black) and **4F4ABC** (red) showing a weak quintet species at 2700 G, a biradical species at 3300G and a triplet signal at 6700 G. B) The experimental **4ABC** triplet signal at 6700 G (black) and simulated spectrum using the parameters in Table 1 with one hyperfine coupled nitrogen. C) The experimental triplet signal of **4F4ABC** (black) and simulated spectrum with three hyperfine coupled nitrogen atoms.

The first obvious difference between the two crystal EPR spectra is that the radical signal in the **4ABC** is substantially larger (~10×) than the triplet signal, while the reverse is true for the **4F4ABC** spectrum, consistent with fewer side reactions in this crystal. A second significant difference between the **4ABC** and **4F4ABC** crystals is the lineshape of the triplet signal. The fine structure seen in both signals originates from hyperfine coupling of the electron spin to the spin=1 nitrogen nucleus. A single N-atom with a nuclear spin of 1 should give rise to a set of 3 peaks due to hyperfine coupling, and this is the case for

4ABC. In order to fit the **4F4ABC** signal, however, we had to model the lineshape taking into account hyperfine coupling to three distinct N atoms that gave rise to 6 resolved peaks. Both fits to the triplet region of the EPR signal revealed zero-field splittings on the order of D=1 cm^{-1} and E=0.001 cm^{-1}, in good agreement with previous measurements and calculations on aromatic nitrenes.[48-51] Note that given the large D value, we only see one part of the triplet resonance in the X-band window. Table 1 summarizes the fit parameters used for both spectra. The asymmetric *G* tensor and the three inequivalent N hyperfine coupling constants are all consistent with the presence of an N_2 molecule in close proximity to the nitrene center. Interestingly, the fit parameters imply that the nitrene experiences greater hyperfine coupling due to the two nitrogens of the N_2 than to the central nitrogen atom. We are currently pursuing higher field EPR measurements to better resolve the hyperfine splitting and clarify the origin of these couplings. The values reported in this thesis should be regarded as prelimary

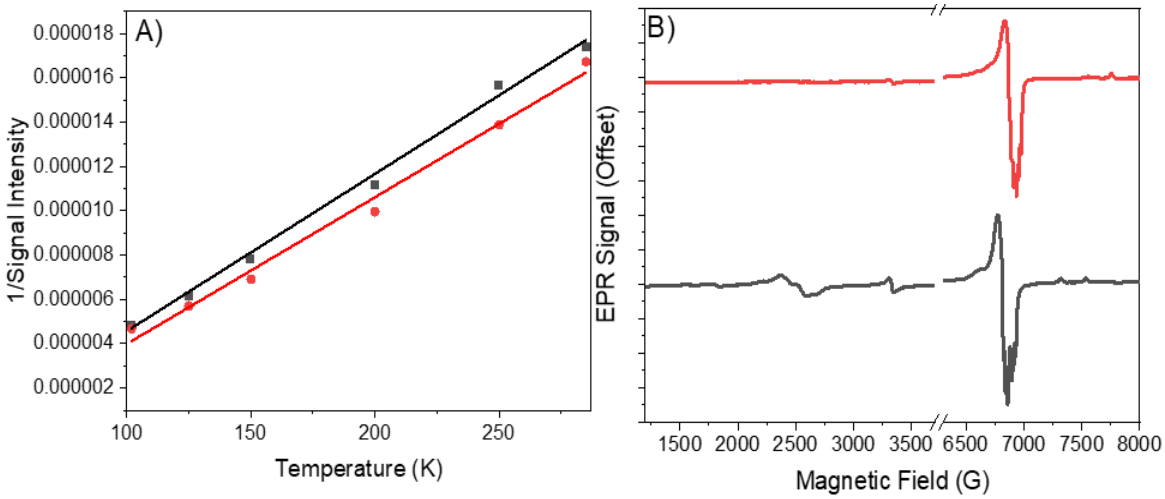

Figure 5.7: A) Curie plots of the triplet signal of **4F4ABC** for two cycles of heating from 100 K to room temperature (black and red) showing the stability of the nitrene triplet signal. B) EPR spectrum of **4F4ABC** at 100 K spectrum before annealing to 285 K (black) and after annealing (red), showing the drastic reduction of quintet and biradical species.

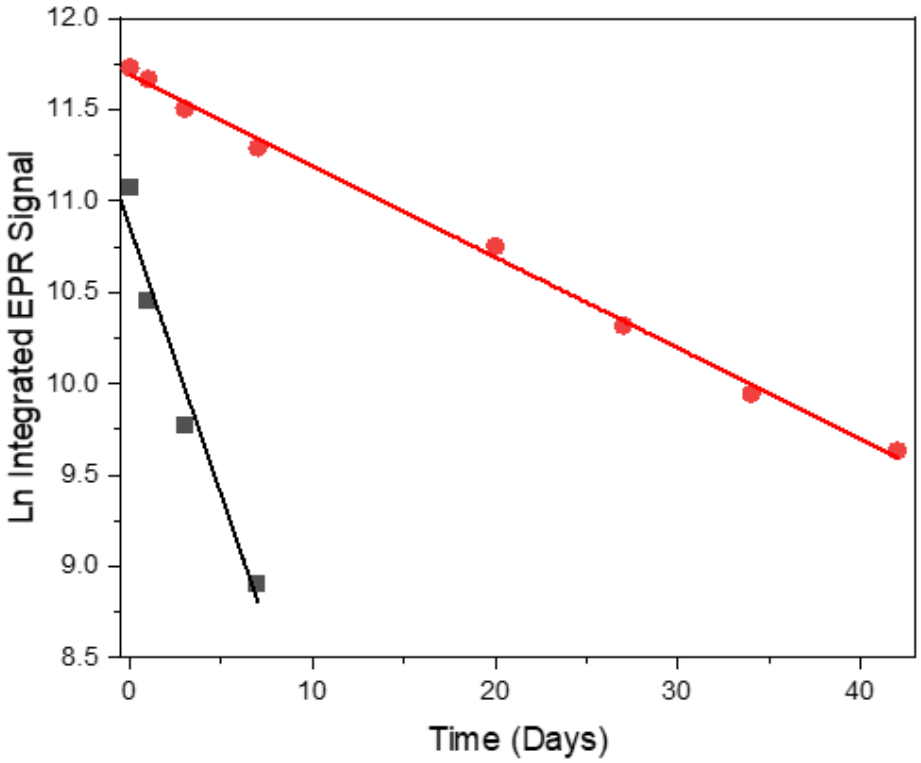

Figure 5.8: The long-term stability of the nitrene triplet for **4ABC** (black) and **4F4ABC** (red) as measured from the intensity of the integrated EPR signal. The linear least squares fit slope of the **4ABC** data is 0.29 $(day)^{-1}$ and 0.05 $(day)^{-1}$.

The features of the low-temperature EPR spectra evolve in different ways for the two crystals as the temperature is raised to 298 K. In both samples, the triplet signal loses intensity due to Curie's Law as seen in Figure 5.7A, but in the **4F4ABC** crystal, the triplet intensity can be completely recovered if the temperature is lowered back down as seen in Figure 5.7B. Furthermore, the spectrum is completely dominated by the triplet signal at 6.7 kG, with the quintet and radical signals almost completely eliminated. The **4ABC** signal, on the other hand, undergoes an irreversible loss of triplet intensity[27], as well as a shift in spectral shape (Supporting Information). For this crystal, lowering the temperature did not recover the original triplet signal intensity, nor does it restore the original triplet

lineshape. At room temperature in **4F4ABC**, it appears that increased reactivity consumes most of the quintet and radical side products but has little effect on the nitrene signal. In **4ABC**, the opposite is true: at room temperature, the nitrene is consumed while the side products increase. If **4F4ABC** is photolyzed at room temperature, the triplet signal is also the dominant species. Unlike the **4ABC** crystal, the **4F4ABC** crystal can be prepared at high temperature to produce a low-temperature sample composed almost exclusively of triplet nitrenes. In addition to the suppression of side products, the **4F4ABC** crystal also extends the lifetime of the nitrene. Figure 5.8 plots the decrease in triplet signals for both crystals, showing that the **4F4ABC** nitrene has a 6× longer lifetime in the open air and at room temperature than that of **4ABC**.

We think the enhanced stability of the nitrene in the **4F4ABC** crystal lattice results from its greater propensity to trap the N_2 molecules and exclude O_2. In addition to the EPR data, several other observations are consistent with this hypothesis. When the **4ABC** crystals were irradiated with 405 nm light, they often shattered (showing a strong photosalient effect) and bubbles could be observed escaping from crystals irradiated under water. Both observations are consistent with rapid escape of N_2 gas from the crystal.[52] Irradiation of the **4F4ABC** crystals under identical conditions did not produce bubbles or fragmentation. But when the reacted **4F4ABC** crystals were placed in an organic solvent to dissolve, bubble evolution was observed, presumably due to the trapped N_2 escaping as the surrounding crystal lattice dissolved (Supporting Information). It is interesting to note that many workers have used low temperature rare gas matrices to trap and characterize highly reactive open shell species like nitrenes. Such experiments typically require a high

vacuum gas handling apparatus and a cryostat. In **4F4ABC**, the crystal packing effectively builds in an inert gas matrix that is stable up to room temperature and requires no special equipment.

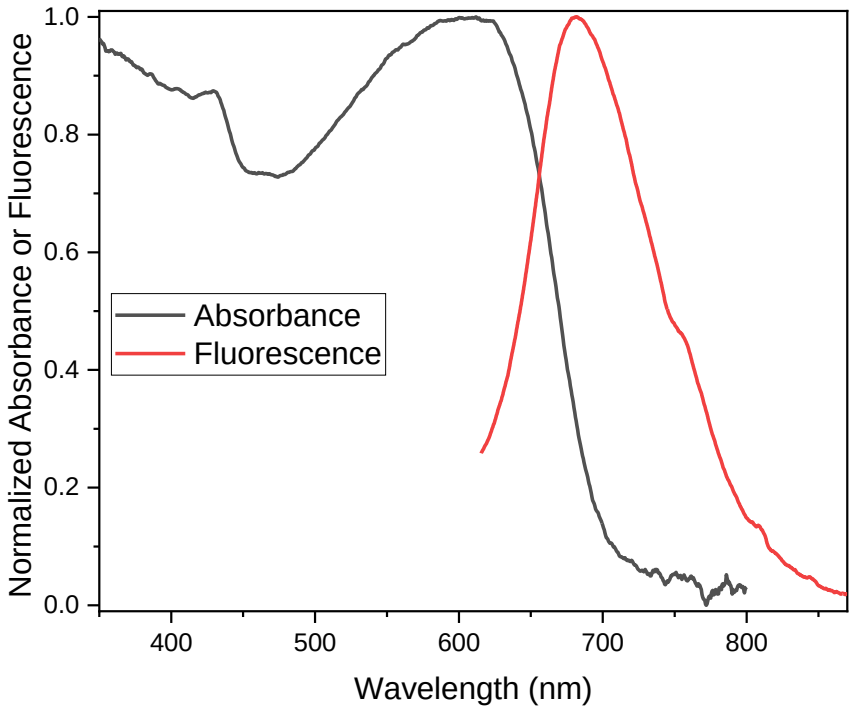

Figure 5.9: The absorbance (black) and fluorescence (red) of the **4F4ABC** nitrene in the solid state. The fluorescence was excited by a 532 nm laser. The peak of the absorbance is 612 nm and peak of the fluorescence is 681 nm.

The high stability of nitrenes in the **4F4ABC** crystal facilitates characterization of their photophysics. Diffuse reflectance measurements on a polycrystalline powder of **4F4ABC** revealed a broad absorption peaked at around 600 nm (Figure 5.9), similar to the spectrum measured for isolated molecules in the glass. Using 532 nm excitation, we measured the fluorescence spectrum of this species, which is also shown in Figure 5.9. The fluorescence of phenylnitrene has been observed only in the gas phase.[53, 54] Its small Stokes

shift and narrow lineshape as compared to the DVC luminescence spectrum[14, 55] suggests a smaller coupling to crystal phonons. The ability to measure fluorescence from this species in its crystalline environment suggests that highly sensitive photoluminescence detection of ODMR experiments, analogous to those performed using DVCs, may be possible. Of course, if the nitrenes are interrogated in an ODMR experiment, then the possibility of additional photochemistry must be taken into account. The wavelength dependent photochemistry of nitrene species is largely unexplored but could play a major role in determining whether they can be viable qubits.

Figure 5.10: Spatial patterning of nitrenes into a single crystal of **4F4ABC** leaves a purple square where the sample was exposed to 405 nm light. Similar results are obtained with 365 nm light.

Lastly, the ability to implant nitrene centers in a single crystal using light opens up the opportunity for optical patterning. Figure 5.10 shows a simple example of a square pattern written into a single crystal using a scanned 405 nm laser beam. The signature

purple color of the nitrene remains visible for weeks after patterning, even though the crystal is left exposed to air on a benchtop. If these nitrenes were to be harnessed as qubits, individually addressable centers would have to be created at well-defined locations within the crystal, and this seems to be feasible using high resolution optical patterning methods. Such a quantum circuit would only be stable for a few weeks under ambient conditions, but this lifetime can be greatly extended at cryogenic temperatures.

5.5 Conclusion

In this paper we have characterized the structure and properties of the nitrene species produced by photolysis of the azides **4ABC** and **4F4ABC**. At the molecular level, one novel observation is that fluorine substitution shifts the optical spectra well into the visible region, which can be understood in terms of the different molecular orbitals populated in the open-shell configurations. This shift permits its luminescence to be excited by common laser sources (e.g. 532 nm), similar to the DVC. From a materials standpoint, the **4F4ABC** crystal has multiple advantages over the non-fluorinated version. First, the initial photolysis generates ~10× higher yield of the triplet nitrene relative to the quintet and radical side-products. Second, the remaining side-products can be almost completely eliminated by thermal annealing. Third, the triplet nitrene has a lifetime of about 20 days, even at room temperature in open air. Evidence presented in this paper suggests that the remarkable stability of this nitrene, even at room temperature in the open air, results from the **4F4ABC** crystal's different packing that allows it to trap N_2 molecules to form an effective inert gas matrix for the nitrene, as well as prevent penetration of reactive molecules like O_2. The high chemical stability of these solid samples provides the opportunity to characterize their photoreactivity and spectroscopy. This advance also

suggests that metastable nitrenes could form the basis of new materials with potential applications in spintronics and information science. Finally, it is possible that the insights gained from crystal studies could guide the design of supramolecular containers that support long-lived nitrenes for use as spin sensors in complex environments.

5.6 Supporting Information

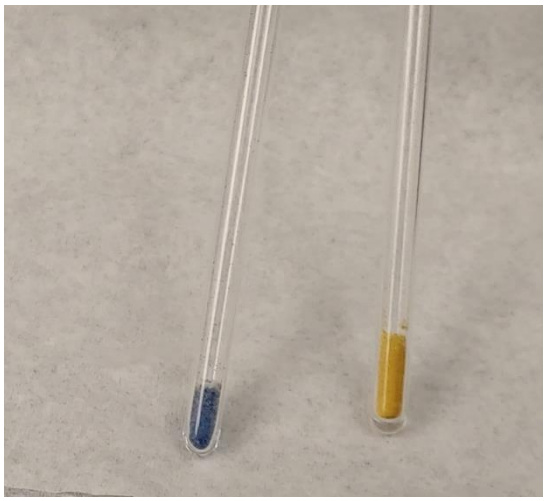

Figure S5.11: A photo of 4ABC (right) and 4F4ABC (left) after exposure to 365 nm light. 4ABC is orange while 4F4ABC is blue.

Figure S5.12: A photo of 4F4ABC dissolving in acetone. Small and large bubbles can be seen evolving from the sample. The dissolving portions are turning brown as the nitrene is reacting.

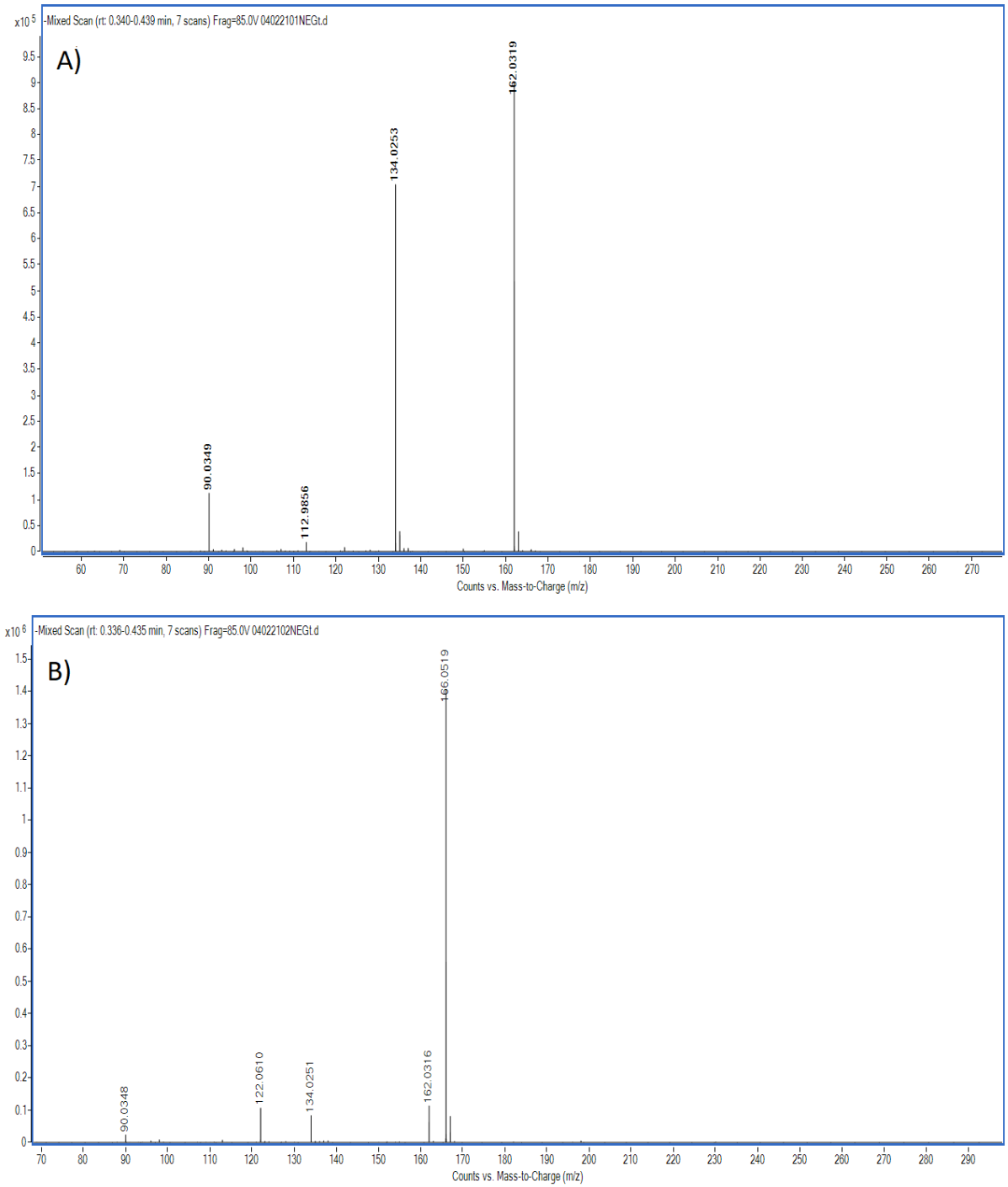

Figure S5.13: A) Mass spectrum of unreacted 4ABC. 162 corresponds to 4ABC. B) The 365nm exposed mass spectrum of 4ABC. The largest peak gains 4 amu which corresponds to a loss of N_2 and a gain of O_2. 166 corresponds to 4-nitrobenzoic acid.

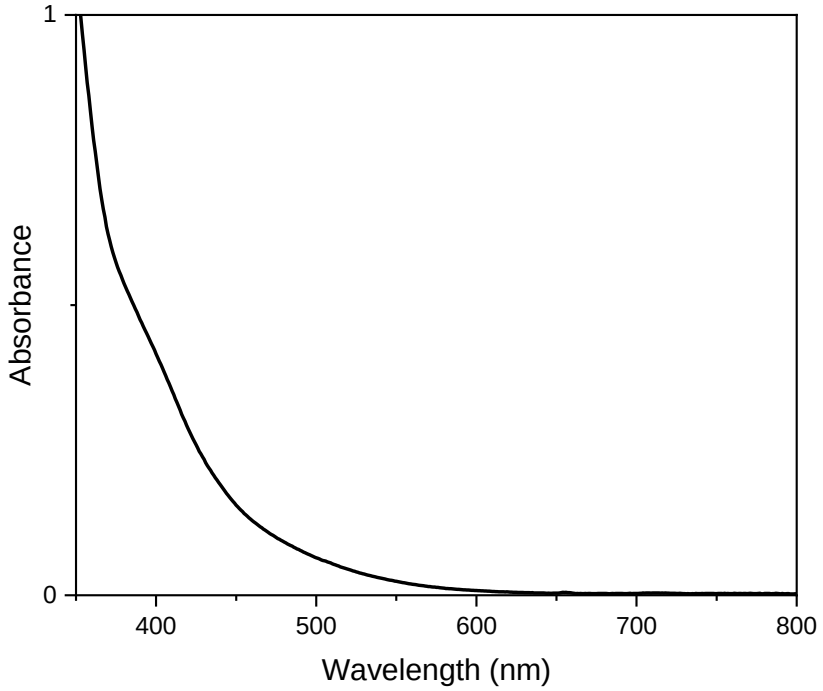

Figure S5.14: The absorbance of UV reacted 4ABC in methanol.

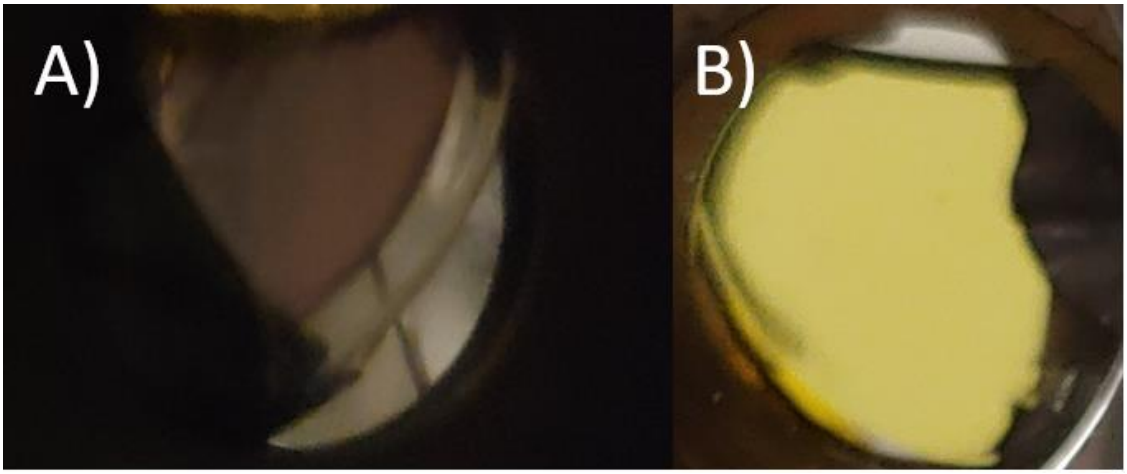

Figure S5.15: A) 4F4ABC in the cryostat in a methyl THF glass showing its distinctive purple color. B) 4ABC showing its yellow color. As the compounds react, they will turn to an orange-brown color.

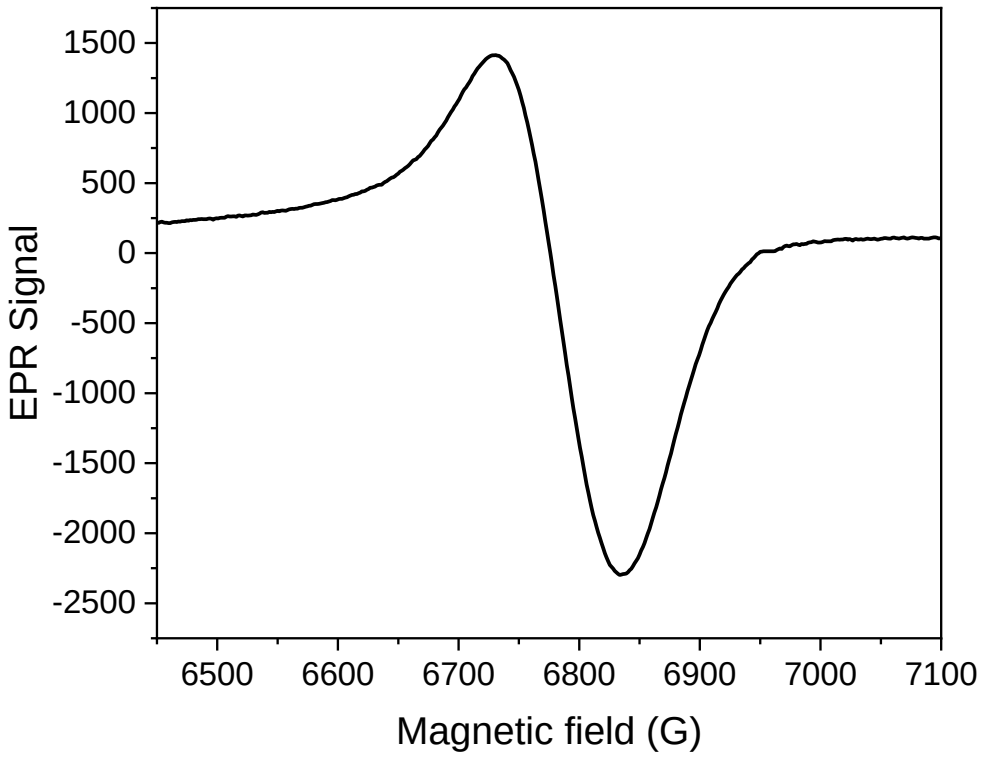

Figure S5.16: The triplet EPR signal of 4F4ABC in an ethanol glass at 100 K. The nitrene slowly reacted over the course of five minutes until the signal was gone.

Benchmark of the excitation energies for the azides 4ABC and 4F4ABC

	4ABC		4F4ABC	
Functional/Basis set	**6-31+G(d,p)**	**6-311+G(d,p)**	**6-31G+(d,p)**	**6-311+G(d,p)**
B3LYP	4.65	4.63	4.69	4.67
CAM-B3LYP	4.87	4.85	4.97	4.95
LC-wHPBE	5.04	5.01	5.06	5.11
M06-HF	5.04	5.02	5.19	5.18
wB97X-D	4.91	4.89	5.00	4.98

Table S5:2. Singlet-singlet vertical excitation energies (in eV) corresponding to the the HOMO --> LUMO transition for **4ABC** and **4F4ABC** azides computed within the (linear-response) TDDFT using the exchange-correlation functionals: B3LYP, CAM-B3LYP, LC-wHPBE, M06-HF and wB97X-D, and the basis sets 6-31+G(d,p) and 6-311+G(d,p). All the excitation energies were computed for the structures of the singlet ground state of the azides **4ABC** and **4F4ABC** optimized in vacuum in the frame of DFT in combination with the (unrestricted) B3LYP exchange-correlation functional and the 6-31+G(d,p) basis set.

Benchmark of the excitation energies for the nitrenes 4ABC and 4F4ABC

	4ABC		4F4ABC	
Functional/Basis set	**6-31+G(d,p)**	**6-311+G(d,p)**	**6-31G+(d,p)**	**6-311+G(d,p)**
B3LYP	2.94	2.93	2.40	2.39
CAM-B3LYP	3.26	3.25	2.77	2.76
LC-wHPBE	3.62	3.60	3.11	3.08
M06-HF	3.50	3.50	3.12	3.14
wB97X-D	3.24	3.23	2.74	2.73

Table S5:3: Lowest triplet-triplet vertical excitation energies (in eV) for **4ABC** and **4F4ABC** nitrenes computed within the (linear-response) TDDFT using the exchange-correlation functionals: B3LYP, CAM-B3LYP, LC-wHPBE, M06-HF and wB97X-D, and the basis sets 6-31+G(d,p) and 6-311+G(d,p). All excitation energies were computed for structures of the triplet ground state of the nitrenes **4ABC** and **4F4ABC** optimized in vacuum in the frame of DFT in combination with the (unrestricted) B3LYP exchange-correlation functional and the 6-31+G(d,p) basis set.

5.6.1 Reaction kinetics

One major advantage of the **4F4ABC** crystal is its ability to suppress the production of spin-active side-products. If they are directly produced by photoexcitation of the azide, in parallel with nitrene production, then their presence is unavoidable. For example, azide absorption events can release excess energy into its surroundings, driving motions that enable additional nitrene or radical production. On the other hand, these side-products could also be created by later nitrene photoexcitation events. In this case, it may be possible to control their production by adjusting the excitation wavelength and/or intensity. We tested both scenarios by fitting the time-dependent growth of the three EPR lineshapes at 2.5, 3.2 and 6.7 kG using kinetic models that reflect these two different sets of assumptions. Model 1 posits parallel creation of all three species by direct azide absorption and leads to the following set of rate equations:

$$N_O = N_A + N_T + N_Q + N_R \qquad (1a)$$

$$\frac{dN_T}{dt} = \sigma_A I \varphi_T \left(\mathrm{N}_O - \mathrm{N}_T - \mathrm{N}_Q - \mathrm{N}_R\right) \qquad (1b)$$

$$\frac{dN_Q}{dt} = \sigma_A I \varphi_Q \left(\mathrm{N}_O - \mathrm{N}_T - \mathrm{N}_Q - \mathrm{N}_R\right) \qquad (1c)$$

$$\frac{dN_R}{dt} = \sigma_A I \varphi_R \left(\mathrm{N}_O - \mathrm{N}_T - \mathrm{N}_Q - \mathrm{N}_R\right) \qquad (1d)$$

where N_A is the population of the ground state azide molecules, and N_T, N_R and N_Q are the populations of the triplet, radical and quintet species, respectively. N_0 is the total population of azide molecules before irradiation. σ_A is the absorption cross section of the

azide, *I* is the light intensity, and φ_T, φ_R, and φ_Q are the quantum yields for the formation of the three EPR-active species. In Equations (1), the T/Q/R species are produced independent of each other, except for the fact that they all come from the same ground state azide population N_A. For Model 2, we assume that the nitrene is the only species produced by azide absorption, and that subsequent absorption by the nitrene photoproduct itself is needed to generate the quintet and radical species. This model leads to a second set of rate equations:

$$\frac{dN_T}{dt} = \sigma_A I \varphi_T \mathrm{N}_A - \sigma_T I\left(\varphi_R + \varphi_Q\right) N_T \tag{2a}$$

$$\frac{dN_Q}{dt} = \sigma_T I \varphi_Q N_T \tag{2b}$$

$$\frac{dN_R}{dt} = \sigma_T I \varphi_R N_T \tag{2c}$$

where σ_T is the absorption cross section of nitrene its triplet ground state. Both models can be solved numerically, and details of the fitting process are provided in the Supporting Information. The parameters summarized in Table S1 were found to yield the best fits to the data. In Figure S5.17 we overlay the data with the fit results using Model 1, and in Figure 5.17b the data are overlaid with fits using Model 2. The kinetic data, particularly the shape of the increasing signals at early times, are much better reproduced by Model 2. This suggests that the quintet and radical side products are mainly generated by photoexcitation of nitrenes produced by an earlier photolysis of the azides.

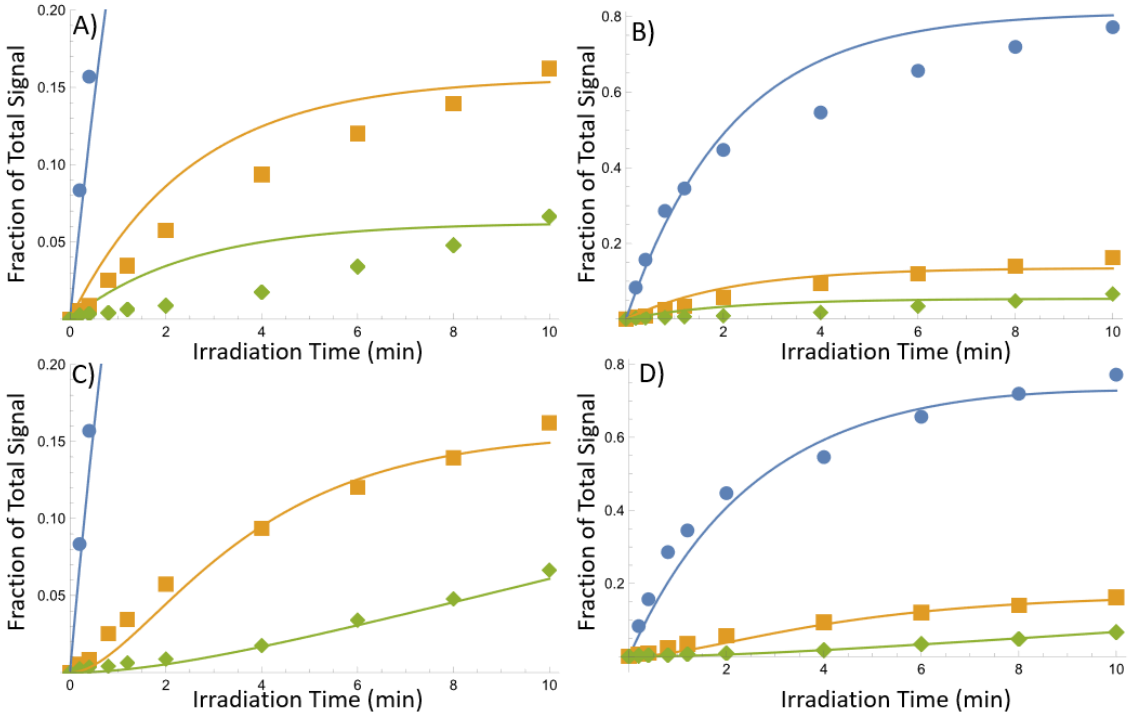

Figure S5.17: The kinetic modeling overlaid with the data from **4F4ABC**. Blue is the triplet, orange is the quintet, and green is the biradical. A) and B) are the result of Model 1, with the left vertical axis scaled to better show the quintet and radical growth. C) and D) are the result of Model 2.

	ϕ_T	ϕ_Q	ϕ_R	$\sigma_A I$	$\sigma_T I$
Method 1	1.5	.25	.1	.25	N/A
Method 2	.659	.2	.05	.2	.2

Table S5:4: The values of the best fits from the differential equation models.

5.7 References

1 Rodgers, C. T.; Hore, P. J., Chemical magnetoreception in birds: The radical pair mechanism. *Proc. Nat. Acad. Sci.* **2009,** *106*, 353–360.

2 Lupton, J. M.; McCamey, D. R.; Boehme, C., Coherent Spin Manipulation in Molecular Semiconductors: Getting a Handle on Organic Spintronics. *ChemPhysChem* **2010,** *11*, 3040 – 3058.

3 Ai, X.; Evans, E. W.; Dong, S.; Gillett, A. J.; Guo, H.; Chen, Y.; Hele, T. J. H.; Friend, R. H.; Li, F., Efficient radical-based light-emitting diodes with doublet emission. *Nature* **2018,** *563*.

4 Nakano, M.; Kishi, R.; Ohta, S.; Takahashi, H.; Kubo, T.; Kamada, K.; Ohta, K.; Botek, E.; Champagne, B., Relationship between Third-Order Nonlinear Optical Properties and Magnetic Interactions in Open-Shell Systems: A New Paradigm for Nonlinear Optics. *Phys. Rev. Lett.* **2007,** *99*, 033001

5 Atzori, M.; Sessoli, R., The Second Quantum Revolution: Role and Challenges of Molecular Chemistry. *J. Am. Chem. Soc.* **2019,** *141*, 11339−11352.

6 Gaita-Ariño, A.; Luis, F.; Hill, S.; Coronado, E., Molecular spins for quantum computation. *Nat. Chem.* **2019,** *11*, 301-309.

7 Wasielewski, M. R.; Forbes, M. D. E.; Frank, N. L.; Kowalski, K.; Scholes, G. D.; Yuen-Zhou, J.; Baldo, M. A.; Freedman, D. E.; Goldsmith, R. H.; III, T. G.; Kirk, M. L.; McCusker, J. K.; Ogilvie, J. P.; Shultz, D. A.; Stoll, S.; Whaley, K. B., Exploiting chemistry and molecular systems for quantum information science. *Nat. Chem. Rev.* **2020,** *4*, 490–504.

8 Ferrando-Soria, J.; Pineda, E. M.; Chiesa, A.; Fernandez, A.; Magee, S. A.; Carretta, S.; Santini, P.; Vitorica-Yrezabal, I. J.; Tuna, F.; Timco, G. A.; McInnes, E. J. L.; Winpenny, R. E. P., A modular design of molecular qubits to implement universal quantum gates. *Nat. Commun.* **2016,** *7*, 11377.

9 Gimenez-Santamarina, S.; Cardona-Serra, S.; Clemente-Juan, J. M.; Gaita-Arino, A.; Coronado, E., Exploiting clock transitions for the chemical design of resilient molecular spin qubits. *Chem. Sci.* **2020,** *11*, 10718–10728.

10 Fataftah, M. S.; Bayliss, S. L.; Laorenza, D. W.; Wang, X.; Phelan, B. T.; Wilson, C. B.; Mintun, P. J.; Kovos, B. D.; Wasielewski, M. R.; Han, S.; Sherwin, M. S.; Awschalom, D. D.; Freedman, D. E., Trigonal Bipyramidal V^{3+} Complex as an Optically Addressable Molecular Qubit Candidate. *J. Am. Chem. Soc.* **2020,** *142*, 20400−20408.

11 Bayliss, S. L.; Laorenza, D. W.; Mintun, P. J.; Kovos, B. D.; Freedman, D. E.; Awschalom, D. D., Optically addressable molecular spins for quantum information processing. *Science* **2020,** *370*, 1309–1312.

12 Lombardi, F.; Lodi, A.; Ma, J.; Liu, J.; Slota, M.; Narita, A.; Myers, W. K.; Müllen, K.; Feng, X.; Bogani, L., Quantum units from the topological engineering of molecular graphenoids. *Science* **2019,** *366*, 1107–1110.

13 Childress, L.; Hanson, R., Diamond NV centers for quantum computing and quantum networks. *MRS Bull.* **2012,** *38*, 134-138.

14 Doherty, M. W.; Manson, N. B.; Delaney, P.; Jelezko, F.; Wrachtrup, J.; Hollenberg, L. C. L., The nitrogen-vacancy colour centre in diamond. *Phys. Rep.* **2013,** *528*, 1-45.

15 Schirhagl, R.; Chang, K.; Loretz, M.; Degen, C. L., Nitrogen-Vacancy Centers in Diamond: Nanoscale Sensors for Physics and Biology. *Ann. Rev. Phys. Chem.* **2014,** *65*, 83-105.

16 Gritsan, N. P.; Platz, M. S., Kinetics, Spectroscopy, and Computational Chemistry of Arylnitrenes. *Chem. Rev.* **2006,** *106*.

17 Chapyshev, S. V.; Mendez-Vega, E.; Sander, W., Molecular Magnets – the Synthesis and Characterization of High-Spin Nitrenes. *Chem. Eur. J.* **2021,** *27*, 1258-1269.

18 Dürr, H.; Kober, H., Triplet states from Azides. *Topics in Current Chemistry* **1976,** *66*, 89–114.

19 Mieres-Pérez, J.; Mendez-Vega, E.; Velappan, K.; Sander, W., Reaction of Triplet Phenylnitrene with Molecular Oxygen. *J. Org. Chem.* **2015,** *80*, 11926−11931.

20 Sankaranarayanan, J.; Rajam, S.; Hadad, C. M.; Gudmundsdottir, A. D., The ability of triplet nitrenes to abstract hydrogen atoms. *J. Phys. Org. Chem.* **2010,** *23*, 370–375.

21 Xue, J.; Luk, H. L.; Eswaran, S. V.; Hadad, C. M.; Platz, M. S., Ultrafast Infrared and UV−Vis Studies of the Photochemistry of Methoxycarbonylphenyl Azides in Solution. *J. Phys. Chem. A* **2012,** *116*, 5325−5336.

22 Lu, B.; Qin, Y.; Lu, Y.; Liu, Q.; Zeng, X., Acryloylnitrenes: Spectroscopic Characterization, Spin Multiplicities, and Rearrangement to Vinyl Isocyanates. *J. Phys. Chem. A* **2020,** *124*, 6319−6329.

23 Mendez-Vega, E.; Mieres-Perez, J.; Chapyshev, S. V.; Sander, W., Persistent Organic High-Spin Trinitrenes. *Angew. Chem. Int. Ed.* **2019,** *58*, 12994 –12998.

24 Soleilhavoup, M.; Bertrand, G., Stable Carbenes, Nitrenes, Phosphinidenes, and Borylenes: Past and Future. *Chem* **2020,** *6*, 1275–1282.

25 Bucher, G.; Christina Tonshoff; Nicolaides, A., Photochemistry of an Azido-Functionalized Cryptand: Controlling the Reactivity of an Extremely Long-Lived Singlet Aryl Nitrene by Complexation to Alkali Cations. *J. Am. Chem. Soc.* **2005,** *127*, 6883-6892.

26 Moriarty, R. M.; Rahman, M.; King, G. J., Organic Nitrenes in Single Crystals. Observation of Hyperfine Structure in the Electron Spin Resonance. *J. Am. Chem. Soc.* **1966,** *88*, 842–843.

27 Mahe, L.; Izuoka, A.; Sugawara, T., How Crystalline Environment Can Provide Outstanding Stability and Chemistry for Arylnitrenes. *J. Am. Chem. Soc.* **1992,** *114*, 7904–7906.

28 Akito, S.; Loïc, M.; Akira, I.; Tadashi, S., Chemical Consequences of Aryl Nitrenes in the Crystalline Environment. *Bull. Chem. Soc. Jpn.* **1998,** *71*, 1259-1275.

29 Becke, A. D., A new mixing of Hartree–Fock and local density-functional theories. *J. Chem. Phys.* **1993,** *98*, 1372-1377.

30 Yanai, T.; Tew, D. P.; Handy, N. C., A new hybrid exchange–correlation functional using the Coulomb-attenuating method (CAM-B3LYP). *Chem. Phys. Lett.* **2004,** *393*, 51-57.

31 Frisch, M. J., Trucks, G.W., Schlegel, H.B., Scuseria, G.E., Robb, M.A., Cheeseman, J.R.; Scalmani, G.; Barone, V.; Petersson, G.A.; Nakatsuji, H.; Li, X.; Caricato, M.; Marenich, A.V.; Bloino, J., Janesko, B.G., Gomperts, R., Mennucci, B., Hratchian, H.P., Ortiz, J.V., Izmaylov, A.F., Sonnenberg, J.L., Williams-Young, D., Ding, F., Lipparini, F., Egidi, F., Goings, J., Peng, B., Petrone, A., Henderson, T., Ranasinghe, D., Zakrzewski, V.G., Gao, J., Rega, N., Zheng, G., Liang, W., Hada, M., Ehara, M., Toyota, K., Fukuda, R., Hasegawa, J., Ishida, M., Nakajima, T., Honda, Y., Kitao, O., Nakai, H., Vreven, T., Throssell, K., Montgomery Jr., J.A., Peralta, J.E., Ogliaro, F., Bearpark, M.J., Heyd, J.J., Brothers, E.N., Kudin, K.N., Staroverov, V.N., Keith, T.A., Kobayashi, R., Normand, J., Raghavachari, K., Rendell, A.P., Burant, J.C., Iyengar, S.S., Tomasi, J., Cossi, M., Millam, J.M., Klene, M., Adamo, C., Cammi, R., Ochterski, J.W., Martin, R.L., Morokuma, K., Farkas, O., Foresman, J.B., Fox, D.J. *Gaussian 16*, *Revision B.01*, Gaussian, Inc.: Wallingford CT, USA, 2016.

32 Medina, B. M.; Beljonne, D.; Egelhaaf, H. J.; Gierschner, J., Effect of Fluorination on the Electronic Structure and Optical Excitations of p-Conjugated Molecules. *J. Chem. Phys.* **2007,** *126*, 111101/1-111101/6.

33 Tannaci, J. F.; Noji, M.; McBee, J.; Tilley, T. D., 9,10-Dichlorooctafluoroanthracene as a Building block for n-Type Organic Semiconductors. *J. Org. Chem.* **2007,** *72*, 5567-5573.

34 Zhu, L.; Al-Kaysi, R. O.; Dillon, R. J.; Tham, F. S.; Bardeen, C. J., Crystal structures and photophysical properties of 9-anthracene carboxylic acid derivatives for photomechanical applications. *Cryst. Growth Des.* **2011,** *11*, 4975-4983.

35 Zhu, L.; Tong, F.; Salinas, C.; Al-Muhanna, M. K.; Tham, F. S.; Kisailus, D.; Al-Kaysi, R. O.; Bardeen, C. J., Improved Solid-State Photomechanical Materials by Fluorine Substitution of 9-Anthracene Carboxylic Acid. *Chem. Mater.* **2014,** *26*, 6007–6015.

36 Gately, T. J.; Sontising, W.; Easley, C. J.; Islam, I.; Al-Kaysi, R. O.; Beran, G. J. O.; Bardeen, C. J., Effect of halogen substitution on energies and dynamics of reversible photomechanical crystals based on 9-anthracenecarboxylic acid. *CrystEngComm* **2021,** *23*, 5931–5943.

37 Reiser, A.; Bowes, G.; Horne, R. J., Photolysis of Aromatic Azides Part 1 . Electronic Spectra of Aromatic Nitrenes and their Parent Azides. *Trans. Farad. Soc.* **1966,** *62*, 3162-3169.

38 V.A.Smirnov; S.B.Brichkin, Spectral and Photochemical Properties of Aromatic Nitrenes. *Chem. Phys. Lett.* **1982,** *87*, 548-551.

39 Nina P. Gritsan; Gudmundsdottir, A. D.; Tigelaar, D.; Zhu, Z.; Karney, W. L.; Hadad, C. M.; Platz, M. S., A Laser Flash Photolysis and Quantum Chemical Study of the Fluorinated Derivatives of Singlet Phenylnitrene. *J. Am. Chem. Soc.* **2001,** *123*, 1951-1962.

40 Ivasenko, O.; Perepichka, D. F., Mastering fundamentals of supramolecular design with carboxylic acids. Common lessons from X-ray crystallography and scanning tunneling microscopy. *Chem. Soc. Rev.* **2011,** *40*, 191–206.

41 More, R.; Scholz, M.; Busse, G.; Busse, L.; Paulmann, C.; Tolkiehn, M.; Techert, S., Hydrogen Bond Dynamics in Crystalline b-9-Anthracene Carboxylic Acid -- a Combined Crystallographic and Spectroscopic Study. *Phys. Chem. Chem. Phys.* **2012,** *14*, 10187-10195.

42 Reichenbacher, K.; Suss, H. I.; Hulliger, J., Fluorine in crystal engineering—''the little atom that could''. *Chem. Soc. Rev.* **2005,** *34*, 22–30.

43 Hathwar, V. R.; Row, T. N. G., Charge Density Analysis of Heterohalogen (Cl...F) and Homohalogen (F...F) Intermolecular Interactions in Molecular Crystals: Importance of the Extent of Polarizability. *Cryst. Growth. Des.* **2011,** *11*, 1338–1346.

44 Calvo-Castro, J.; Morris, G.; Kennedy, A. R.; McHugh, C. J., Effects of Fluorine Substitution on the Intermolecular Interactions, Energetics, and Packing Behavior of N-Benzyl Substituted Diketopyrrolopyrroles. *Cryst. Growth. Des.* **2016,** *16*, 2371−2384.

45 Komissarova, E. A.; Dominskiy, D. I.; Zhulanov, V. E.; Abashev, G. G.; Siddiqui, A.; Singh, S. P.; Sosorev, A. Y.; Paraschuk, D. Y., Unraveling the unusual effect of fluorination on crystal packing in an organic semiconductor. *Phys. Chem. Chem. Phys.* **2020,** *22*, 1665-1673.

46 Karney, W. L.; Borden, W. T., Why Does o-Fluorine Substitution Raise the Barrier to Ring Expansion of Phenylnitrene? *J. Am. Chem. Soc.* **1997,** *119*, 3347–3350.

47 Chapyshev, S. V.; Lavitskii, V. F.; Akimov, A. V.; Misochko, E. Y.; Shastin, A. V.; Korchagin, D. V.; Shilov, G. V.; Aldoshin, S. M., Photochemical generation of triplet—triplet nitrene pairs in aromatic diazide crystals. *Russ. Chem. Bull. Int. Ed.* **2008,** *57*, 524—531.

48 Kuck, V. J.; Wasserman, E.; Yager, W. A., Electron spin resonance of triplet nitrenes from aryl isocyanates. *J. Phys. Chem.* **1972,** *76*, 3570–3571.

49 Havlas, Z.; Kyvala, M.; Michl, J., Spin-orbit coupling in biradicals. 4. Zero-field splitting in triplet nitrenes, phosphinidenes, and arsinidenes. *Collect. Czech. Chem. Commun.* **2003,** *68*, 2335-2343.

50 Lu, Y.; Li, H.; Abe, M.; Begue, D.; Wan, H.; Deng, G.; Xu, J.; Liu, K.; Zeng, X., Sulfamoyl nitrenes: singlet or triplet ground state? *Chem. Commun.* **2018,** *54*, 6136-6139.

51 Abe, M.; Bégué, D.; Silva, H. S.; Dargelos, A.; Wentrup, C., Triplet States of Tetrazoles, Nitrenes, and Carbenes from Matrix Photolysis of Tetrazoles, and Phenylcyanamide as a Source of Phenylnitrene. *J. Phys. Chem. A* **2018,** *122*, 7276–7283.

52 Shields, D. J.; Karothu, D. P.; Sambath, K.; Ranaweera, R. A. A. U.; Schramm, S.; Duncan, A.; Duncan, B.; Krause, J. A.; Gudmundsdottir, A. D.; Naumov, P. e., Cracking under Internal Pressure: Photodynamic Behavior of Vinyl Azide Crystals through N_2 Release. *J. Am. Chem. Soc.* **2020,** *142*, 18565−18575.

53 Hancock, G.; McKendrickt, K. G., Laser-induced Fluorescence and Vibrational Relaxation of the Phenyl Nitrene Radical. *J. Chem. Soc., Faraday Trans. 2* **1987,** *83*, 2011-2024.

54 Ozawa, K.; Ishida, T.; Fuke, K.; Kaya, K., Electronic spectrum of jet-cooled phenyl nitrene. *Chem. Phys. Lett.* **1988,** *150*, 249-253.

55 Su, Z.; Ren, Z.; Bao, Y.; Lao, X.; Zhang, J.; Zhang, J.; Zhu, D.; Lu, Y.; Hao, Y.; Xu, S., Luminescence landscapes of nitrogen-vacancy centers in diamond: quasi-localized vibrational resonances and selective coupling. *J. Mater. Chem. C* **2019,** *7*, 8086--8091.

Chapter 6 : Conclusions and Future Work

In this dissertation we studied ways to optimize various photomechanical systems. By looking at ways to optimize existing systems more useful properties can be obtained. Three separate systems were observed. By using a better polymer matrix, we were able to create a reversible photochromic adhesive using spiropyran and zeonex. The addition of fluorines to 9AC greatly altered the back reaction rate of the molecules. Finally, fluorination of 4ABC led to a more stable nitrene radical through a tighter crystal structure.

6.1 Improving Reversible Adhesion

The SP ZX system is novel due to its reversibility. The system has very weak adhesion though, comparable to that of a sticky note. The requirement of special substrates limits the systems usefulness in real world applications. There are many potential ways that a photoreactive system could be used to strong adhesion. Mechanical adhesion, such as a screw or bolt, is typically the strongest type of adhesion as it requires a material failure to detach. There are three different designs that could be used to create photoreversible mechanical adhesion. The first is a photoreactive screw. The threads of the screw, when exposed to light, are blown off allowing the rest of the screw to be easily removed as seen in Figure 6.1. Light could be applied externally or through an optical window in the screw leading to the photoreactive areas. A molecule such as (E)-4-fluorocinnamaldehyde malononitrile ((E)-4FCM) would be a prime candidate for this screw design due to its photosalient nature[1].

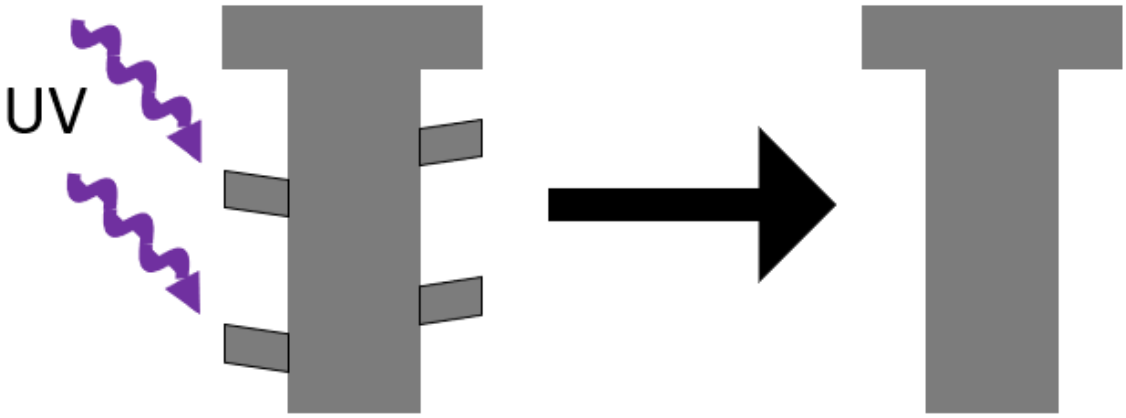

Figure 6.1: A potential design for a photoreactive explosive screw. When exposed to light the threads are blown off allowing the rest of the screw to be easily removed. Light could be applied externally or through an optical window in the screw leading to the photoreactive areas.

A second form of mechanical adhesion would be a light induced phase change material. Two rows of overlapping teeth can be placed together with a phase change material gluing the two surfaces together. The phase change material is doped with a molecule or nanoparticle that heats up when exposed to light. The resulting heat melts the phase change material and allows the surfaces to be separated. An example of this can be seen in Figure 6.2.

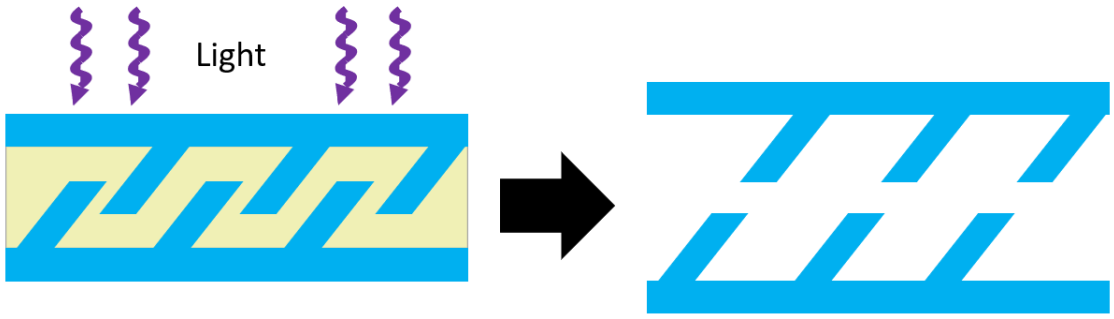

Figure 6.2: Another method of generating reversible adhesion using light. In this case a phase change material would be doped with a molecule or nanoparticle to generate heat.

A third form of photoreversible mechanical adhesion would be to generate photoreversible velcro, or hook and loop fasteners. In this scenario a series of static loops, most likely from a polymer, would be attached to one side of the device. The second side would have a p-type photomechanical form of hooks that bend when exposed to light. When adhesion is needed the two sides are pressed together and light is used to make the photomechanical hooks go from straight to curled. These small hooks will catch the loops and create the adhesive force. When the adhesion is no longer needed a second wavelength of light is used to bend the photomechanical hooks back to the straight direction allow the two surfaces to be separated. Figure 6.3 shows the deadhesion process for the hook and loop design.

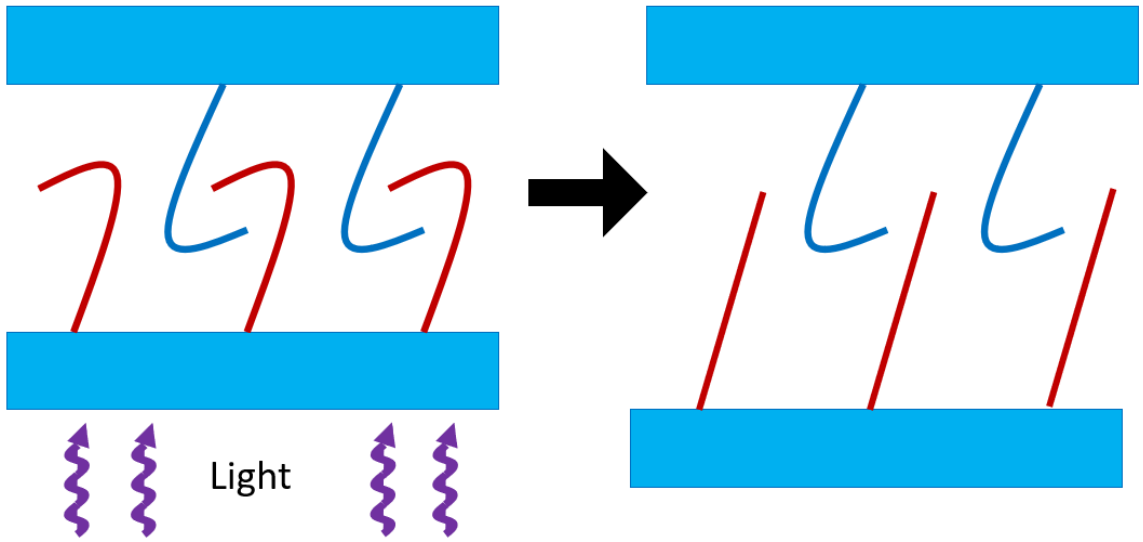

Figure 6.3: Photoreversible Velcro could be made using p type photomechanical materials. The red hooks are the photomechanical portion of the design.

6.2 The Future of Fluorinated 9AC Compounds

Further fluorination of 9AC will prove difficult due to the complexities of further selectively fluorinating 9AC. Additional characterization is needed for 4,5diF-9AC as our

detection method was not able to deliver reliable data on the recovery time of that molecule. The recovery of 9AC compounds also showed extreme temperature dependence in the initial data that was taken. The data was taken over a very small range though. A larger temperature range and more sensitive equipment will be beneficial in better understanding this crystalline system. Using a cryostat to obtain low temperature data could also pinpoint the activation energy required to back react. Finally, a martensitic phase transition was also observed in some 9AC molecules. This phase transition should be studied further. Studying this phenomenon will give more insight into kinetics inside the crystal. Currently many kinetic models exist but none can accurately describe the kinetic situation that is observed.

6.3 Enhancing Crystalline Nitrene Stability and Applying the System to Quantum Computing

The generation of room temperature stable nitrenes will not only allow for these usually unstable molecules to be studied but also allows their use in real world applications. The first step is to measure the coherence times of these molecules and determine whether Rabi oscillations can be observed. Ideally coherence times will be in the hundreds of microseconds time scale to be useful for quantum computing. The nitrene crystal structure has very large concentrations of unpaired electrons by each other. This will likely preclude its use in most quantum information systems, though it could be used as a quantum shift register. Spacing out the radical nitrenes will allow single radical centers to be individually addressed and likely increase coherence times. We plan on using a cocrystal to stabilize the nitrenes. In an ideal scenario we will be able to remove atoms with a spin to reduce the

hyperfine interaction as well. Fluorescence lifetimes will need to be measured to ensure that the qubit information can be read out. The ability to have a stable, room temperature nitrene that can fluoresce will allow for these cocrystals to be used in quantum information systems.

6.4 Conclusion

We have looked at three photoreactive stimulus response systems and optimized a variety of factors to create a system with more desirable qualities. The ultimate goal is to have a high degree of control over our photomechanical systems. Ideally, we will have a toolbox of optimization techniques which can alter the system's properties to given specifications. Control over the molecule, the matrix it is in, and the crystal structure all play an important role in achieving this. The quest for high levels of fidelity over photomechanical systems is just beginning. These light driven stimulus response systems can bring weight savings, increased efficiency, and unique properties that a conventional chemical system cannot.

6.5 References

1 Tong, F.; Xu, W.; Guo, T.; Lui, B. F.; Hayward, R. C.; Palffy-Muhoray, P.; Al-Kaysi, R. O.; Bardeen, C. J., Photomechanical molecular crystals and nanowire assemblies based on the [2+2] photodimerization of a phenylbutadiene derivative. *J. Mater. Chem. C* 2020, *8*, 5036-5044.